

DOKUZ EYLÜL UNIVERSITY
GRADUATE SCHOOL OF NATURAL AND APPLIED SCIENCE

**ELECTROMAGNETIC ACTUATOR BASED
CONTACTLESS CONTROL OF MICRO ROBOT
OPERATION FOR BIOMEDICAL
TECHNOLOGIES**

by
Nail AKÇURA

June, 2022
İZMİR

**ELECTROMAGNETIC ACTUATOR BASED
CONTACTLESS CONTROL OF MICRO ROBOT
OPERATION FOR BIOMEDICAL
TECHNOLOGIES**

**A Thesis Submitted to the
Graduate School of Natural and Applied Sciences of Dokuz Eylül University
In Partial Fulfillment of the Requirements for the Degree of Doctor of
Philosophy in Mechatronics Engineering, Mechatronics Engineering Program**

**by
Nail AKÇURA**

**June, 2022
İZMİR**

Ph.D. THESIS EXAMINATION RESULT FORM

We have read the thesis entitled “**ELECTROMAGNETIC ACTUATOR BASED CONTACTLESS CONTROL OF MICRO ROBOT OPERATION FOR BIOMEDICAL TECHNOLOGIES**” completed by **NAİL AKÇURA** under supervision of **ASST. PROF. DR. ÖZGÜR TAMER** and we certify that in our opinion it is fully adequate, in scope and in quality, as a thesis for the degree of Doctor of Philosophy.

Asst. Prof. Dr. Özgür TAMER

Supervisor

Asst. Prof. Dr. Hakkı Tarkan YALAZAN

Thesis Committee Member

Assoc. Prof. Dr. Levent ÇETİN

Thesis Committee Member

Assoc. Prof. Dr. Barış BIDIKLİ

Examining Committee Member

Assoc. Prof. Dr. Erkin GEZGİN

Examining Committee Member

Prof. Dr. Okan FISTIKOĞLU

Director

Graduate School of Natural and Applied Sciences

ACKNOWLEDGEMENT

First and foremost, I would like to express my deepest appreciation to my supervisor Asst. Prof. Dr. Özgür Tamer for his unconditional support, invaluable guidance, and vigorous encouragement.

My sincere gratitude also goes for Assoc. Prof. Dr. Levent Çetin for his endless support and guidance. I would like to express my deepest gratitude to Asst. Prof. Dr. Hakkı Tarkan Yalazan for his precious contribution and fruitful discussions.

I would like to acknowledge the financial support provided by the Scientific and Technological Research Council of Turkey (TÜBİTAK, project No. 215M879) during my Ph.D. Also, I am also thankful for the supports provided by İzmir Katip Çelebi University Coordinatorship of Scientific Research Projects (project No. 2018-ÖDL-MÜMF-0020). I would like to acknowledge Ege University Mechanical Engineering Department Smart Structures Laboratory for the technical support about providing finite element analysis program.

Finally, this thesis would not have been completed without support and encouragement of my family members. I must express my best gratitude to my mother Hanife Akçura, for her perpetual support, understanding and patience. I also must express my profound gratitude to my brother Murat Akçura, his wife Selin Akçura and my lovely nephew Çınar Akçura for their endless support.

Nail AKÇURA

ELECTROMAGNETIC ACTUATOR BASED CONTACTLESS CONTROL OF MICRO ROBOT OPERATION FOR BIOMEDICAL TECHNOLOGIES

ABSTRACT

Microrobots offer enormous potential for biomedical applications in many aspects. Deploying the microrobots into the human body and applying related treatment is one of the sole purposes for researchers. Micro-scaled microrobots driven by an external magnetic field is now one of the state-of-the-art technologies. The microrobot may require a few degrees of freedom to accomplish its goal. Those motions can be provided using multiple electromagnetic actuators. Also, the desired microrobot locomotion can only be accomplished by proper actuator control. In this thesis, a microrobot manipulation system concept was studied. This concept uses a pair of magnetic actuators and derives the complexity of the magnetic actuation to manipulators. The electromagnetic actuators are attached onto an Euclidean platform parallel manipulator. Since this concept is not proper to manufacture directly, a prototype model was induced, adapting some of the motions in different way. A subsidiary manipulator supports the motion gaps of the system. Mobile electromagnetic actuators were analysed, developed, and manufactured considering the facts such as weight. The system was applied to some developed phantoms of aneurysms, i.e., deformations with the vein walls, in some terms making a shape like a balloon. These models especially considered cerebral aneurysms that it may be difficult to reach. The fundamental microrobot motions on xy and xz planes were studied and navigational tasks were carried out inside phantom models.

Keywords: Microrobot, EMA, aneurysm, magnetic gradient, Euclidean platform

ELEKTROMANYETİK EYLEYİCİLER İLE MİKRO ROBOTLARIN BİYOMEDİKAL TEKNOLOJİLER İÇİN TEMASSIZ KONTROLÜ

ÖZ

Mikrorobotlar, biyomedikal uygulamalar için birçok açıdan muazzam potansiyel sunarlar. Mikrorobotların insan vücuduna sokmak ve ilgili tedaviyi uygulamak, araştırmacıların yegane amaçlarından birisidir. Harici manyetik alan ile yönlendirilen mikro ölçekli mikro robotlar teknolojinin en gelişmiş noktası seviyesindedir. Mikrorobot, verilen görevi gerçekleştirmek için birkaç derece serbestlik derecesinde harekete ihtiyaç duyabilirler. Bu hareketler ise birden fazla elektromanyetik eyleyici kullanılarak sağlanabilir. Ayrıca istenilen mikrorobot hareketi ancak eyleyicilerin uygun kontrolü ile gerçekleştirilebilir. Bu tezde, bir mikro robot manipülasyon sistemi konsepti incelenmiştir. Bu konsept bir çift elektromanyetik eyleyici içerir ve manyetik tahrikteki kompleksliği robot manipülatörlere dağıtır. Elektromanyetik eyleyiciler bir Öklid platformu paralel manipülatör üzerinde yer alır. Bu konsept doğrudan üretime uygun olmadığı için bazı uyarlamalar yapılarak bir prototip model oluşturulmuştur. Yardımcı bir manipulator sistemi, paralel robot sisteminin yapamadığı hareketler konusunda destekler. Mobil elektromanyetik eyleyiciler, ağırlık gibi durumlar göz önünde bulundurularak analiz, geliştirme ve üretimi gerçekleştirilmiştir. Sistem, anevrizmaların, yani damar duvarlarında gelişen deformasyonlar bazı durumlarda ise balon şeklinde, bazı fantomları geliştirilmiş ve uygulanmıştır. Bu modellerde özellikle ulaşılması zor olabilecek serebral anevrizmalar dikkate alınmıştır. xy ve xz düzlemlerindeki temel mikrorobot hareketleri incelenmiş ve fantom modeller içinde navigasyon görevleri gerçekleştirilmiştir.

Anahtar kelimeler: Mikrorobot, EMA, anevrizma, manyetik gradyan, Öklid platformu

CONTENTS

	Page
Ph.D THESIS EXAMINATION RESULT FORM	ii
ACKNOWLEDGEMENT	iii
ABSTRACT.....	iv
ÖZ.....	v
LIST OF FIGURES	x
LIST OF TABLES	xvii
LIST OF SYMBOLS	xviii
ABBREVIATIONS	xix
CHAPTER 1 - INTRODUCTION.....	1
1.1 Introduction.....	1
1.2 Motivation.....	2
1.3 Literature Survey	3
1.4 Research Gaps.....	12
1.5 Objectives and Contributions of the Thesis.....	15
CHAPTER 2 - MICROROBOT AND MICROROBOT LOCOMOTION.....	16
2.1 Introduction.....	16
2.2 Microrobots.....	16
2.2.1 Wireless Microrobot Actuation	17
2.2.2 Electromagnetic Actuation and Locomotion Methods.....	18
2.2.3 The Magnetic Gradient Actuation	20
2.3 Microrobot Analysis and Manufacturing.....	21
2.3.1 Verification of Permanent Magnet Values	22
2.3.2 Microrobot environment.....	26

2.3.3	Defining the Needs	26
2.3.4	Manufacturing of Microrobot.....	29

CHAPTER 3 - ELECTROMAGNETIC ACTUATORS..... 30

3.1	Introduction.....	30
3.2	Magnetic Actuators in Microrobot Manipulation	30
3.3	Actuator Configuration of EMAs	31
3.4	Prior Analyses of a Different EMA	32
3.5	EMA Design	34
3.5.1	Finite Elements Method and Mesh Decision	35
3.5.1.1	Homogeneous Magnetic Field Analysis (Variable Electromagnet Distances).....	38
3.5.1.2	Magnetic Gradient Analysis (Variable Electromagnet Distances)	38
3.5.2	EMA Design Analysis.....	39
3.6	EMA Manufacturing.....	45
3.6.1	EMA Calibration	46
3.6.1.1	Results and Discussion on EMA Calibration.....	56

CHAPTER 4 - THE MANIPULATOR SYSTEMS 57

4.1	Introduction.....	57
4.2	Robot manipulators.....	57
4.3	Previous Studies and Works	57
4.4	Analysis, Design, and Manufacturing of Manipulator Systems	62
4.4.1	Euclidean Platform Parallel Manipulation System.....	63
4.4.2	Subsidiary Manipulation System.....	70
4.4.3	EMA Linear Mechanism	73
4.5	Mechanical System Calibrations	74
4.5.1	Conclusion of Mechanical System Calibrations	81

CHAPTER 5 - SOFTWARE ARCHITECTURE AND IMPLEMENTATION 83

5.1	Introduction.....	83
5.2	Choosing the Operating System and Its Distribution	83
5.3	Robot Operating System.....	84
5.3.1	Nomenclature	85
5.3.2	Library Overview	86
5.4	OpenCV	87
5.5	QT	88
5.6	Hardware.....	88
5.6.1	Computer	88
5.6.2	Dynamixel Smart Servo Motors.....	89
5.6.3	Stepper Motor, Stepper Motor Drivers, and Arduino Mega board ..	90
5.6.4	Basler Ace Camera.....	92
5.7	ROS Environment Development	92
5.8	Calibrations.....	94
5.8.1	Camera calibration	94
5.9	Object Tracking Algorithm.....	99
5.10	Inverse Kinematic Using tf2 Package.....	100
5.11	Operating Principles of Nodes and Control Algorithms.....	102
5.12	User Interface.....	107

CHAPTER 6 - MOTION APPLICATIONS 111

6.1	Introduction.....	111
6.2	Biomedical Application: Aneurisms.....	111
6.3	Force Tests	114
6.4	Programmed Control Motions	117
6.4.1	Programmed Motions on xy Plane	117
6.4.2	Programmed Motions on xz Plane	125
6.5	Results and Discussion	129

CHAPTER 7 - CONCLUSION AND FUTURE WORKS 131

7.1 Overview..... 131

7.2 Future Works 132

REFERENCES..... 133



LIST OF FIGURES

	Page
Figure 1.1 Helmholtz coil setup	4
Figure 1.2 Rotational propulsion with Helmholtz coil setup	5
Figure 1.3 Jelly-like robot motion using Helmholtz coil setup.....	5
Figure 1.4 ON-OFF control-based robot motion using Helmholtz coil setup	5
Figure 1.5 Saddle coils (a) system configuration, (b) microrobot setup	6
Figure 1.6 OctoMag setup.....	6
Figure 1.7 MiniMag setup (a) side view of working space (b) integration with a flourescent microscope.....	7
Figure 1.8 Coil setup differences between OctoMag and MiniMag	7
Figure 1.9 6 DOF actuation system with 8 coils (a) computer aided design of the setup (b) side view of the setup	7
Figure 1.10 Microrobot actuation system using Helmholtz and Maxwell coils	8
Figure 1.11 Cylindrical permanent magnet rotation-based setup (a) actuation system installed as end effector to a robot manipulator (b) rotating permanent magnet (c) spherical shaped test robot (d) helical shaped test robot.....	9
Figure 1.12 Spherical permanent magnet rotation-based setup	9
Figure 1.13 Magnetically controlled capsule endoscopy system.....	10
Figure 1.14 Swarm robotic test in a mouse (a) test bench setup (b) visual feedback	11
Figure 1.15 Microrobot test in rabbit eye placed into OctoMag setup	11
Figure 1.16 In vivo wireless capsule trials on female pig.....	12
Figure 1.17 A concept work of the desired micromanipulation system	14
Figure 2.1 Bio-inspired microrobots	18
Figure 2.2 Types of microrobots and their actuation methods.....	19
Figure 2.3 The motion of the microrobot (a) homogenous magnetic field causing τ torque (b) the magnetic field gradient causing F force.	21

Figure 2.4 General layout using two EMAs with microrobot.....	21
Figure 2.5 N35 grade cylindrical permanent magnet with 1 mm to 1 mm dimensions	22
Figure 2.6 Hysteresis curve and remanence value	23
Figure 2.7 A cylindrical permanent magnet flux density.....	24
Figure 2.8 The tip of STD18-0404 F.W.Bell Gaussmeter measurement probe and its embedded sensor	24
Figure 2.9 The positioning of the permanent magnet on the probe	25
Figure 2.10 The acting forces onto the microrobot.....	27
Figure 3.1 Homogenous magnetic field and magnetic field gradient configurations	31
Figure 3.2 Homogenous magnetic field occurring in ROI (Region of Interest) on xy plane and classification of areas.....	33
Figure 3.3 Analysis parameters.....	33
Figure 3.4 Dimensions of the cylindrical coils and its core in terms of w (width), h (height), L (length), L_e (extrusion length), h_e (extrusion height), L_c (coil length) and r_c (coil radius) (Alasli et al., 2019).....	34
Figure 3.5 The reference meshing model for performance comparison	37
Figure 3.6 Mesh performance comparison of reference (mesh sample 1) and more dense meshed samples.....	37
Figure 3.7 Effect of layers in magnetic field strength and weight.....	40
Figure 3.8 Effect of layers in magnetic field strength and weight shown as ratio.....	41
Figure 3.9 Effect of each layer in magnetic field strength.....	41
Figure 3.10 Effect of winding length in magnetic field strength and weight	42
Figure 3.11 Effect of winding length in magnetic field strength and weight shown as ratio.....	42
Figure 3.12 Effect of each winding length in magnetic field strength.....	43
Figure 3.13 Effect of winding length for 15 layers in magnetic field strength and weight.....	44

Figure 3.14 Effect of winding length for 15 layers in magnetic field strength and weight shown as ratio	44
Figure 3.15 Effect of each winding length for 15 layers in magnetic field strength..	44
Figure 3.16 Manufactured EMAs	45
Figure 3.17 Calibration setup with gaussmeter probe.....	47
Figure 3.18 Position referencing the gaussmeter probe using the structure	47
Figure 3.19 KUKA robot setup for calibration	48
Figure 3.20 Magnetic field measurement setup	49
Figure 3.21 Symmetric configuration simulation result	50
Figure 3.22 Symmetric configuration measurement results	51
Figure 3.23 Simulation results of asymmetry configuration $\epsilon=10\text{ mm}$	52
Figure 3.24 Comparison of measurement and simulation results of asymmetry configuration $\epsilon=10\text{mm}$	52
Figure 3.25 Magnetic field gradient comparison of asymmetry configuration $\epsilon=10\text{ mm}$	53
Figure 3.26 Simulation results of asymmetry configuration $\epsilon=20\text{ mm}$	53
Figure 3.27 Comparison of measurement and simulation results of asymmetry configuration $\epsilon=20\text{mm}$	54
Figure 3.28 Magnetic field gradient comparison of asymmetry configuration $\epsilon=20\text{mm}$	54
Figure 3.29 Simulation results of asymmetry configuration $\epsilon=30\text{ mm}$	55
Figure 3.30 Comparison of measurement and simulation results of asymmetry configuration $\epsilon=30\text{ mm}$	55
Figure 3.31 Magnetic field gradient comparison of asymmetry configuration $\epsilon=30\text{mm}$	56
Figure 4.1 A general Stewart platform.....	58
Figure 4.2 Microlar Rotopod R-3000.....	59

Figure 4.3 Stewart-like studied manipulator system.....	60
Figure 4.4 First subsidiary system design.....	61
Figure 4.5 First Euclidean platform parallel manipulator accompanied with subsidiary manipulator system	62
Figure 4.6 The prototype system showed with the motion adaptations.....	63
Figure 4.7 Parallel manipulator system.....	64
Figure 4.8 Inverse kinematic of one leg on an Euclidean plane	64
Figure 4.9 Platform rotation and platform centre point relationship	67
Figure 4.10 The final design of Euclidean platform parallel manipulator with hidden beams.....	68
Figure 4.11 Design improvement with major structure reinforcement revisions with leg and spherical joint structure	69
Figure 4.12 Simplified 1/3 model of the parallel manipulator for dynamic calculations	69
Figure 4.13 xy cartesian structures: a) H-bot b) CoreXY c) T-bot	71
Figure 4.14 Subsidiary manipulator layout.....	71
Figure 4.15 Manufactured subsidiary manipulator system.....	72
Figure 4.16 Electromagnet linear mechanism.....	73
Figure 4.17 The last form of the platform and electromagnet mechanism layout	74
Figure 4.18 Measurement sensor assembly for subsidiary mechanism	76
Figure 4.19 Electromagnet mechanism calibration.....	77
Figure 4.20 Parallel robot calibration system where three cameras observe the measurement probes	79
Figure 4.21 Marker and camera configurations shown in the user interface of the program	79
Figure 5.1 A general ROS communication schematic.....	86
Figure 5.2 Dynamixel network schematic	90

Figure 5.3 Stepper motor connection schematic	91
Figure 5.4 A general glance to pema_gui and the other nodes	93
Figure 5.5 GUI plugins	94
Figure 5.6 Microrobot environment and bottom camera configuration.....	95
Figure 5.7 Bottom camera calibration using graph paper	96
Figure 5.8 Bottom camera calibration with real application.....	97
Figure 5.9 Front camera calibration bench	98
Figure 5.10 tf2 conversion of the inverse kinematic.....	101
Figure 5.11 Calculating d on Euclidean plane	101
Figure 5.12 General motion layout showing the topics	102
Figure 5.13 Subsidiary manipulator system and coordinate frames	103
Figure 5.14 Parallel manipulator system and coordinate frames	104
Figure 5.15 A brief and general motion algorithm flowchart for all motions.....	105
Figure 5.16 Snapping function during motion on xy plane	106
Figure 5.17 Snapping function during motion on xz plane.....	107
Figure 5.18 General GUI layout with plugins.....	107
Figure 5.19 GUI camera control page overview	108
Figure 5.20 Parallel manipulator calibration, referencing and monitoring page overview	108
Figure 5.21 Parallel manipulator motion control page overview.....	109
Figure 5.22 Subsidiary manipulator page overview	109
Figure 5.23 EMA mechanism page overview	110
Figure 5.24 Rosbag and camera image plugin page overviews	110
Figure 6.1 Common aneurism types	111
Figure 6.2 Cerebral vein system	112
Figure 6.3 An aneurism occurrence	113

Figure 6.4 A phantom aneurysm model with a microrobot inside.....	114
Figure 6.5 Gravity compensation configuration	115
Figure 6.6 An example force test motion from centre towards to an EMA.....	116
Figure 6.7 When constant ratio 7.176 applied, the gradient velocity relationship...	117
Figure 6.8 x axis pure motion capability test (a) EMAs snap and follow the microrobot (b) between 1-2 there is 90° subsidiary actuator rotation and EMAs only follow in homogenous configuration as between 2-3 EMAs apply gradient configuration and cause local motion.....	119
Figure 6.9 x axis motion position plot with global (spatial) positions, first making the circular shape.....	119
Figure 6.10 x axis motion position plot with local (raw camera reading) positions, last making the straight line	120
Figure 6.11 y axis pure motion capability test (a) EMAs snap and follow the microrobot (b) between 1-2 there is 90° subsidiary actuator rotation and EMAs only follow in homogenous configuration as between 2-3 EMAs apply gradient configuration and cause local motion.....	121
Figure 6.12 y axis motion position plot with global (spatial) positions, first making the circular shape.....	121
Figure 6.13 y axis motion position plot with local (raw camera reading) positions, last making the straight line	122
Figure 6.14 The developed constrained xy motion model.....	123
Figure 6.15 Guided motion control that the goal position is given by mouse click, the clicked positions during the motion marked in order.....	124
Figure 6.16 The motion result plot (mirrored for better observation).....	124
Figure 6.17 The resin models and their silicon moulds for xz motion	125
Figure 6.18 Most used model for xz motion	126
Figure 6.19 Applicable models for xz motion	126
Figure 6.20 The gravity compensation and motion along x axis	127

Figure 6.21 Aneurysm application on xz axis (a) between 1-2 floating then between 2-3 gradient motion (b) between 3-4 gradient motion then between 4-5 submerging then between 5-6 gradient motion then between 6-7 floating (c) sequential positions during the motion 128

Figure 6.22 15° rotation motion with gravity compensation 129



LIST OF TABLES

	Page
Table 2.1 Remanence measurements of the permanent magnets.....	25
Table 3.1 Analysing the layer number effect	40
Table 3.2 Analysing the winding length effect	41
Table 3.3 Analysing the winding length effect	43
Table 3.4 Design and manufactured model parameter comparison.....	45
Table 3.5 Weight summary for EMAs and the moving platform	46
Table 4.1 Subsidiary manipulator system calibration of 10 mm steps	76
Table 4.2 Electromagnet linear mechanism calibration results	77
Table 4.3 Translation motion of the platform	80
Table 4.4 Pitch motion of the platform	80
Table 4.5 Roll motion of the platform	81
Table 5.1 Bottom camera calibration readings	96
Table 5.2 Resolution and conversion of bottom camera image.....	96
Table 5.3 Front camera calibration readings.....	98
Table 5.4 Resolution and conversion of front camera image.....	98
Table 6.1 Experimental constant velocity results with different asymmetry parameters	116

LIST OF SYMBOLS

H	: External magnetic field strength (G)
M	: Magnetization (emu/g)
B	: Magnetic flux density (mT)
B_r	: Remanent flux density (T)
μ	: Permeability of the material (N/A ²)
μ₀	: Permeability of vacuum (4π10 ⁻⁷ H/m)
F	: Force (N)
τ	: Torque (Nm)
ε	: Asymmetric configuration parameter (mm)
NdFeb	: Neodymium
F_{mag}	: Magnetic force (N)
F_{grav}	: Gravitational force (N)
F_{bouy}	: Buoyancy force (N)
F_{drag}	: Drag force (N)
G_u(ε)	: Correlation of force with asymmetry parameter
C_u	: Drag constant
C_m	: Magnetic constant

ABBREVIATIONS

EMA	: Electromagnetic actuator
HMI	: Human Machine Interface
GI	: Gastrointestinal
ROS	: Robot Operating System
MEMS	: Microelectromechanical systems
ROI	: Region of Interest
FEM	: Finite Elements Method
RMS	: Root Mean Square
RMSE	: Root Mean Square error

CHAPTER 1

INTRODUCTION

1.1 Introduction

The focus of this study is to develop a system for the untethered microrobot manipulation which should serve for biomedical applications. The microrobots steps into people's lives with the rapid development of technologies. The milestone of these systems can be counted as the advancements of microscale manufacturing in 2000s, which earlier on it was all theoretical works. These scaled robotic applications received a significant boost thanks to the leadership of various research groups, especially with the development of 3D printing technologies. These microscale robot agents can be utilized for many purposes, especially for biomedical applications. In vitro and in vivo can be both included in these applications. In biomedical technologies, size of the equipment can mean a lot. Using these dimensional advantages, the equipment can enable the treatment of various diseases via robot controllability and reachability to specific target areas in the human body. Defining scale dimensions (particularly for micro-scaled robots) with specific boundaries is problematic, the highest limit is set at a few millimeters.

Microrobot manipulator systems can be inspected in a few scopes, including microrobot, locomotion technique, internal/external actuators, microrobot position feedback, microelectronics, power transmission, and so on. However, it brings challenges with nearly each scope even with the basics. Microrobot locomotion using external magnetic field is assumed to be one of the methods with greatest potential that can be commonly utilized in the future.

Counting the potential application in vitro, micro/nano-scaled robots can be used in biomedical applications for targeted therapy (drug delivery, object manipulation, heat exchange with tissues, and so on), material removal (biopsy, ablation, and so on), controllable structures (scaffolds, stents, implants, and so on), and telemetry (oxygen concentration, image capture, and so on) (Nelson et al., 2010). The circulatory system,

central nervous system, urinary system and prostate, eye, ear, fetal, and gastrointestinal system are also relevant human body pathways (Nelson et al., 2010). This type of technology is expected to play a vital role in a variety of industries in the future (Carpi, 2010).

1.2 Motivation

The first motivation of this thesis is to resolve the dynamics of the microrobot. For this reason, it has been come up with the general motion equation. Using different environments, microrobots, EMAs requires the parameters to be revealed. In this way, the relationship between the microrobot and EMAs can be constructed, and these data can be used for microrobot, EMA and manipulator design.

The second motivation of the thesis is to come up with analysis and design of EMA. EMAs can be crucial with generated magnetic field form, magnitude and even EMA weight. It should be considered with the demands of the design of control principles and the mechanical requirements.

The third motivation of this thesis is to investigate the mechanical manipulators with their structure and analysis. The demands of the system majorly consist of dimensional requirements with many parameters. To provide these motions, the mathematical relation should be inspected, especially for inverse and forward kinematic calculations.

The fourth motivation of the thesis is to design a mechatronic system which includes a computer and peripheral components like motor drivers and cameras for motion control, data acquisition and Human-Machine Interface (HMI). The system should be compatible with every component and provide the necessary needs for the system.

1.3 Literature Survey

First, it should be informed that some of the scopes were intentionally left to their related sections.

Biomedical in vivo applications are believed to provide advantages in many treatments and applications. One of the focused applications of the micro/nanorobots is minimally invasive drug delivery. This kind of treatment helps recovery time, infection risks, medical complications, and post operation pain. Researchers are working on special methods for unloading the drug at the target point. Due to the small dimensions, conventional methods are not applicable on the robot and making this a challenging area. Some of the solutions for this problem are coating the robot with drug (Ergeneman et al., 2008), unloading the coated drug using ultrasound (Mhanna et al., 2014), covering with self-folding temperature controlled hydrogel (Fusco et al., 2014), shape shifting structures with the temperature (Fusco et al., 2015), unloading the mounted pDNA with change in frequency (Fusco et al., 2015) and different robot structures (Floyd et al., 2008; Huang et al., 2016; Yim & Sitti, 2012). Moreover, some sicknesses like ulcer and tumour can be detected and cured in early stages, and prevent vital sicknesses to spread to other organs (Chevalerias et al., 2008). Picking samples from the target area is also a challenging area again due to the dimensions and unconventional methods. Researchers work on microgrippers (tweezer like structures) with different actuation methods (D. H. Kim et al., 2004; K. Kim et al., 2004; Nogimori et al., 1997). If flexing the scale limits a little, microrobots can be used in endoscopy applications. Endoscopy is the best way to view inner tract of gastrointestinal (GI) and detect the diseases directly and efficiently (Eliakim et al., 2004).

Leaving the endoscopy type robots, microrobots are mostly controlled in the liquids which provides better accuracy. Also, mostly the environments generally have low Reynolds number. When the scale of the microrobots and the applications gets smaller, the generated locomotion force and also other general motion forces alters, which may even lead to consider the forces of molecular physics (Diller, 2011). Following these, different microrobot locomotion were discovered.

The fundamental principle of microrobot manipulation using magnetic field starts with magnetic field gradient force and homogenous magnetic field torque acts. With the control of those magnetic aspects, a microrobot with magnetic properties can be locomoted with its motion principle.

One of the prior microrobot actuation systems in 3D was studied (Yesin et al., 2006), showing that using magnetic gradient for the navigation is applicable. This work led to design of OctoMag actuator system (Kummer et al., 2010), consisting of eight electromagnetic actuator, leading to 5 DOF microrobot control.

At the same time with the development of OctoMag, there were also other actuator systems that might be counted alike (Kratochvil et al., 2014)., well inspected (Xu et al., 2015).

Basically, 3D Helmholtz coils 3-axis rotating motion can be accomplished. A uniform rotating magnetic field can be generated with this setup at the workspace taking part at the centre where the coil axes intersect (Zhang, Abbott, Dong, Kratochvil, et al., 2009), as shown in Figure 1.1. The researchers (Mahoney et al., 2011; Sendoh et al., 2004; Xu et al., 2014) showed that rotating magnetic field can propel helical type microrobots, as in Figure 1.2.

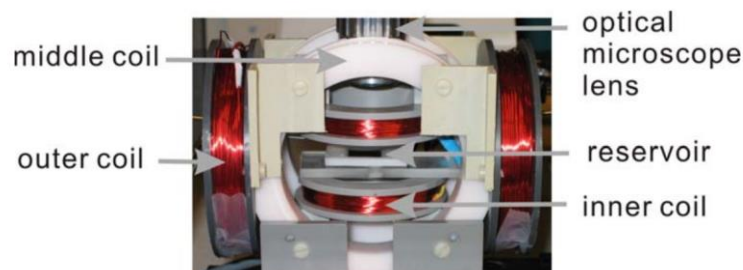


Figure 1.1 Helmholtz coil setup (Zhang, Abbott, Dong, Kratochvil, et al., 2009)

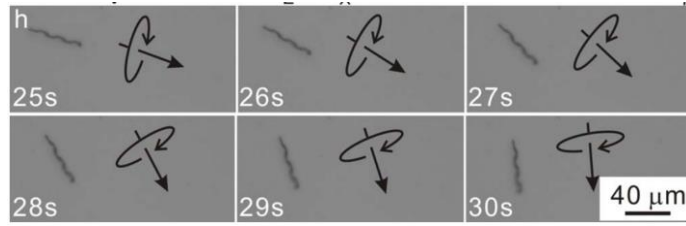


Figure 1.2 Rotational propulsion with Helmholtz coil setup (Mahoney et al., 2011)

In (Ko et al., 2012), a square form magnetic field is used to manipulate a jelly-like robot with Helmholtz coil setup, shown in Figure 1.3. In (Frutiger et al., 2009; Gao et al., 2010), a flexible nanowire tail is used for propulsion by ON-OFF magnetic field, shown in Figure 1.4.

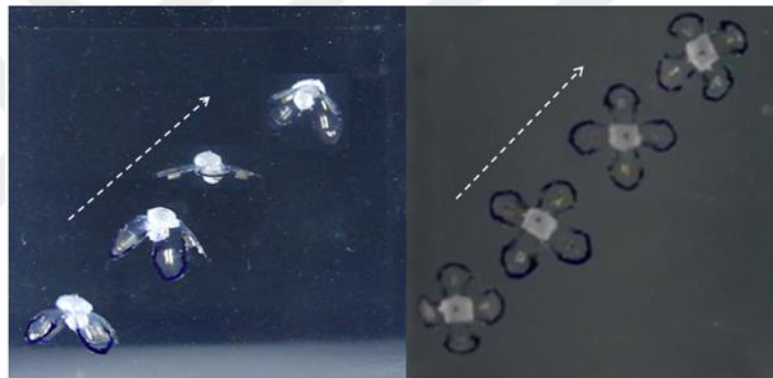


Figure 1.3 Jelly-like robot motion using Helmholtz coil setup (Ko et al., 2012)

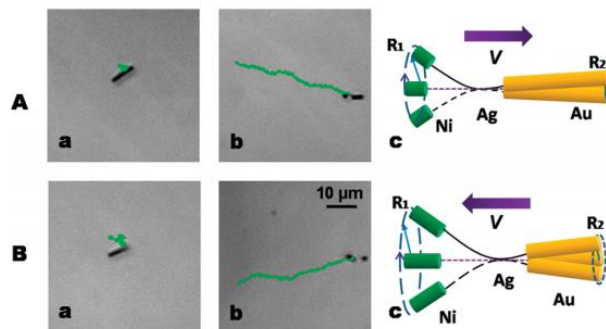


Figure 1.4 ON-OFF control-based robot motion using Helmholtz coil setup (Gao et al., 2010)

Using the gradient of magnetic field, the robots can be also propelled. In (Jeon et al., 2010), using uniform saddle coils generating uniform magnetic field, one-axis rotation can be accomplished, shown in Figure 1.5.

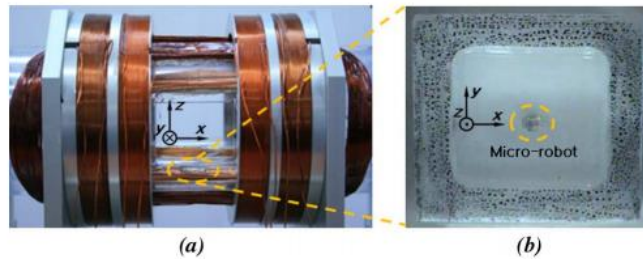


Figure 1.5 Saddle coils (a) system configuration, (b) microrobot setup (Jeon et al., 2010)

Nelson and his friends increase the degrees of freedom (DOF) (2 rotation and 3 translation) of the robot control in 3D space with a new setup, called OctoMag (Kummer et al., 2010), shown in Figure 1.6. Then, they come up with a new setup, called MiniMag (Figure 1.7) with the same DOF, where the ergonomics of the system is better (Schuerle et al., 2013). The differences are given between these two systems in Figure 1.8.



Figure 1.6 OctoMag setup (Kummer et al., 2010)

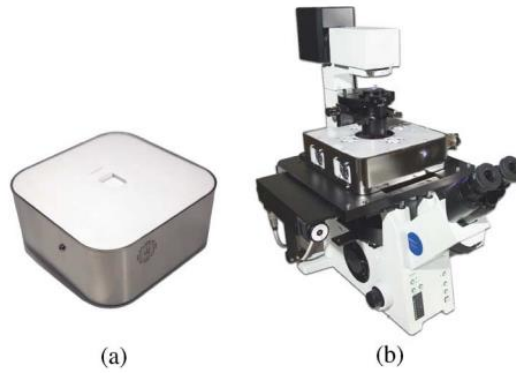


Figure 1.7 MiniMag setup (a) side view of working space (b) integration with a fluorescent microscope (Schuerle et al., 2013)

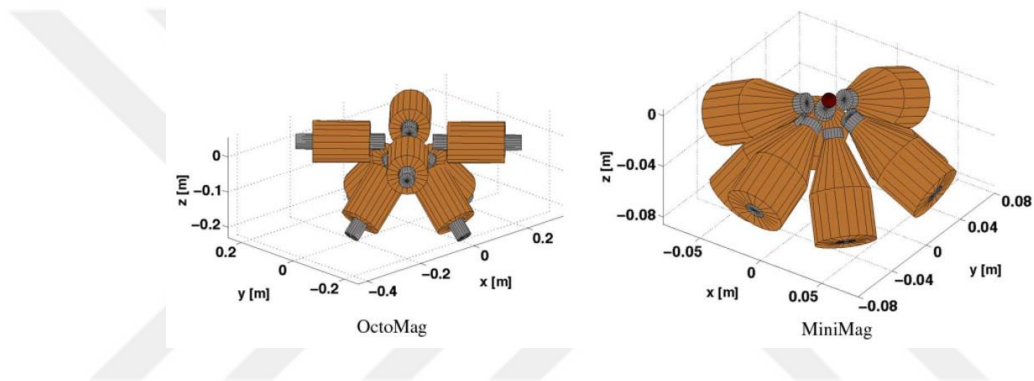


Figure 1.8 Coil setup differences between OctoMag and MiniMag (Schuerle et al., 2013)

Metin Sitti and his friends come up with a new system where 6 DOF (3 rotation and 3 translation), showing that every motion is possible inside the 3D working space (Diller et al., 2013; Pawashe et al., 2009), given in Figure 1.9.

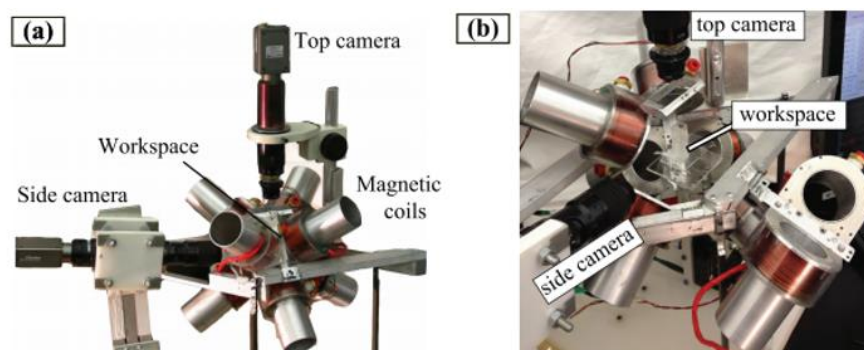
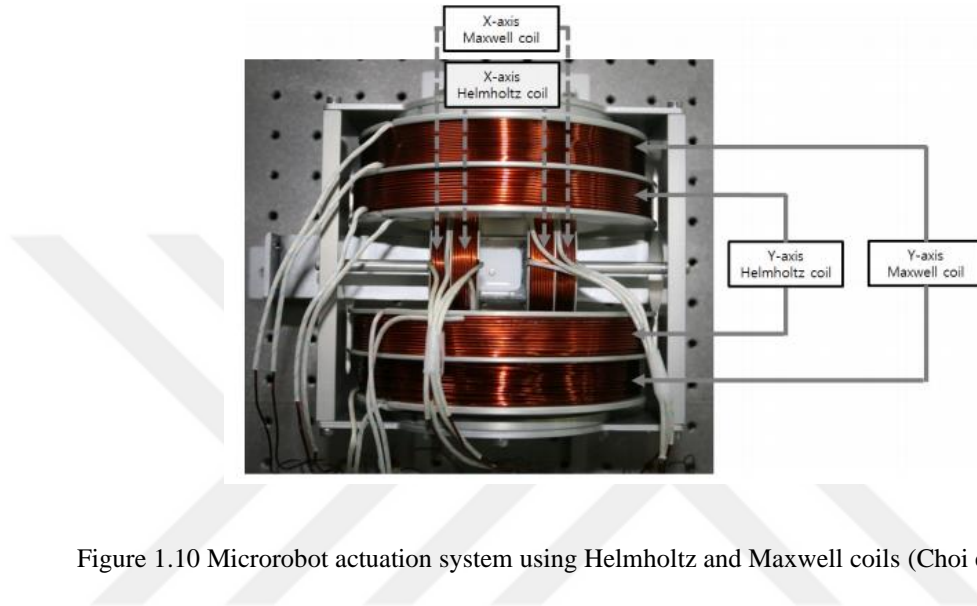


Figure 1.9 6 DOF actuation system with 8 coils (a) computer aided design of the setup (b) side view of the setup (Diller et al., 2013)

Also, there are some systems where uniform magnetic field is generated by Helmholtz coils and magnetic field gradient is generated by Maxwell coils separately at the same system where most of them work in 2D space (Choi et al., 2009; Go et al., 2015; Hu et al., 2011; Jeon et al., 2010; Kim et al., 2014; Yesin et al., 2006), shown in Figure 1.10.



Different from electromagnet actuated systems, in Utah Telerobotics Laboratory, it is shown that the microrobot motion can be accomplished using a rotating permanent magnet, generating a rotating magnetic field (Mahoney & Abbott, 2012, 2014, 2016; Popek et al., 2017), given in Figure 1.11 and Figure 1.12. Also, using one permanent magnet magnetic flux lines, a capsule robot is controlled in (Mahoney & Abbott, 2016).

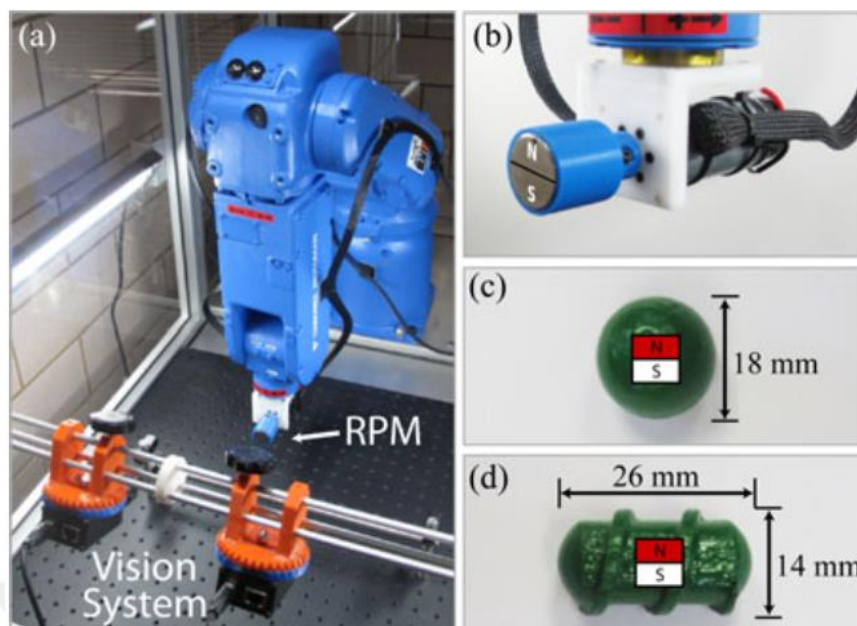


Figure 1.11 Cylindrical permanent magnet rotation-based setup (a) actuation system installed as end effector to a robot manipulator (b) rotating permanent magnet (c) spherical shaped test robot (d) helical shaped test robot (Mahoney & Abbott, 2014)

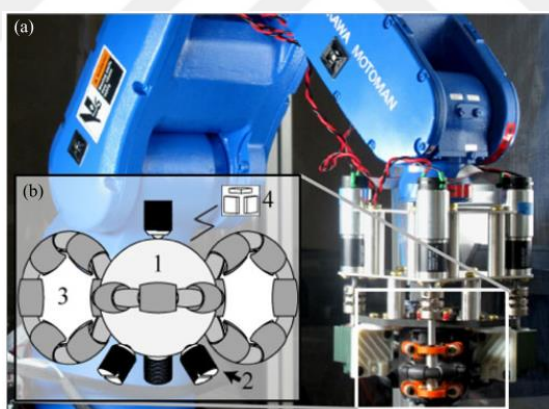


Figure 1.12 Spherical permanent magnet rotation-based setup (Popek et al., 2017)

Like these systems, for capsule robot locomotion, Ankon Tech. developed a capsule endoscopy system consisting of a capsule camera and a sphere-shaped permanent magnet manipulator, shown in Figure 1.13, given with the patent in (Duan et al., 2015).



Figure 1.13 Magnetically controlled capsule endoscopy system (Duan et al., 2015)

In the literature, visual feedback is individually a challenging topic. The working space of the robot may be categorized as opaque and transparent. In opaque working spaces, radio frequencies, propagation (fluoroscopic, gamma ray, magnetic resonance imaging, etc.), ultrasound, odometrical, positron emitting marking, magnetic (magnetic marker, Hall effect sensors, external permanent magnet, etc.) detection techniques are used (Hu et al., 2016). In these techniques, there is no visual contact between the measurer and the measurand and the disadvantages can be listed as (not valid for all of them at the same time): The integration of detection equipment (position, assembly, etc.), requiring power supply with the robot, having toxic marker chemical on the robot, having side effects in the measuring environment due to the detection source (especially to human body). For transparent working spaces, almost all the researcher groups prefer visual imaging techniques. In 2D motions, just one camera is enough, in 3D motions, generally stereo vision (determining 3D position/orientation out of multiple image sources) technique is applied. In system integration, fast cameras with high resolutions cover small spaces thanks to the technological developments.

Many tests were run in test benches in 2D/3D specialized imitated environments and human phantom models, but when it comes to apply to a living/dead biological test subject, there are not many examples. A swarm helical fluorescent marked robots

with microscale are injected into a mouse and controlled by using Helmholtz coils setup (Servant et al., 2015), shown in Figure 13.

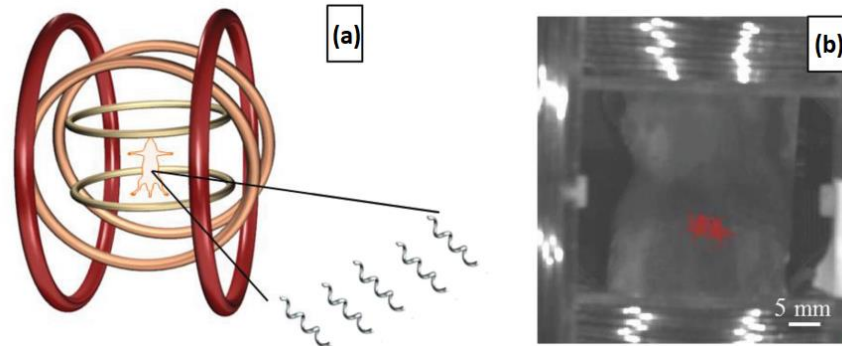


Figure 1.14 Swarm robotic test in a mouse (a) test bench setup (b) visual feedback (Servant et al., 2015)

After dead-eye tests, a needle-typed robot is tested in an anesthetized rabbit eye using OctoMag setup (Ullrich et al., 2013), shown in Figure 1.15. In this work, the transparency of the eye is used for visual position feedback.



Figure 1.15 Microrobot test in rabbit eye placed into OctoMag setup (Ullrich et al., 2013)

For colonoscopy applications, a pig is used for capsule robot manoeuvring (Ciuti et al., 2010), shown in Figure 1.16.



Figure 1.16 In vivo wireless capsule trials on female pig (Ciuti et al., 2010)

1.4 Research Gaps

According to the extended literature survey, the research gaps arise as follows:

- With the literature review, around the world, it is believed that the researchers are focusing on magnetically locomoted microrobot systems. Thus, it is believed that the conventional methods will be changed with these in the future. However, the increasing motion capability adds more complexity to EMA systems and there are no compensation systems to lower the complexity.
- The literature shows that the fundamentals were studied using a pair of EMAs, but after the investigations of multiple EMAs, the researchers mostly found former concept insufficient and left it for the ones with multiple ones. So that currently the new developed systems are generally not based on a pair of EMAs.
- There is no study using the proposed manipulator couple in the literature. This may open a path for the future applications.

- EMAs generally did not have a specialized design for mobile EMAs that parameters like weight should also be considered.
- Considering the literature, it is observed that there is a big gap that microrobot applications considering aneurisms were not at a proper level. Researchers generally studied the methods that a catheter is deployed.

The first motivation of this thesis is to use external magnetic actuators to generate a controlled magnetic field for the microrobot and locomote it in an untethered way. So that, it can be applied for a biomedical application that a microrobot can be deployed into a living creature body. As mentioned in Section 1.1, the microrobot locomotion using external magnetic field are thought to be one of the most effective methods in biomedical applications.

The second motivation of this thesis is to investigate and study the external magnetic field generation system using the philosophy to derive the electromagnetic actuator complexity to manipulator motions. This philosophy fundamentally aims to use a pair of electromagnetic actuators (EMAs) and constant current flowing through them. Two forms of magnetic field required for microrobot general motion are provided by changing the distances of the actuators. Also, the required spatial positioning of the actuators is provided using robot manipulators. Thus, the complexity required to provide 5-6 DOF microrobot motion using multiple EMAs is derived to robot manipulators, lowering the complexity needed by each system.

The third motivation of this thesis is to study a manipulator system concept which can be applied in biomedical applications for human body. For the basis of the applications, a concept manipulator system which is shown in Figure 1.17 was developed. This system consists of a couple of positioning manipulators: parallel and subsidiary manipulator. In the literature, this kind of manipulation system was not utilized for the specified purpose which is mentioned in the fourth motivation. Also, it was found out that using a nonmobile EMA system was also more popular. Also, parallel manipulator is not a common method for this kind of operations since mostly

researchers needed an end-effector and a series manipulator was mostly a better solution since it can provide macro-positioning.

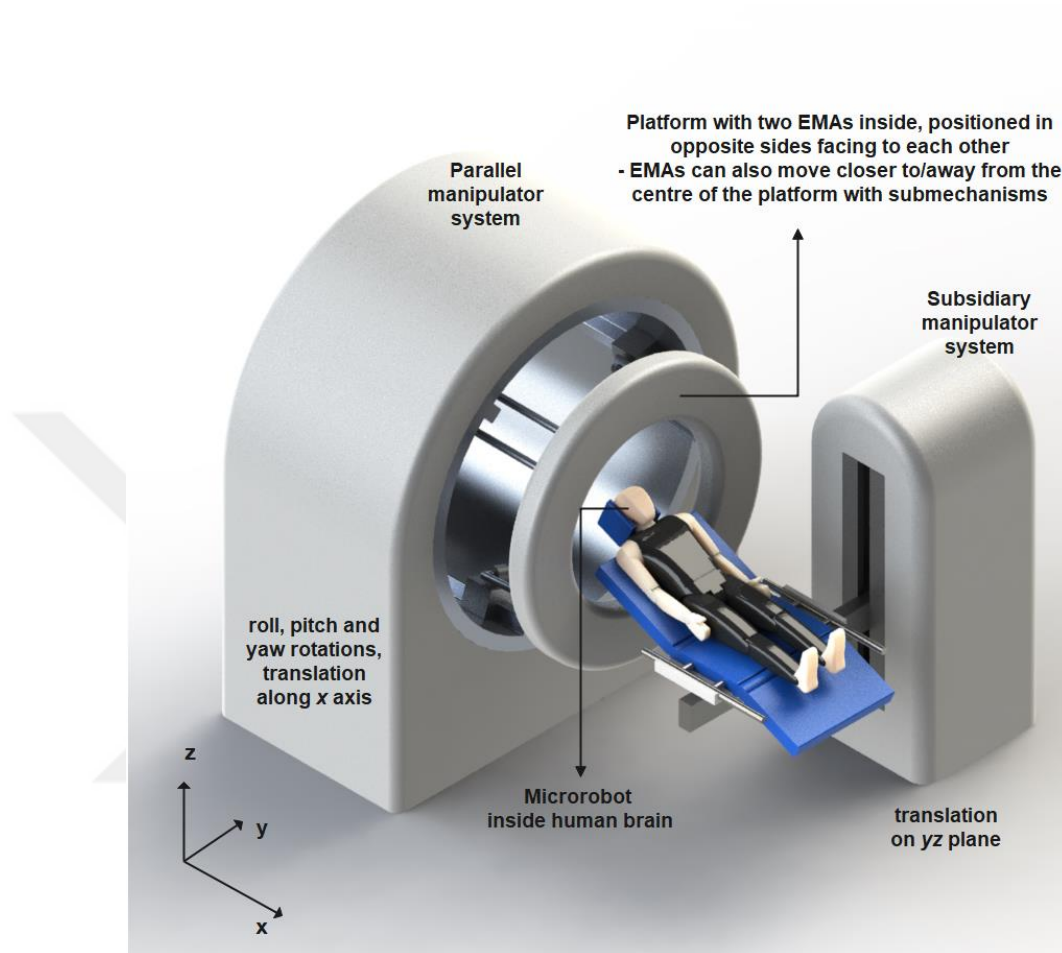


Figure 1.17 A concept work of the desired micromanipulation system

The fourth motivation of this thesis is to provide a method for the treatment of cerebral aneurisms. Aneurisms are the balloon shaped deformations which may occur at the wall of the blood vessels. Even there are treatment methods with open surgeries and close surgeries using catheter, for some situations it can be risky or impossible, especially the aneurisms occurring inside the brain. These locations might be very tricky to reach, very narrow to proceed using a catheter, or not reachable without severe damage with an open surgery. It is believed to provide a navigation method to provide a solution where the aneurism occurs.

1.5 Objectives and Contributions of the Thesis

The main contribution of this study is to provide a manipulation system approach especially for the treatments like cerebral aneurysm. The proposed concept was adapted to a prototype model which similar and can be more easily manufactured. Thus, it is planned to contribute to the subject of untethered microrobot manipulation using one EMA pair with an experimental validation of applicability. To contribute to the research gaps that arise from the extended literature survey, followings are the objectives of this thesis study.

- Investigation of the microrobot dynamics using general motion equations and providing by experimental data,
- Analysis (using a commercial engineering simulation program COMSOL), design and manufacturing of EMAs considering some goal parameters, experimentally calibrating the manufactured models,
- Coming up with a manipulator system concept work which may provide a solution, then adapting to an applicable prototype system,
- Analyses, designs, manufacturing and experimental investigations of manipulators and mechanisms: Euclidean plane parallel manipulation system, subsidiary manipulation system and EMA linear mechanism,
- Design of Robot Operating System (ROS) based software system, coming up with other hardware/software components,
- Experiment and investigations of the system using closed-loop control, achieving motions with open and constrained environments with different working modes.

CHAPTER 2

MICROROBOT AND MICROROBOT LOCOMOTION

2.1 Introduction

This chapter includes the microrobot operation principle, microrobot structure and design parameters for the applications. The fundamental microrobot locomotion is based on homogenous magnetic field and magnetic field gradient configurations, providing torque and force effects onto the microrobot. These configurations include a pair of EMAs facing to each other and the microrobot (also microrobot environment) is positioned between them. Each EMAs can be perpendicularly moved further or closer to the microrobot environment providing transition between these configurations. The microrobot structure consist of N35 grade NdFeb (neodymium) permanent magnets, which can be easily provided from the market in different shapes with tiny dimensions. The microrobot environment was also studied. The analyses cover the general motion equations for a prior microrobot design.

2.2 Microrobots

Microrobots are called the manipulated micro-scaled objects to accomplish their tasks and all the aspects of their structures may vary depending on the entrusted task and desired motion parameters. In general, the microrobot structure can be inspected in numerous scopes: locomotion methods, shape and volume, materials, etc.

To accomplish the desired in vitro tasks, the most conventional method is to use micromanipulators (Cappelleri et al., 2012; Chen et al., 2017; Kim et al., 2004; Nogimori et al., 1997; Schaffer et al., 2019) which consist of micro tweezer structures. For the applications that these micro manipulator tweezers cannot be deployed, microrobots come into consideration.

Basically, the general microrobot structure can consist of two types: with wire or wireless. The microrobot can have the required locomotion actuator on board and the energy transmission can be provided using wires. Wireless manipulation methods

come in handy when especially the microrobot is aimed to be deployed into the body. So that, the structure branches to two different categories: on-board powering and external powering. On-board powering principle includes all the components including actuator, battery, and all kind of electronics on the microrobot. Considering these specifications, all the fields have their own challenges which are not convenient to apply in the common technologies. Intense charging capacities are required with non-traditional batteries. Electronics are directly dependent to micro fabrication and micro scaled design of the digital circuitry. Thanks to Very-Large-Scale-Integration (VLSI) and lithography techniques, digital controllers can be custom-designed and fabricated up to some dimension limits. Small-scaled actuator technologies like propellers, tweezer motors, etc. and functional electronics technologies in microscales like micro cameras can be defined in microelectromechanical systems (MEMS) technique, but they are not at a required level for manufacturing and energy consumption efficiencies. Briefly, each of the components have their challenges and should finally be optimized exclusively for the microrobot and working environment depending on the desired locomotion specifications.

External powering comes in two facts: to harvest energy and directly move by external power. By harvesting energy, the robot may not need a powerful battery whose capacity must be large enough to accomplish the goal. Energy transmission can be accomplished using magnetic field easily thanks to the magnetic permeability of human body, so that the robot may harvest electricity without much loss in the way. Unfortunately, in submillimetre dimensions, energy harvesting for microrobots have not advanced to a proper level.

2.2.1 Wireless Microrobot Actuation

Researchers worked on the wireless actuation methods and came up with different methods. Electrical actuators can provide locomotion to the microrobot generally by deformations like bending/folding in the material. This motion might be applied using micro actuators on joints (Jager, 2000), with the temperature gradient with electrical structure might on flexible robot (S. Zhang et al., 2021), or an externally provided heat.

Light based optical actuators (optical tweezers) (Bustamante et al., 2021; Zhou et al., 2017) are one of the most common actuators, especially used for manipulating atom/molecule/cell sized objects. Focused laser beam uses Lorentz force basis, simply trapping the object inside the beam. Thermal locomotion can be counted Different from these, biohybrid actuators specialize the actuators with biological parts like bacteria, muscle cell, etc. to generate the required motion for the locomotion/task, reviewed in (Ricotti et al., 2017). Another method acoustic propelling uses waves to propel the microrobot (Aghakhani et al., 2022). The other promising method is locomotion using external magnetic field.

2.2.2 Electromagnetic Actuation and Locomotion Methods

This part only inspects locomotion using external magnetic field. After their studies, researchers found biomimicry the most efficient way to achieve microrobot structures (Abbott et al., 2010; Barbot et al., 2016; Gao et al., 2012, 2014; Ghanbari & Bahrami, 2011; Ghost & Fischer, 2009; Hill et al., 2010; Peyer, Tottori, et al., 2013; Peyer, Zhang, et al., 2013a; Purcell, 1977; Qiu et al., 2014; Tottori et al., 2012; L. Zhang et al., 2009). Some of the developed magnetically controlled robot structures can be seen in Figure 2.1. Also, the microrobot structures and their actuation methods are given in Figure 2.2.

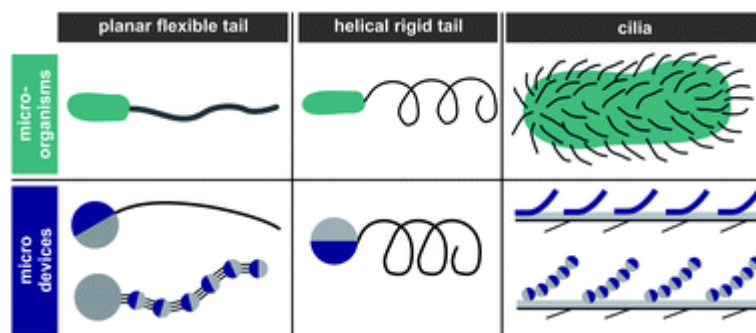


Figure 2.1 Bio-inspired microrobots (Peyer, Zhang, et al., 2013b)

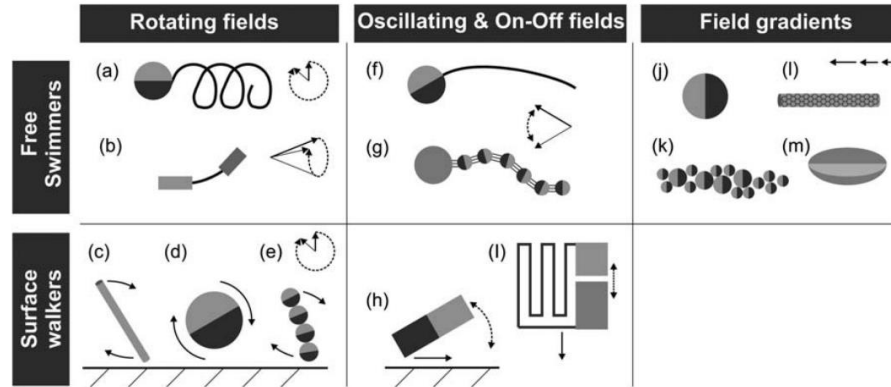


Figure 2.2 Types of microrobots and their actuation methods (Peyer, Zhang, et al., 2013b)

The robot locomotion types can be categorized as helical propulsion, travelling wave, pulling with magnetic gradient and clinical magnetic resonance imaging system.

Helical propulsion motion depends on robot rotation actuated by rotating magnetic field. The shape of the robots in helical propulsion is inspired from bacteria with flagella. The rotation of the flagella generates a translational motion. The material of this robot can show magnetic properties, or a top head at the tip of the helical with magnetic properties for propulsion with nonmagnetic like plastic helical are used. The recent progresses were inspected well in review by (Dong et al., 2022). Commenting on the literature works, helical type robots are one of the most studied microrobot structures.

Using a whip-like tail or body, the propulsion can be achieved using the travelling waves, inspired from cilia. The structure is designed in a flexible way that the body can respond the moves of the magnetic waves, manipulating the body with a whip or snake-like motion, generating a translational motion in the end. ON-OFF or oscillating magnetic fields are used for this type of motion. A fully inspired cilia type robot including tens of tails are difficult to manufacture in a precise way, so one-tail models are preferred.

The gradient type of robot designs is generally considered with the mission, shaping from a needle form for penetration to a chin-like form for particle transportation. Depending on the fundamental properties of the magnetic field, a force is applied onto the robot when a magnetic gradient is formed through the robot. This needle-like form

is one of the exceptional forms that is used in magnetic actuation methods but does not exist in biomimicry (has no equal in nature).

Surface walker robots are also controlled with rotating magnetic field, ON-OFF or oscillating magnetic fields. The motion depends on the fluid properties near to a surface like wall-effect (Israelachvili, 2010) or the structural properties.

2.2.3 *The Magnetic Gradient Actuation*

The magnetic gradient actuation method uses two fundamental general motion equation for torque and force. These are shown in Equation 2.1 and 2.2.

$$\mathbf{F} = v(\mathbf{M} \cdot \nabla)\mathbf{B} \quad (2.1)$$

$$\boldsymbol{\tau} = v(\mathbf{M} \times \mathbf{B}) \quad (2.2)$$

Here, v stands for robot volume, M for robot magnetization and B for external magnetic flux intensity. Using these formulations, the applied force F and torque τ can be determined. This way, one can change force and torque applied onto the robot just by changing the vector and the magnitude of magnetic flux intensity if robot volume and magnetization are realized constants.

Applying these principles to a microrobot with magnetic properties, the behaviour of the microrobot is given in Figure 2.3. A torque motion is utilized under homogenous magnetic field in the magnetic field direction, and under magnetic gradient a force exerts in the direction of the gradient.

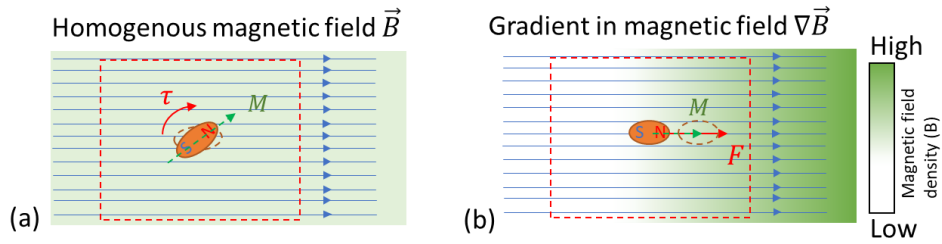


Figure 2.3 The motion of the microrobot (a) homogenous magnetic field causing τ torque (b) the magnetic field gradient causing F force.

Providing the magnetic actuation principle, a general layout of the actuation system using a pair of EMAs is given in Figure 2.4. EMAs are positioned facing each other on the same spatial axis, and microrobot is applied on the same axis. D_1 and D_2 presents the distances from microrobot to EMAs' surfaces.

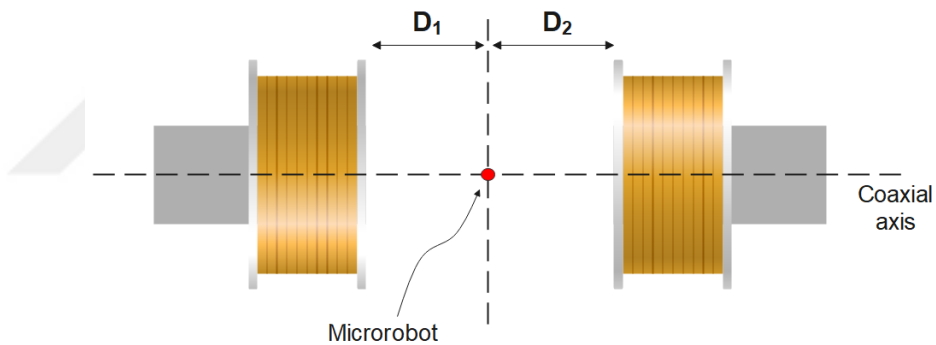


Figure 2.4 General layout using two EMAs with microrobot

The further details and inspections with EMA systems are given in the next chapter.

2.3 Microrobot Analysis and Manufacturing

In specialized terms of the study, microrobots are basically the agents that should accomplish the task given in the field by the actions of movement, grabbing, etc in the task space. The important part here is to complete the goal, thus a microrobot can have a complex or basic structure if it works.

In this application, the goal is to provide a basic structure for the microrobot which should be utilized for positioning, nothing else. Thus, specialized parts like gripper, etc. are not required with the structure. A sample permanent magnet used in structure is shown in Figure 2.5.



Figure 2.5 N35 grade cylindrical permanent magnet with 1 mm to 1 mm dimensions (Kahveci et al., 2021)

2.3.1 Verification of Permanent Magnet Values

An experiment system was designed to measure the magnetism values of the permanent magnets have. According to the designed measurement principle, magnetic field measurement will be made with a gaussmeter probe from a certain distance from the permanent magnet and the desired values of the permanent magnet will be reached by replacing it in the theoretically known equations.

The required magnetism value is called Remanence (B_r) expressing the residual magnetization of the object/material with the absence of external magnetic field ($H=0$). Considering the hysteresis curve in electromagnetism, the permanence point of a permanent magnet B_r is as in Figure 2.6.

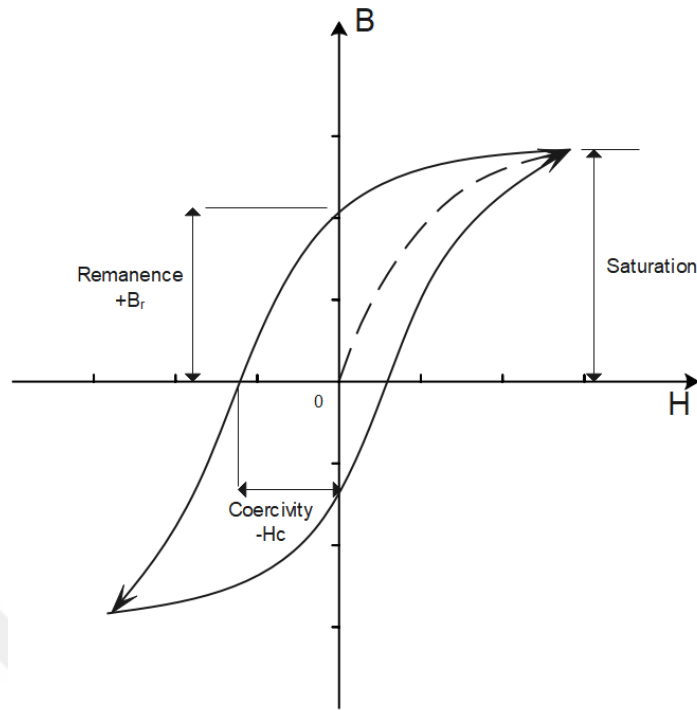


Figure 2.6 Hysteresis curve and remanence value

The acknowledged magnetism formula in linear operating regions and the magnetic field formula including the remanence point is as in Equation 2.3:

$$B = \mu_0 \mu H + B_r \quad (2.3)$$

The formula used to find the magnetization variable of permanent magnets in the force and moment equations, which are the general equations of motion, is as follows in Equation 2.4.

$$M = \frac{1}{\mu_0} B_r \quad (2.4)$$

The uncomplicated magnetic field formula for a disk or cylindrical permanent magnet is given below and the distances are as in Figure 2.7 and the related formulation in Equation 2.5.

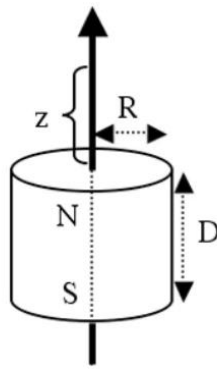


Figure 2.7 A cylindrical permanent magnet flux density

$$B = \frac{B_r}{2} \left(\frac{D+z}{\sqrt{R^2+(D+z)^2}} - \frac{z}{\sqrt{R^2+z^2}} \right) \quad (2.5)$$

Here, z stands for the distance from face to measurement point, R for radius, D for thickness of the permanent magnet.

Accordingly, the magnets were placed directly on the measurement probe, taking into account the dimensions of the permanent magnets to be measured and the decrease in the distinguishability of the measurement sizes as the distance increases. The sensor position of the probe is as in Figure 2.8. The positioning of the magnet is given in Figure 2.9.



Figure 2.8 The tip of STD18-0404 F.W.Bell Gaussmeter measurement probe and its embedded sensor



Figure 2.9 The positioning of the permanent magnet on the probe

As can be seen in the measuring probe specifications document provided by the manufacturer, the sensor is positioned at the midpoint of the probe. Also, the thickness of the probe was measured as 1.08 mm with the help of calliper. This value has been confirmed to be within the tolerance range of the probe dimensions in the document. That is, in this case, 0.54 mm is taken as the z value in the formula.

Accordingly, the measurements and the B_r values obtained with the measurements are given in the Table 2.1 (it should be noted that N42 was not used in the applications).

Table 2.1 Remanence measurements of the permanent magnets

Sample	Grade	Cylinder height	Cylinder diameter	Measured magnetic field	Calculated B_r value	General B_r values for this grade
Type#1	N35	1	1	130.6 mT	1201 mT	1.17-1.22 T
Type#2	N42	1	1	142.2 mT	1308 mT	1.28-1.32 T
Type#3	N35	1	2	214.4 mT	1180 mT	1.17-1.22 T

2.3.2 *Microrobot environment*

In the literature, using different robot structures, actuators, actuation methods and operation aims, researchers used different kinds of microrobot environments. These environments share some common properties. First, all the environments are in fluid state. Secondly, the environments have low Reynolds number (i.e., a constant fluid flow does not exist). Thirdly, they have Newtonian characteristics that the viscosity does not change with the velocity of the microrobot.

The most preferred are water, silicon oil, sunflower oil, and glucose syrup mixture. It should be noted that water has viscosity value of 1 mPa.s. Previously, it was studied in (Çetin et al., 2022) that the viscosity of the custom fluid was 557 mPa.s considering some conditions for the prior tests of the doctrine. The first condition was to have a system which the microrobot stays in the equilibrium state between sinking and floating. The second condition was to increase the stress value to observe the relationship between microrobot motion and the fluid.

In this thesis, the considered principles were nearly the same except a few. The aim was to increase the viscosity to be able to provide an ability to overcome physical structures, like opening a clogged vein, punching a vein wall, so on. Also, the environment with the flow increases the Reynolds number, so a fluid with higher viscosity may provide better controlling environment for motion. The buoyancy equilibrium was not considered this time with the expectation of sinking.

After some considerations and tests, castor oil was preferred as the microrobot environment. The fluid has the viscosity of was measured 1.03 Pa.s at 25° temperature.

2.3.3 *Defining the Needs*

At this stage, the magnetic force equation needs to be discussed. Even some of the parameters, especially related to the microrobot environment, are not clear, a starting

point for the microrobot (size, type, grade, etc. leading to volume and magnetization vector) should be decided.

The reference microrobot is a permanent magnet with N35 magnetic material (Br permanent magnetization approximately 1200 mT), 1 mm diameter and 1 mm height. This magnet was used as the base unit. Considering the orientation detection, the axis in z direction was desired to be longer, so that the considered model has 1 mm diameter and 2 mm height. Accordingly, the volume and magnetization of the microrobot are given in Equation 2.6-2.7.

$$V = \pi r^2 h = 1.5707 \times 10^{-9} \text{ m}^3 \quad (2.6)$$

$$M = \frac{1}{\mu_0} Br = \frac{1}{4\pi \times 10^{-6}} 1200 \times 10^{-3} = 95492.96 \frac{\text{A}}{\text{m}} \quad (2.7)$$

Here, μ_0 stands for vacuum permeability. Using these parameters, it can be seen that M does not affect if the magnet grade is different. The volume (i.e., the dimensions and the number of magnets) affects the equation. These parameters can be substituted into the general equation of motion and the magnetic field magnitudes required for motion can be found. At this stage, it is necessary to determine general motions. The free body diagram is given in Figure 2.10.

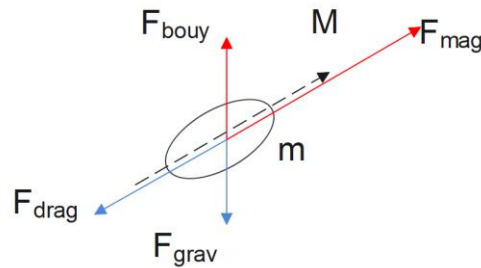


Figure 2.10 The acting forces onto the microrobot

Here, F_{mag} stands for generated magnetic manipulation force, F_{drag} for the drag force between the microrobot and the environment fluid struggling against the motion,

F_{grav} for the gravitational force of microrobot, and F_{bouuy} for the buoyancy force of the microrobot.

Assuming the buoyancy and gravity force equilibrium, or with other perspective providing the equilibrium with gravity compensation using magnetic field, on the motion axis the equation is given in Equation 2.8.

$$m\vec{a} - \vec{F}_{drag} = \vec{F}_{mag} \quad (2.8)$$

Here, m stands for microrobot mass, a for acceleration. The drag force in microrobot applications can be modelled in a few ways. It should be considered that in small scales, the law may also change. Stokes' law theory assuming a sphere shaped microrobot, results the drag force correlated the velocity. It should be noted that the drag force is morphologically related to the surface. The velocity force model is given in Equation 2.9.

$$\vec{F}_{drag} = C_d v \quad (2.9)$$

Here, C_d stands for the drag constant, and v for velocity. Returning to the previous equation, when a motion with constant speed occurs, an equilibrium with drag force and magnetic force, giving the drag coefficient value. In this form, it is difficult to find out a constant directly. Instead, if the magnetic field force is modelled with the form given in Equation 2.10, it would be possible to find out a constant relationship between the constants of the units.

$$\vec{F}_{mag} = C_m G_u(\epsilon) \quad (2.10)$$

Here, C_m stands for the magnetic constant, $G_u(\mathcal{E})$ for a correlation of force with the asymmetry parameter, which is studied in the next chapter.

2.3.4 Manufacturing of Microrobot

As stated in the previous subsection, the prior model was to use a cylindrical microrobot at the size of 1 mm diameter and 2 mm height. Updated after the applications, the prior model was used for the whole applications. This microrobot was painted to red colour for machine vision segmentation.



CHAPTER 3

ELECTROMAGNETIC ACTUATORS

3.1 Introduction

This chapter includes analyses, design, manufacturing, and calibration steps of the electromagnetic actuators. EMAs are deployed to provide the desired magnetic field form and magnitude to the Region of Interest (ROI). Apart from these, weight of EMAs were also a matter of consideration. First, a prior work was briefly presented that EMA design was studied. Then, EMAs used in the thesis were analysed, designed, manufactured, and then calibrated.

3.2 Magnetic Actuators in Microrobot Manipulation

Microrobot magnetic actuators can be categorized into two parts: electromagnetic and permanent magnet actuator systems.

In electromagnetic actuator systems, Helmholtz configuration is one of the most popular configurations, providing 6 DOF motion capability to the microrobot inside a limited area, using three pairs of EMAs. There exist many Helmholtz-like systems that were used for microrobot manipulation. OctoMag (Kummer et al., 2010) and MiniMag (Schuerle et al., 2013) actuators consist of eight actuators, also providing a limited ROI. Also, another proved system (Tasoglu et al., 2014) provides 6 DOF, using eight EMAs. Most of these electromagnetic systems are stationary systems and provide limited ROI area for control.

Permanent magnetic actuator systems generally supported with manipulators, providing the required positioning to the actuator. In (Mahoney & Abbott, 2014) and (Popek et al., 2017), permanent magnet actuators can provide gradient and rotating magnetic fields to capsule robots. There exists other works using permanent magnet actuators (Khalil et al., 2017).

It is concluded that stationary actuation systems are more trending than the systems that has programmable working space.

3.3 Actuator Configuration of EMAs

The fundamental microrobot locomotion is based on homogenous magnetic field and magnetic field gradient configurations, providing torque and force effects onto the microrobot. These configurations include a pair of EMAs facing to each other and the microrobot (also microrobot environment) is positioned between them. Each EMAs can be perpendicularly moved further or closer to the microrobot environment providing transition between these configurations. The configurations are given in Figure 3.1.

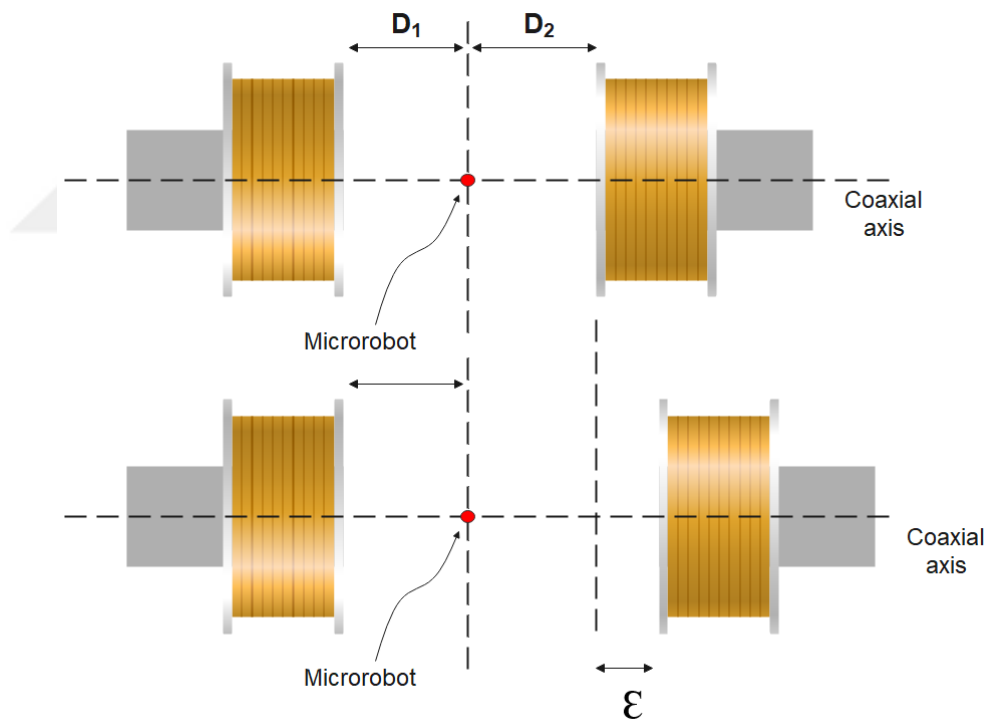


Figure 3.1 Homogenous magnetic field and magnetic field gradient configurations

Here, \mathcal{E} presents the asymmetry parameter for magnetic gradient configuration. Assuming that the current values are the same with both EMAs, aware of the opposite current flow directions, a homogenous magnetic field occurs at the centre of the

EMAs, as $D_1=D_2$. When moving away one of EMAs further away with ϵ , the generated magnetic field at the same point (i.e., onto the microrobot) loses its homogenous form, inducing a magnetic gradient. Using these two configurations, force and torque configurations can be applied. The related general motion equations acting onto the microrobot were given in the previous chapter.

3.4 Prior Analyses of a Different EMA

In electromagnetics, it is difficult to analytically calculate the magnetic field strength produced for complex structures. Generally, mathematical formulas can be extracted in cases with some special structures, e.g. for Helmholtz systems electromagnets are air-cored and the desired mathematical magnetic field can be calculated analytically. This is since the environment in which the magnetic flux circulates consists of only a single median (i.e., air). However, in systems with a different environment other than air (iron core in this case), a correlation can usually be made because of the data obtained as a result of measurements and simulations. This method is the most common method b.

A similar magnetic field analysis for EMA design was studied before. These analyses were simulated using COMSOL Multiphysics program. This prior study was about determining an EMA design by comparing the systematically calculated performances. Shown in Figure 3.2, the generated magnetic field between EMAs was segmented into categories and their parameters were used for determining a performance score. Also, in Figure 3.3 other performance criteria parameters were shown.

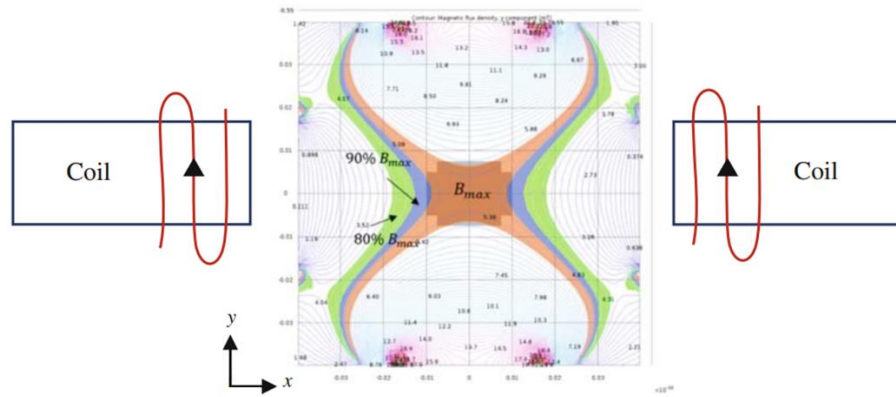


Figure 3.2 Homogenous magnetic field occurring in ROI (Region of Interest) on xy plane and classification of areas (Alasli et al., 2018).

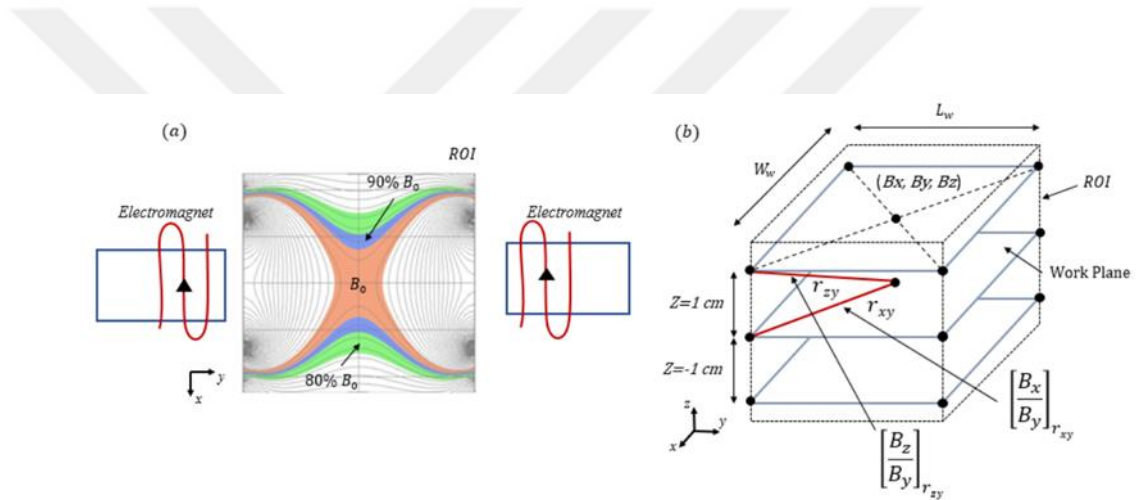


Figure 3.3 Analysis parameters (Alasli et al., 2019).

On Figure 3.3a, a magnetic field result occurring on a xy plane in Region-of-Interest (ROI) between the pair of coils is shown. The magnetic field occurring at the centre of the area is named B_0 and coloured areas derive within 10% portions while the middle area forms a uniform area, where the analyses have interest with the value and its dimensions. On Figure 3.3b, the interested analysis layers and measurement points are shown. W_w and L_w are distances between the points on xy plane, B_x , B_y , B_z are the components of the occurring magnetic field, r_{xy} and r_{zy} are the distances between the center and the related diagonal points, $[B_x/B_y]_{r_{xy}}$ and $[B_z/B_y]_{r_{zy}}$ are magnetic field component ratios in the related diagonals.

When inspected, it was realized that the electromagnetic actuators are mostly based on Helmholtz-like (air core coils) and iron-core cylindrical coils. It was inspected and realized that the same type of coils was used for iron-cored versions. So, it was decided to analyse and optimize a coil pair with iron core for our system.

The new coil design depended on some critical limitations. One of them was the weight constraint. As the system is mounted onto an industrial manipulator, the weight should be as light as possible. So that, the considered electromagnet structure is shown in Figure 3.4.

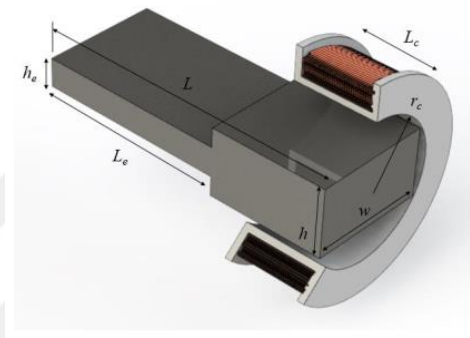


Figure 3.4 Dimensions of the cylindrical coils and its core in terms of w (width), h (height), L (length), L_e (extrusion length), h_e (extrusion height), L_c (coil length) and r_c (coil radius) (Alasli et al., 2019).

The analyses focused on the numerical computations. Depending on some parameters on the structure dimensions, some outputs were handled in decision phase. An EMA structure and parameters were decided, applied and manufactured (Alasli et al., 2018).

In this thesis, the considerations are a little bit different and handled in the upcoming subsections.

3.5 EMA Design

In this part, the design analyses and related details are presented.

3.5.1 Finite Elements Method and Mesh Decision

The meshes are closely related to the Finite Element Method's analysis. The bodies and the quality of the analysis are both defined by the meshes. The accuracy, especially with some specific conditions (e.g., boundary edges, curves, thin body parts, etc.), and the time necessary for the analysis solution are both affected by the meshes used. Depending on the form of the domains, mesh element shapes are also important (i.e., the parts that individual meshes are defined). Some parameters that are closely related to the phrase "mesh quality" are considered while comparing the analyses.

Mesh sizes should be lowered, and suitable mesh element shapes should be employed to achieve more accurate results. Increasing the number of meshes can be done using traditional methods (i.e., h and p refinements) as well as higher-degree interpolation functions, which generate meshes in a curve-shaped rather than linear shape with a smaller number of mesh elements, which is especially useful in regions where boundary faces/edges/corners (which require concentrated meshes for better accuracy) and complex domain shapes (which require concentrated meshes for better accuracy) (a curved domain edge is considered as polylines and the original shape is predicted). The Degrees of Freedom of the analysis are also increased by adding mesh nodes. In comparison, while adding more meshes may appear to improve accuracy in cases when there aren't enough nodes, doing so also extends the analysis time to days.

Two outcomes are examined for comparing analysis. Mesh element quality and error convergence are the two factors to consider. Skewness, maximum angle, volume versus circumradius, volume versus length, condition number, and growth rate are all used to calculate mesh element quality. The error value between the theoretical and approximated (analytical result) values is supposed to be the error value of convergence. Increasing the number of mesh nodes has no effect on the outcome value by this margin. The goal here is to compare the outcomes as the number of meshes is increased until the result value does not dramatically change. If a professional FEM program is used, these findings are typically analysed and meshes regenerated to meet the stated error margins. Two outcomes are examined for comparing analysis. Mesh

element quality and error convergence are the two factors to consider. Skewness, maximum angle, volume versus circumradius, volume versus length, condition number, and growth rate are all used to calculate mesh element quality. The error value between the theoretical and approximated (analytical result) values is supposed to be the error value of convergence. Increasing the number of mesh nodes has no effect on the outcome value by this margin. The goal here is to compare the outcomes as the number of meshes is increased until the result value does not dramatically change. If a professional FEM program is used, these findings are typically analysed and meshes regenerated to meet the stated error margins. As a result, the user is only expected to choose the mesh configuration settings that best suit his or her needs to achieve the best possible physical result.

The COMSOL Multiphysics program was used to conduct the analysis. The program uses its automated features to produce mesh nodes based on linked parameters, which is highly useful for users. By applying some iterations, the mesh node performance is internally adjusted to reduce the error convergence.

Because of its low complexity, adaptable uniformity, and applicability to most domain forms, free tetrahedral meshing geometry in 3D was chosen in the studies.

Generally, the number of elements for the analysis model start is considered as literally unknown except the minimum and maximum size values of the meshing parameters (meshing minimum value cannot be larger than the minimum dimension of the domain). Mesh comparison model geometry consists of a ferrite core with dimensions of 101.6x25.4x25.4 mm rectangular prism and a multiturn coil (400 turns with 10 layers) wound around the core. This coil is paired with another coaxial pair and the gap between the coils including interested region is meshed as a rectangular prism which has more concentrated nodes.

A reference model and three models with denser meshes were used in the mesh comparison test. Figure 3.5 shows the reference meshing model (mesh sample 1), which has a DOF of 3375832. The middle box node distances were narrowed in other

mesh samples because the gathered information was included. 3791606, 6892850, 6469100, and 9512386 were the DOF of the other samples. Figure 3.6 shows the data, which demonstrate maximum changes of less than 1%. Furthermore, the iterative solution was FGMRES (Flexible Generalized Minimal Residual Method), and the tolerance was left at its default value of 0.001.

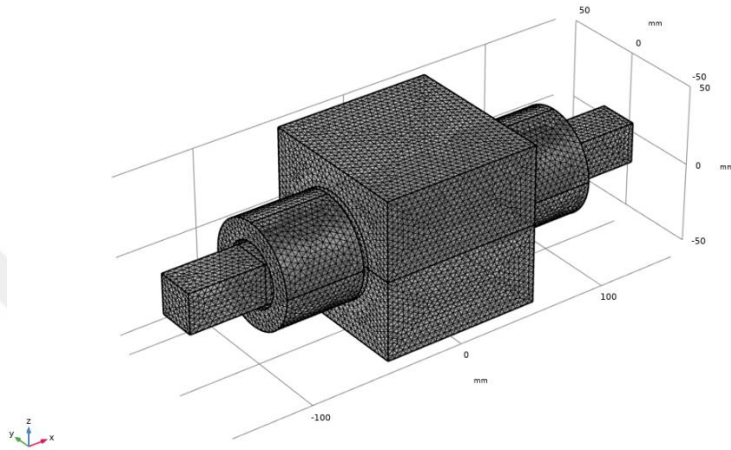


Figure 3.5 The reference meshing model for performance comparison

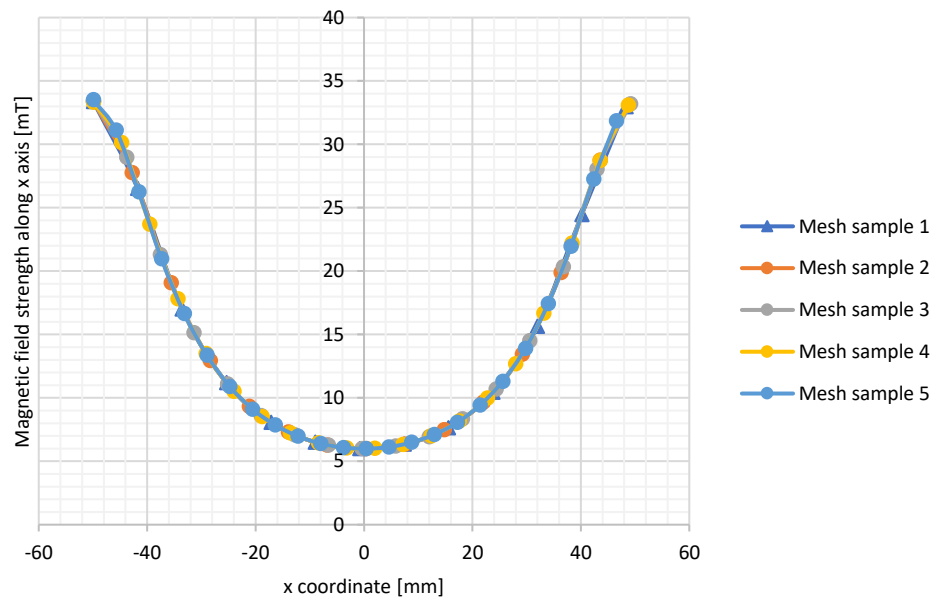


Figure 3.6 Mesh performance comparison of reference (mesh sample 1) and more dense meshed samples

There are some physical aspects to consider at this point. Accordingly, key points such as microrobot environment size, dimension values in the mechanism are decided accordingly. One of the most important physical limitations is that the EMA surfaces should not collide with the microrobot environment chamber or the tube-shaped apparatus below it, especially with the angled motions.

3.5.1.1 Homogeneous Magnetic Field Analysis (Variable Electromagnet Distances)

If a current flows in the same direction over the pair of electromagnets placed along the same axis, a homogeneous magnetic field is formed in and around the midpoint of the region located between the electromagnets. This homogeneous magnetic field creates an area with no magnetic field gradient value and is used for magnetic torque generation. The strength of the magnetic field is directly proportional to the amount of current.

The magnetic field values examined in this title are simulation results. These simulations were carried out with the COMSOL© Multiphysics program, which uses the finite element method. The homogeneous magnetic field value is considered as the homogeneity ratio as well as the magnitude of the magnetic field occurring at the midpoint. If the magnetic field size at the midpoint is accepted as 1 unit, three zones are formed as tolerant zones around it, and these zones are evaluated as homogeneity zones in the range of 105%-95%, 95%-90% and 90%-80%.

3.5.1.2 Magnetic Gradient Analysis (Variable Electromagnet Distances)

The magnetic field gradient is used as a variable in the force generation with the magnetic field. This gradient is applied in a system state, like the cases discussed in the previous section. The magnetic field gradient is applied on the particle as follows: while applying the homogenous magnetic field configuration, one of the EMAs is removed at a fixed distance value and a magnetic gradient begins to act on the particle that is no longer located at the midpoint, generating a magnetic force.

3.5.2 EMA Design Analysis

The analyses embrace an EMA model which has a simple structure consisting of ferrite core and copper wire. If the outcomes of the copper wire length and height were sum up:

- Increasing the number of winding layers:
 - Increases the magnetic field strength
 - Increases the change rate of magnetic field strength with each layer
 - Increases the weight
 - Increases the change rate of weight with each layer
 - Increases the outer radius of copper winding
- Increasing the copper length:
 - Increases the magnetic field strength
 - Decreases the change rate of magnetic field strength as it gets longer
 - Stops the magnetic field strength change at some point
 - Increases the weight with constant rate

So, for an ideal arrangement with a constant length ferrite core, the windings should be focused on the head part, and the outer radius of the winding should not be too large.

The model constraints were first suggested. The ferrite core was fixed to the size of 25.4x25.4x101.6 mm. The inner winding radius was fixed in a fixed carcass model, while the outer winding radius was limited by carcass assembly pieces. The diameter of the copper wire was set at 1 mm. Even if the wire diameter is known, some tolerances in the winding process occur for a non-ideal winding, according to past experiences. With a 5/4 ratio, this tolerance was stated (e.g., for a gap of 100 mm, only 80 windings can be applied). 2 A was set as the current. The analyses were carried out with the help of the COMSOL program.

The effect of the number of layers was first investigated. The winding length was adjusted at 50 mm for this analysis, which is exactly half of the core. The number of

layers tested ranged from ten to twenty, and various consequences were examined. Table 3.1 summarizes the simulation results. Figure 3.7, Figure 3.8, and Figure 3.9 show the plans that go with each other.

Table 3.1 Analysing the layer number effect

Number of layers	B_x Magnetic field strength along x axis [mT]	Iterative change with B_x [mT/layer]	Weight of copper [kg]	Weight ratio referencing to 10 layers	B_x ratio referencing to 10 layers
10	5.9729	0	0.4421	1	1
11	6.6962	0.7233	0.4961	1.122	1.1210
12	7.4379	0.7417	0.5518	1.248	1.2452
13	8.2002	0.7623	0.60929	1.378	1.3729
14	8.9784	0.7782	0.66854	1.512	1.5031
15	9.7753	0.7969	0.72956	1.65	1.6366
16	10.59	0.8147	0.79234	1.792	1.7730
17	11.422	0.832	0.85690	1.938	1.9123
18	12.267	0.845	0.9232	2.088	2.0537
19	13.128	0.861	0.9913	2.242	2.1979
20	14.003	0.875	1.0611	2.4	2.3444

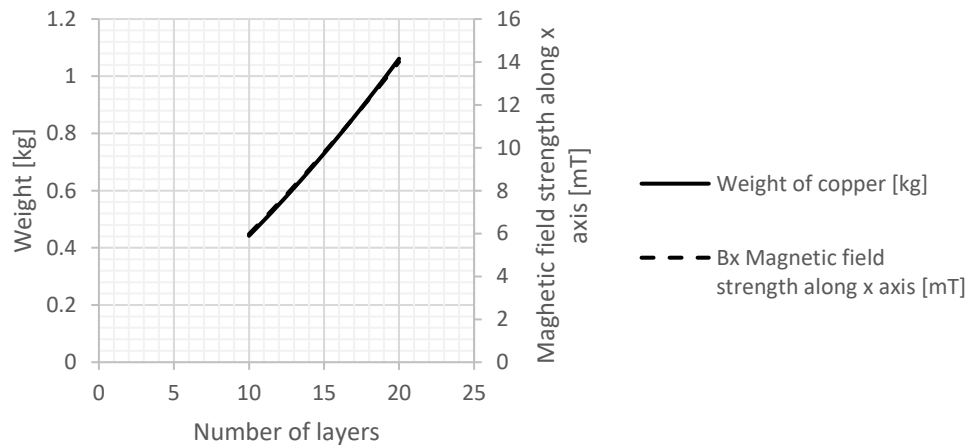


Figure 3.7 Effect of layers in magnetic field strength and weight

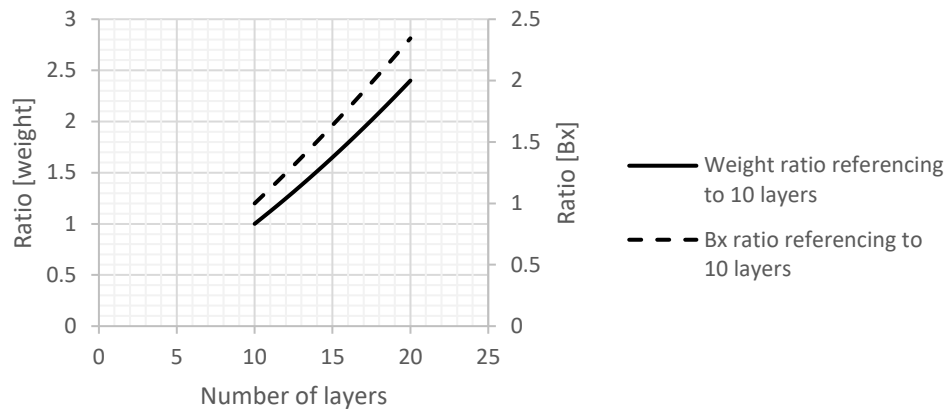


Figure 3.8 Effect of layers in magnetic field strength and weight shown as ratio

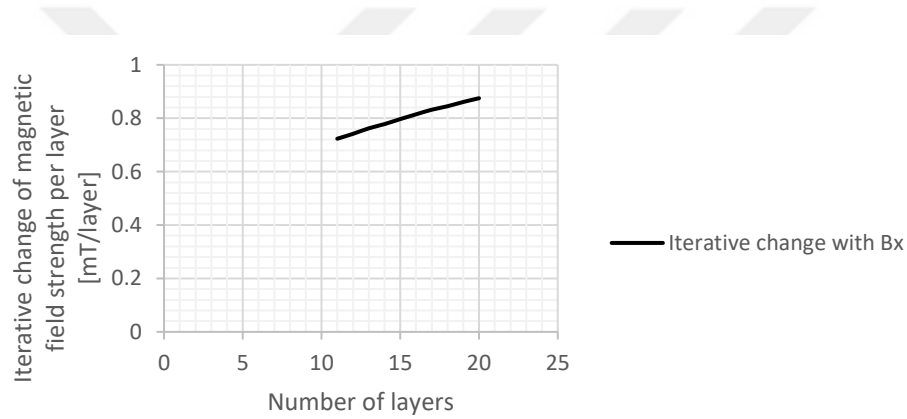


Figure 3.9 Effect of each layer in magnetic field strength

The effect of winding length was also examined, with the number of layers set to ten. Table 3.2 displays the results. Figure 3.10, Figure 3.11, and Figure 3.12 show the plans that go with each other.

Table 3.2 Analysing the winding length effect

Number of layers	Winding length [mm]	Bx Magnetic field strength along x axis [mT]	Iterative change with Bx [mT/mm]	Weight of copper [kg]	Weight ratio referencing to 10 layers	Bx ratio referencing to 10 layers
10	10	1.3907	0	0.0884	1	1
10	20	2.7009	1.3102	0.1768	0.5	1.9421
10	30	3.9103	1.2094	0.2652	0.3333	2.8117
10	40	5.0031	1.0928	0.3537	0.25	3.5975
10	50	5.9729	0.9698	0.4421	0.2	4.2948

Table 3.2 Continues

10	60	6.806	0.8331	0.5305	0.1666	4.8939
10	70	7.5028	0.6968	0.6190	0.1428	5.3949
10	80	8.0631	0.5603	0.7074	0.125	5.7978
10	90	8.4887	0.4256	0.7958	0.1111	6.1039
10	100	8.762	0.2733	0.8843	0.1	6.3004

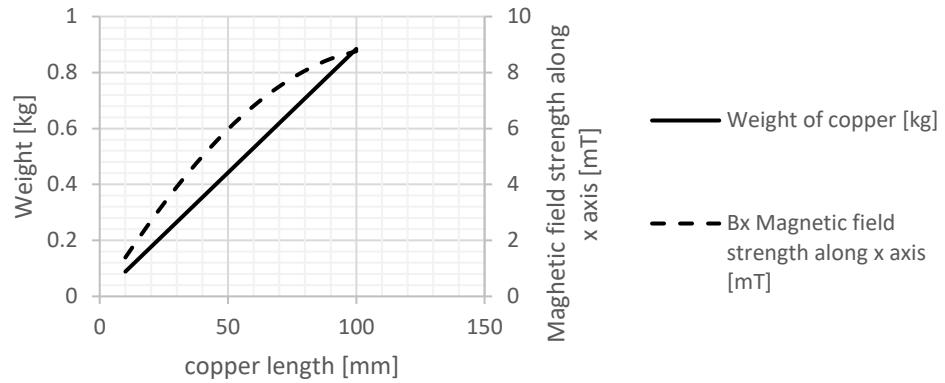


Figure 3.10 Effect of winding length in magnetic field strength and weight

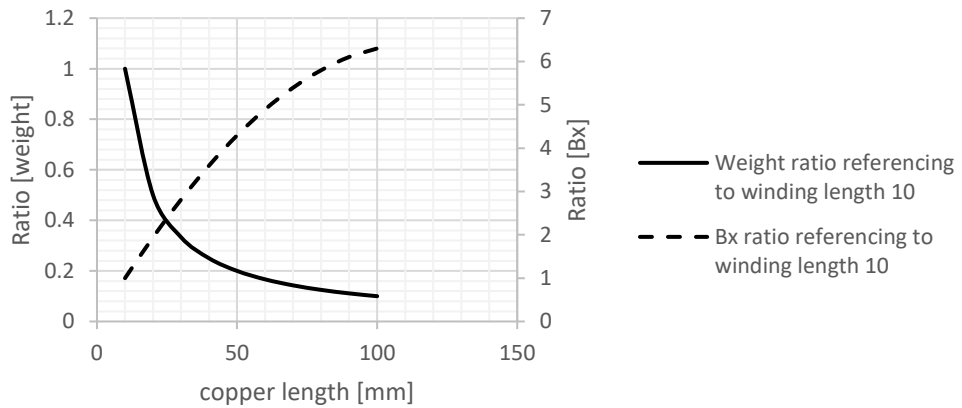


Figure 3.11 Effect of winding length in magnetic field strength and weight shown as ratio

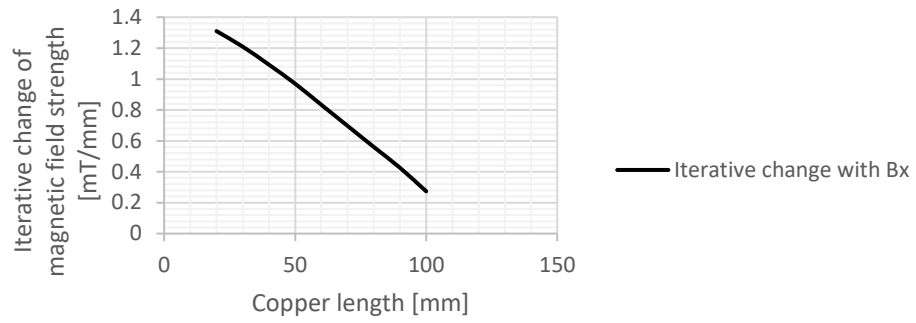


Figure 3.12 Effect of each winding length in magnetic field strength

After reviewing these results and weighing the benefits and drawbacks, it was determined to employ 15 layers for windings. Because the analyses were done with 10 layers, the winding length was double-checked using 15 layers. Table 3.3 shows the corresponding outcomes. The plots that go with it can be found in Figure 3.13, Figure 3.14 and Figure 3.15.

Table 3.3 Analysing the winding length effect

Number of layers	Winding length [mm]	Bx Magnetic field strength along x axis [mT]	Iterative change with Bx [mT/mm]	Weight of copper [kg]	Weight ratio referencing to 10 layers	Bx ratio referencing to 10 layers
15	10	2.3426	0	0.1459	1	1
15	20	4.4946	2.152	0.2918	0.5	1.9186
15	30	6.4569	1.9623	0.4377	0.3333	2.7562
15	40	8.219	1.7621	0.5836	0.25	3.5084
15	50	9.7753	1.5563	0.7295	0.2	4.1728
15	60	11.115	1.3397	0.8754	0.1666	4.7447
15	70	12.232	1.117	1.0213	0.1428	5.2215
15	80	13.132	0.9	1.1672	0.125	5.6057
15	90	13.821	0.689	1.3132	0.1111	5.8998
15	100	14.267	0.446	1.4591	0.1	6.0902

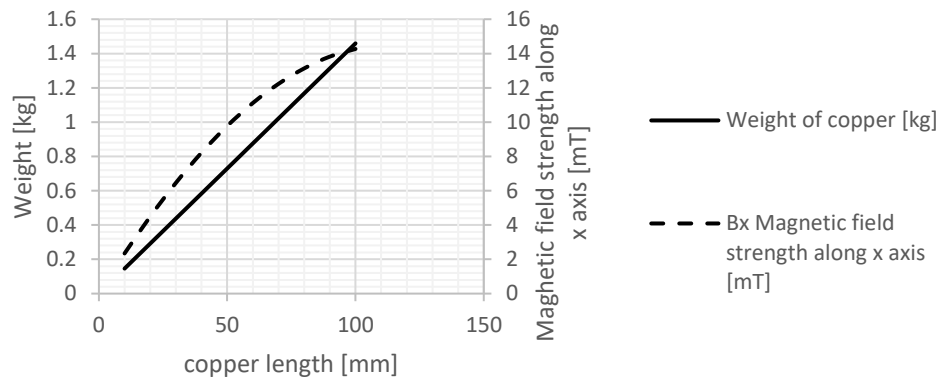


Figure 3.13 Effect of winding length for 15 layers in magnetic field strength and weight

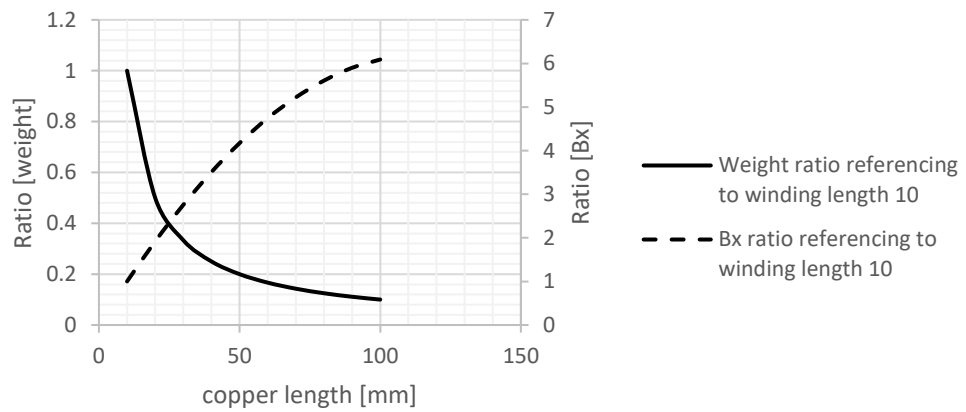


Figure 3.14 Effect of winding length for 15 layers in magnetic field strength and weight shown as ratio

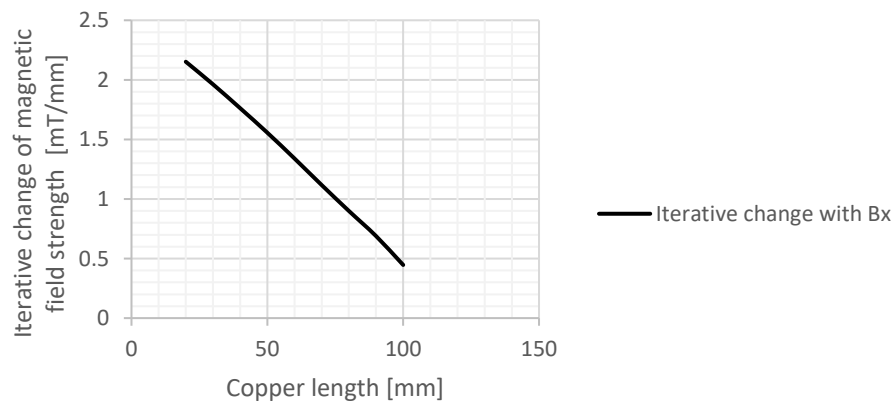


Figure 3.15 Effect of each winding length for 15 layers in magnetic field strength

Based on the findings of the analysis, the manufacturing parameters were determined to be 15 layers for the number of layers and 50 mm for the winding length. Considering only the copper and ferrite weights, the final actuator should weigh roughly 1 kg.

3.6 EMA Manufacturing

The finalized design parameters, the manufactured EMA is given in Figure 3.16. The design was shaped to be compatible with the adaptor component at EMA liner motion mechanism. The parameter for the manufactured EMA is given in Table 3.4. It should be noted that these parameters are the same with both EMAs, with almost same weight values.

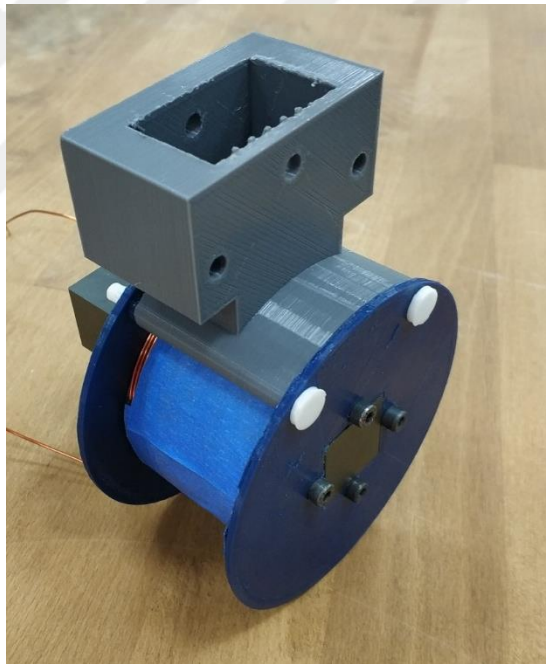


Figure 3.16 Manufactured EMAs

Table 3.4 Design and manufactured model parameter comparison

Design parameter	Expected	Manufactured
Number of layers	15	15
Number of turns for each layer	40	43
Total number of turns	600	645

Table 3.4 Continues

Total weight of copper (For 645 turns)	783 gr	824 gr
---	--------	--------

Considering these values, the finalized model for EMAs and the platform is given in Table 3.5.

Table 3.5 Weight summary for EMAs and the moving platform

Weight parameters	Value
EMA (x1 times)	1250 gr
Moving platform	3500 gr
Total	6000 gr

3.6.1 *EMA Calibration*

The manufactured EMA couple were required to be calibrated. To provide this calibration environment, a KUKA robot manipulator was used. Compatible adaptors provided symmetrical positioning as a F.W.Bell 5180 gaussmeter probe was positioned between them. The mock-up system and the calibration probe are shown in Figure 3.17.

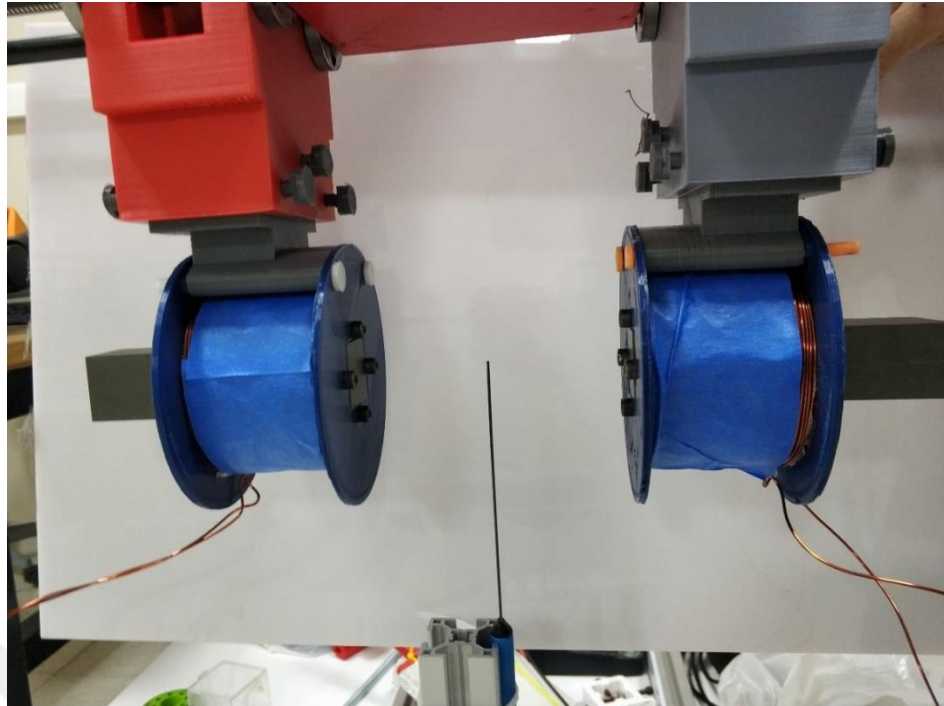


Figure 3.17 Calibration setup with gaussmeter probe

The referencing of the probe was done using physical contracting to one of EMA surface. A method figure is given in Figure 3.18. Assuming the reference point is one of the bottom corners of the ferrite core, the sensor position and the probe face were put into contact to start the referencing. The spatial position of the probe sensor relative to EMA is known, so it can be precisely moved to centre point between EMA pair.

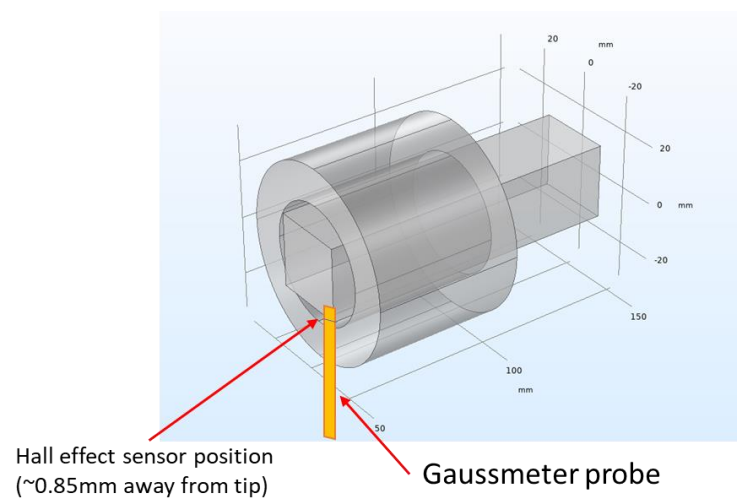


Figure 3.18 Position referencing the gaussmeter probe using the structure

The fabricated electromagnets were calibrated after being tested by measuring magnetic field strengths to determine the correlation with the simulation. A KUKA robot manipulator, an electromagnetic actuator mechanism, and an F.W. Bell 5180 gaussmeter were utilized to set up the measurement environment.

The electromagnetic actuator mechanism allows the actuators to be coaxially positioned over a wide range of distances. This mechanism is mounted to the tip of a KUKA robot manipulator with six degrees of freedom. The gaussmeter probe is placed on a platform, with the measurement face aligned with the actuator faces. Figure 3.19 and Figure 3.20 shows the configuration.

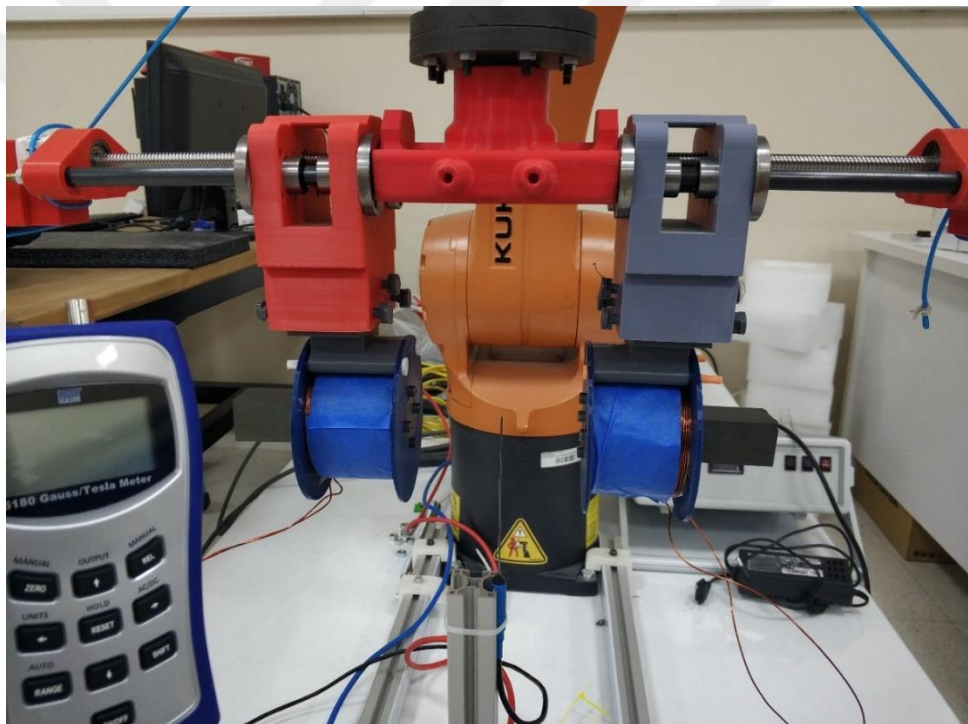


Figure 3.19 KUKA robot setup for calibration

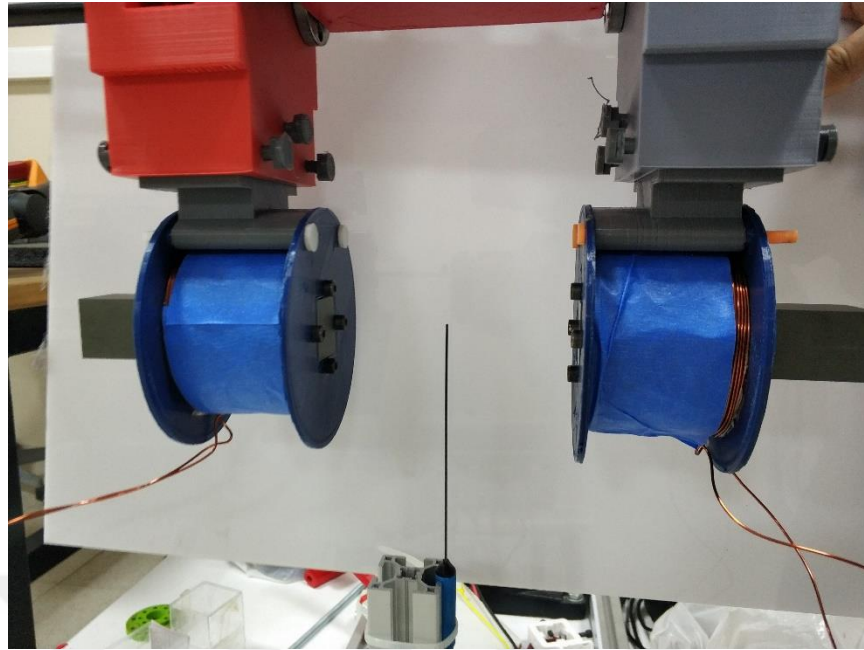


Figure 3.20 Magnetic field measurement setup

The calibration method for the setup was performed in the following order:

- The KUKA robot tip is properly positioned, especially in terms of vertically establishing EMAs and horizontally aligning the co-axis of EMAs with the KUKA global frame axis.
- Face distances are measured at multiple locations to assure accuracy. If not, the mechanism is properly set up.
- The gaussmeter probe is attached on a grounded platform.
- KUKA is used to align the gaussmeter with the electromagnet locations. The probe face (particularly the specific area where the Hall effect sensor is located) is touched to a reference point for referencing using this method, which is accomplished by moving KUKA (i.e., one of the ferrite core corners is selected here).
- The probe is accurately positioned at the centre point by moving KUKA since the reference point coordinates are known. The centre point coordinates are then read from the KUKA controller and noted.
- In symmetric setup, the location can also be double-checked by reversing one actuator current.

Four measurements were used in these comparisons: one for symmetric configuration and three for asymmetric configurations. These measurements were carried out using statistical data collecting principles, and each point was subjected to at least 10 measurements. The measuring point intervals were adjusted to 2 mm for symmetric configuration. However, because gradient values at the centre point are more essential in asymmetric configurations and need denser measurement points, the interval was fixed to 1 mm. The same current was provided because the simulations were run using a 2 A current.

The spacing between electromagnets was chosen to 100 mm for symmetric configuration. Figure 3.21 and Figure 3.22 show the simulation and measurement findings where coordinate 0 represents the centre point. The average ratio between measurement and simulation findings is 1.0298, and the average mean absolute error value is 0.3203 mT, according to the measurements.

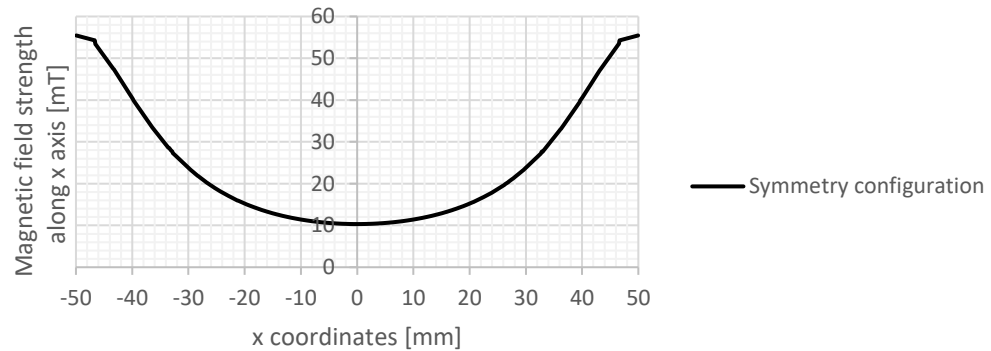


Figure 3.21 Symmetric configuration simulation result

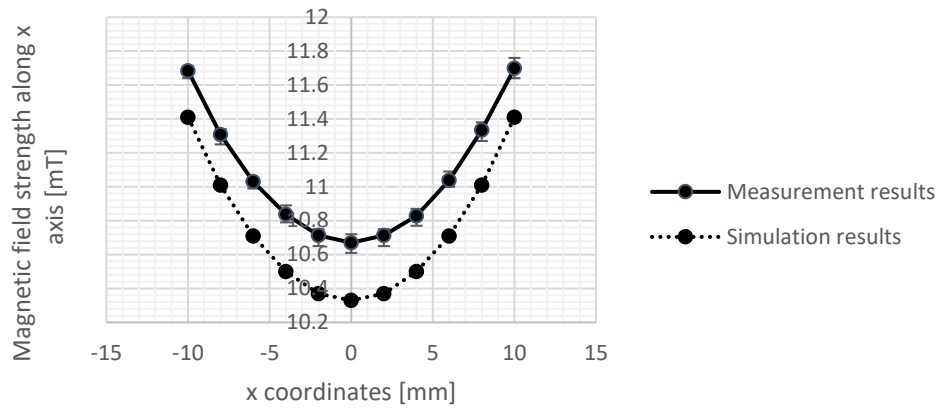


Figure 3.22 Symmetric configuration measurement results

The asymmetry parameter ε was chosen as 10 mm, 20 mm, and 30 mm for asymmetric configurations. In addition to the values determined in the symmetric configuration, the magnetic gradient values were calculated in the asymmetric configuration. Smaller x coordinate intervals produce more precise results when calculating the magnetic field gradient. However, it has been shown in previous reports that even reducing measurement point intervals and calculating the gradient using magnetic field strength and x coordinate interval can produce inconsistent and choppy results, both in measurements and simulations. As a result, 2nd order polynomial trendlines were used to analyse the gradient results. The magnetic field gradient value along the x axis can be calculated by forming this trendline regarding the x coordinate.

The first asymmetric configuration findings are shown in Figure 3.23, Figure 3.24, and Figure 3.25. According to the measurements, the average ratio between measurement and simulation findings was 1.0620, and the average mean absolute error value was 0.5384 mT. With a ratio of 0.9193 to the simulation result computation, the measured magnetic field gradients were calculated to be 0.0741 mT/mm.

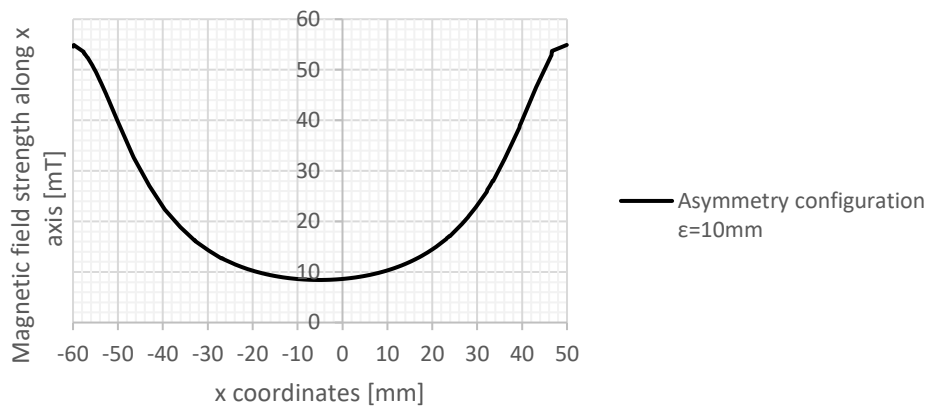


Figure 3.23 Simulation results of asymmetry configuration $\epsilon=10 \text{ mm}$

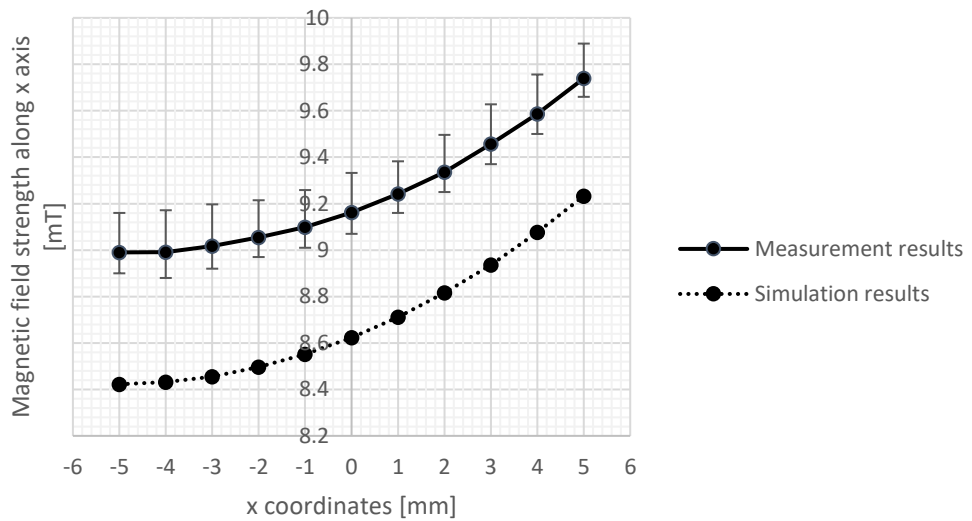


Figure 3.24 Comparison of measurement and simulation results of asymmetry configuration $\epsilon=10\text{mm}$

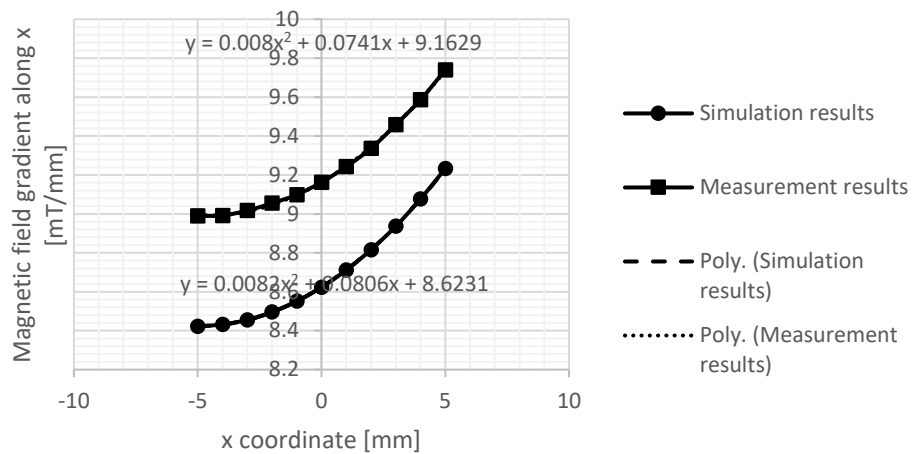


Figure 3.25 Magnetic field gradient comparison of asymmetry configuration $\epsilon=10 \text{ mm}$

The second asymmetric configuration findings are shown in Figure 3.26, Figure 3.27, and Figure 3.28. According to the measurements, the average ratio between measurement and simulation findings was 1.0724, and the average mean absolute error value was 0.5470 mT. With a ratio of 0.9145 to the simulation result computation, the measured magnetic field gradients were calculated to be 0.1155 mT/mm.

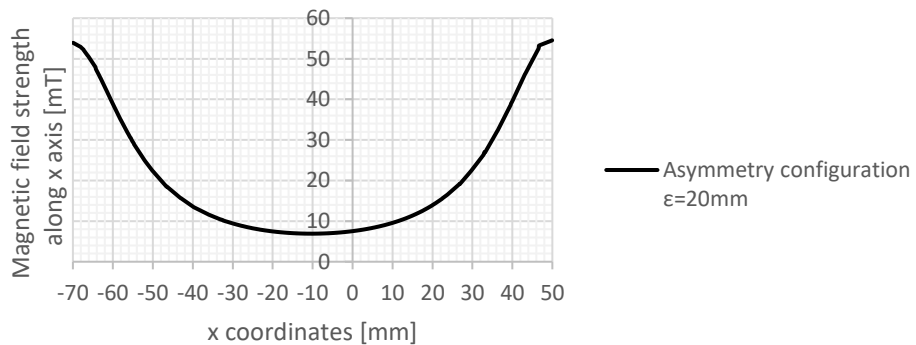


Figure 3.26 Simulation results of asymmetry configuration $\epsilon=20 \text{ mm}$

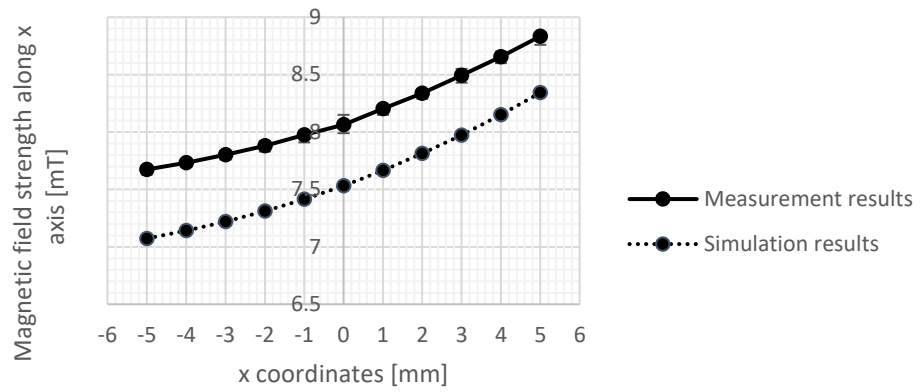


Figure 3.27 Comparison of measurement and simulation results of asymmetry configuration $\epsilon=20mm$

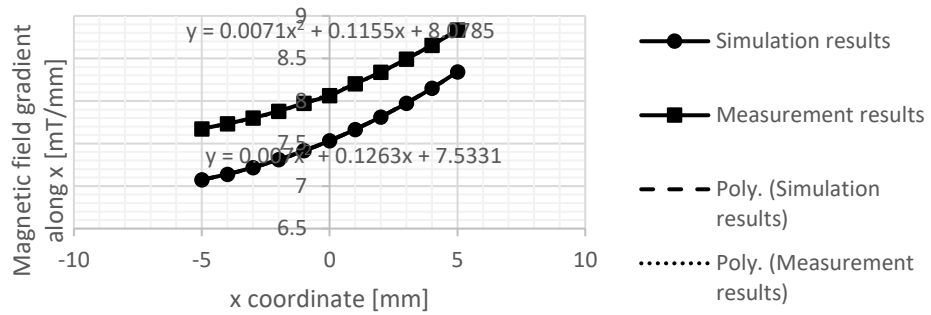


Figure 3.28 Magnetic field gradient comparison of asymmetry configuration $\epsilon=20mm$

The third asymmetric configuration findings are shown in Figure 3.29, Figure 3.30, and Figure 3.31. According to the measurements, the average ratio between measurement and simulation findings was 1.0835, and the average mean absolute error value was 0.5678 mT. With a ratio of 0.9135 to the simulation result computation, the measured magnetic field gradients were calculated to be 0.1405 mT/mm.

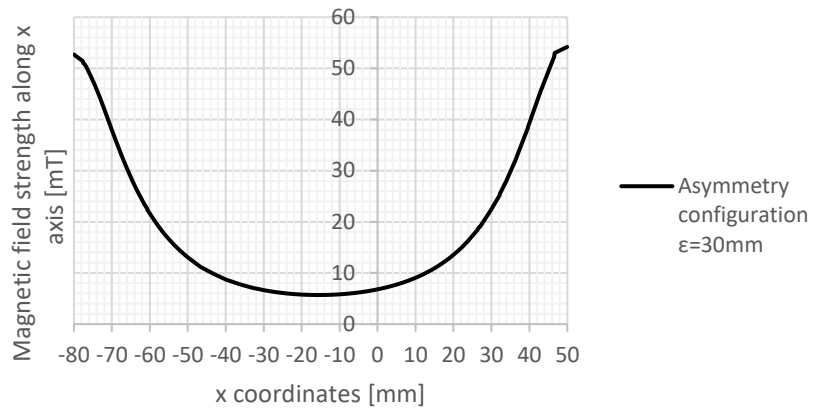


Figure 3.29 Simulation results of asymmetry configuration $\epsilon = 30 \text{ mm}$

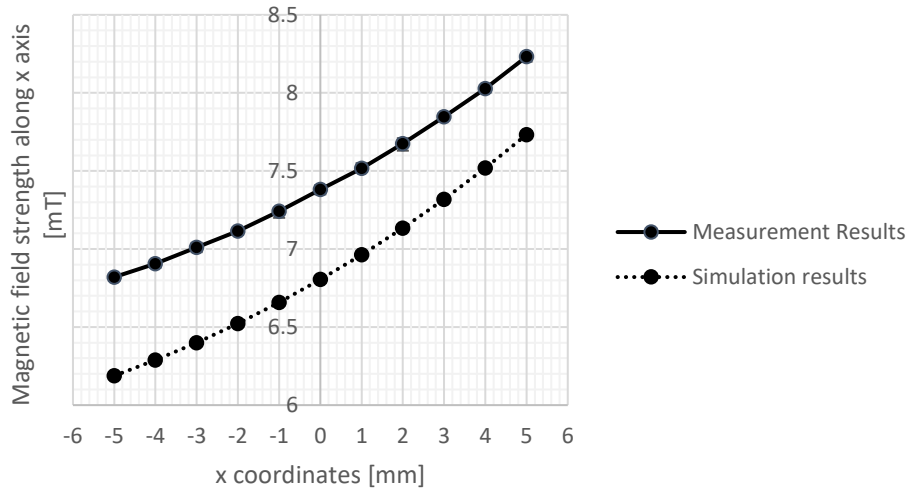


Figure 3.30 Comparison of measurement and simulation results of asymmetry configuration $\epsilon = 30 \text{ mm}$

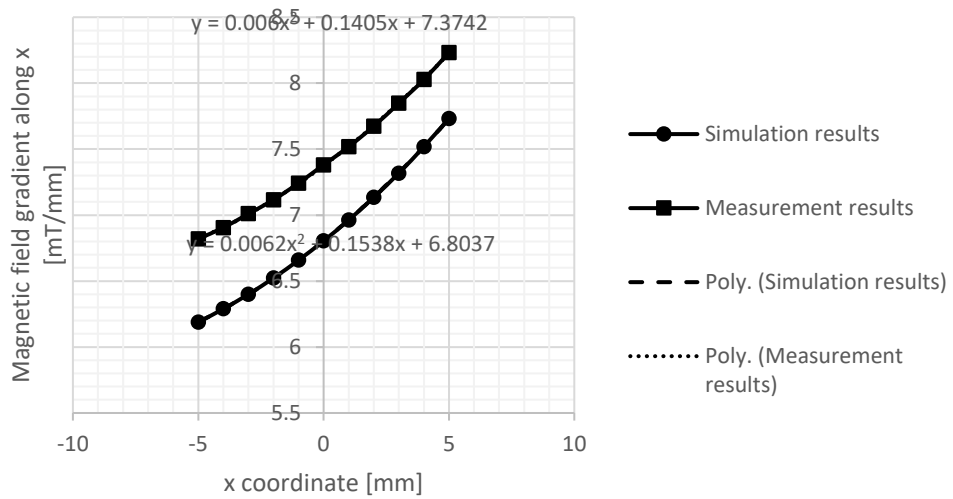


Figure 3.31 Magnetic field gradient comparison of asymmetry configuration $\varepsilon = 30\text{mm}$

3.6.1.1 Results and Discussion on EMA Calibration

Between the simulation model and the constructed model, the graphs and values measured along the x axis demonstrated a significant correlation. Furthermore, the estimated ratios indicate that the difference is less than 10%. Current differences, non-ideal created models, measurement offset formed with gaussmeter over time, or variances between real and simulation models could all contribute to the mismatch.

CHAPTER 4

THE MANIPULATOR SYSTEMS

4.1 Introduction

This chapter includes the design, manufacture and calibration processes of the manipulators that are purposed for microrobot actuation. The manipulator section is divided into two. Manipulator studies, the design and manufacturing phases of a few manipulator versions before reaching to the final forms constructs the first part, named 'previous studies and works'. The system manipulators (i.e., Euclidean platform parallel manipulator and subsidiary manipulator systems, 3 DOF each) composes the second part, giving more details with the fundamentals and kinematics. Then, the calibration processes were evaluated.

4.2 Robot manipulators

Parallel robots are popular and common for some advantages like high load capacity and high resolution, generally consisting of two platforms connected to each other via links or joints. First milestone stages starts with Gough (Gough, 1962) and Stewart (Stewart, 1965). Derived from these, Stewart platform is one of the most famous of its category as it is a fundamental design and its DOF is 6 where most of the motions can be satisfied (x, y, z, roll, pitch, and yaw motions). Also, Delta robot is one of the acknowledged parallel robots manifested in (Clavel, 1988) . Parallel robot structure synthesis was studied by many researchers ((Alizade & Bayram, 2004; Freudenstein & Alizade, 1975; Gogu, 2008; Merlet, 2006)). Euclidean platform parallel manipulators are the parallel manipulators that the platform motion depends on the dyads of Euclidean planes. These Euclidean platform manipulator synthesis was studied in (Alizade et al., 2008).

4.3 Previous Studies and Works

In this part, some other manipulator models that were studied/manufactured at a considerable amount and effort are given.

A proper relative position and orientation between microrobot and EMAs are required for the microrobot manipulation system. One of the objectives was to deduce the microrobot manipulation complexity to the mechanisms, as previously stated. Subsystem/sub mechanisms are then deduced from the mechanism. The microrobot environment is basically not grounded and has 3 DOF motion capability, depending on the suggested configuration. The EMA mechanisms are mounted on a platform with three degrees of freedom (referred to in this thesis as a parallel manipulator), giving it a total of six degrees of freedom.

The first studied models were originated from Stewart platform, shown in Figure 4.1. This parallel manipulator mechanism consists of 6 links. The actuators might be prismatic or rotary in different variations and actuator types.

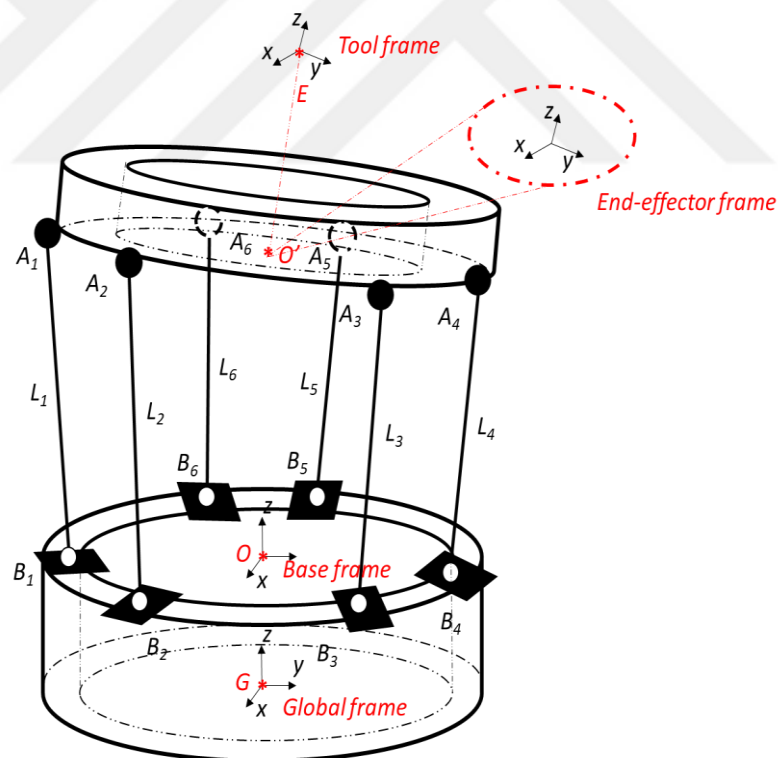


Figure 4.1 A general Stewart platform

The considered system for this work was inspired from a model where the base joints are sliding independently while the link lengths are not altering. In (Bonev et al.,

2006), an inspired work is given that also mentions about the extra ability for infinite rotation around z axis (yaw motion) if cable length constraints are eliminated or ignored, which is given in Figure 4.2. The base joints can move on a circular path individually controlled by the electric motors with encoders. Of course, the assumption is that the platform carries the EMAs, and the centre part of the platform is left as a hollow for microrobot environment.



Figure 4.2 Microlar Rotopod R-3000 (Bonev et al., 2006)

At the first steps of the full model development, using the trial-and-error method for dimension decision and unconventional model parts, the designed model is given in Figure 4.3. The model also includes a ROI area and a visualization system with a camera and a digital microscope, in which the microrobot environment is fully grounded and the parallel manipulator provides all the DOFs. In a simple term, the development of this system was halted due to manufacturing difficulties. Furthermore, the noncoincidence of the coaxial axis of the EMAs and the plane comprised of spherical joints on the platform limited the motion capabilities of the EMAs.



Figure 4.3 Stewart-like studied manipulator system

The parallel manipulator, as can be seen, has all of the degrees of freedom required for proper microrobot actuation. The next design was simplified by dividing the degrees of freedom, resulting in a secondary manipulator system that holds the microrobot environment. After dividing the system into sub manipulators, it is critical to be able to see the system as a whole and meet the needs.

The first step with the system implementation was to assign one of the most difficult motions to the new manipulator: rotation around the z axis. The remaining motions were then logically deduced between the manipulators. The rotation motion around z axis was moved to the manipulator called subsidiary manipulator system. Then, based on reviews of existing manipulator systems in the literature, it was decided to transfer translation motion to the xy plane, which could still cause serious issues with the parallel manipulator. As a result, two manipulators were acquired at the conclusion of the evaluations, one called parallel and the other a subsidiary manipulator system. The first subsidiary manipulator system design having a PPR (prismatic-prismatic-rotary) serial chain is given in Figure 4.4, holding the microrobot environment at the top part while a bottom camera with a lens is appointed to observe it from under.

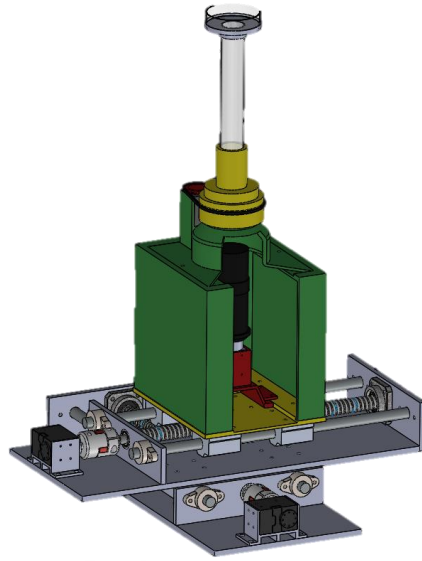


Figure 4.4 First subsidiary system design

Rotation around x and y axes, as well as translation along the z axis, should be provided after motions have been deduced. The new parallel manipulator system was created with a Euclidean platform structure to reduce complexity. Because the leg joints/links are all on the same Euclidean plane, the coordinate relationship can be analysed using 2D analytics rather than 3D.

Additionally, the parallel manipulator's layout direction was reversed. The skeleton of the parallel manipulator was made of aluminium sigma profiles, and the new model was purposefully designed with easy-to-manufacture parts. The number of legs connected to the platform has been reduced to three, leaving an idle joint between the rotary actuator and the platform joint, which is ideal for academic study. From the ground to the platform, each leg has a chain of Rotary-Rotary-Spherical (RRS) joints. Also, this system (with minor/major changes) was studied in (Akçura et al., 2019) with kinematic and dynamic calculations. This was a prior work to find out the system requirements, especially the motor specifications.

The electromagnets' linear motion mechanisms were changed from threaded motion parts to screw rod, which is commonly used in 3D printers. Two guider rods were chosen as carbon rods to make the system lighter. The electromagnets' focus point is

the platform frame's volumetric centre, allowing it to easily assemble the spherical joints and front camera. The system is given in Figure 4.5. This model was built, studied, and then abandoned because the mechanical structure (in terms of material robustness) and motor performance were insufficient to produce precise results and had poor motion control in practice.

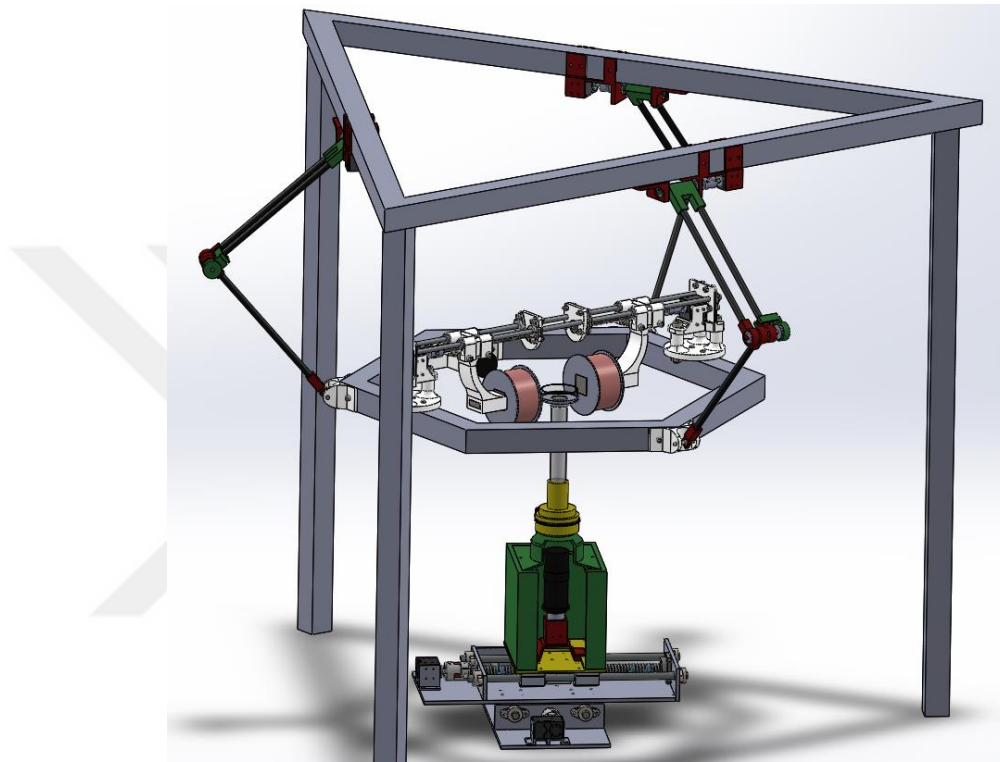


Figure 4.5 First Euclidean platform parallel manipulator accompanied with subsidiary manipulator system

4.4 Analysis, Design, and Manufacturing of Manipulator Systems

The system consists of two manipulator systems: an Euclidean platform parallel manipulator system and a subsidiary manipulator system, as described in the previous studies and works section. The systems are given in Figure 4.6. Also, another sub mechanism, i.e., EMA linear motion mechanism, was evaluated.

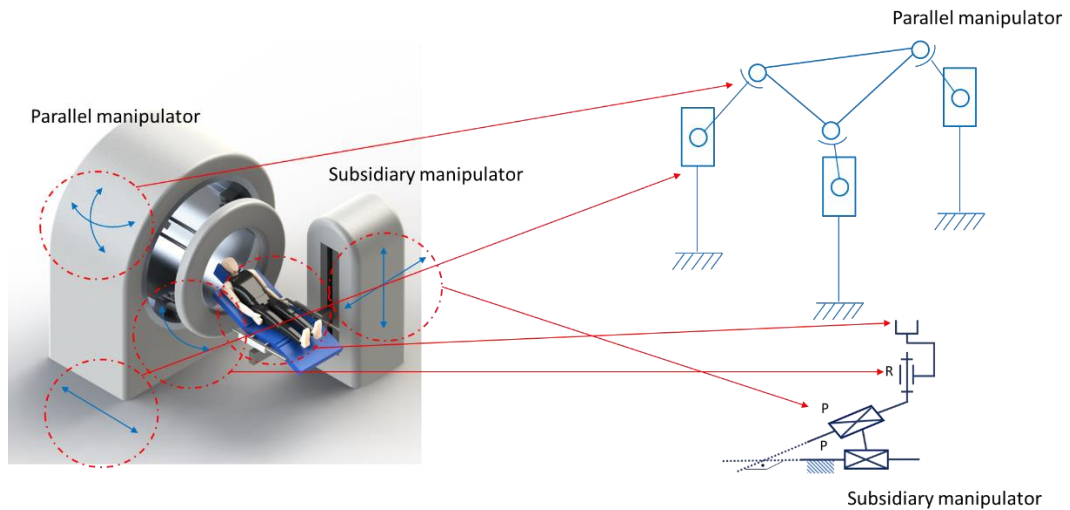


Figure 4.6 The prototype system showed with the motion adaptations

4.4.1 *Euclidean Platform Parallel Manipulation System*

Mentioning the previous subsection, the parallel manipulator structure was undergone major changes with the manipulator structure. PRS (Prismatic-Rotary-Spherical) leg chain was found to be suitable for the purpose after some research. Instead of hanging legs from the ceiling, the chains start at the bottom and the weight of the platform is supported by the leg mechanisms. Another issue that existed previously has been solved by the prismatic joint design preference, in which the legs act as a brake mechanism in the occurrence of a motor failure. The new design is shown in Figure 4.7. As can be seen, this is also a Euclidean platform parallel manipulator that generates three Euclidean plane edges, which are indicated by transparent shape. The related Euclidean model is given in Figure 4.8.

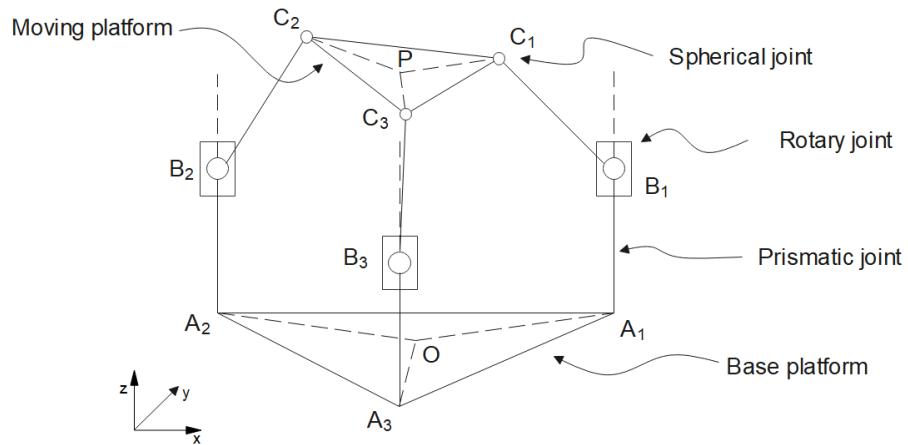


Figure 4.7 Parallel manipulator system

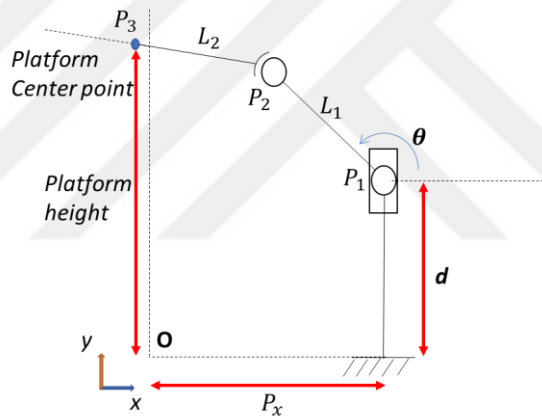


Figure 4.8 Inverse kinematic of one leg on an Euclidean plane

In Figure 4.7, the reference of the mechanism is assumed point O , having the coordinates $(0, 0, 0)$. The plane consisting of O , A_1 , B_1 and C_1 points construct one of the Euclidean planes. Likewise, the other two planes are constructed using O point and its related number. For one leg, while $|A_1B_1|$ forms the prismatic joint, the rotary joint takes place at B_1 and spherical joint at C_1 connecting to the moving platform. The unshown parameters $|OA_1|$ presents the base platform radius as $|PC_1|$ imposes moving platform radius.

The kinematics of the parallel manipulator can be defined using homogenous transform matrices that consists of rotation and translation data. The general form is shown in Equation 4.1 which represents the coordinates of point i with respect to $i-1$.

$${}^{i-1}T_i = \begin{bmatrix} {}^{i-1}R_i & {}^{i-1}p_i \\ 0 & 1 \end{bmatrix}_{4 \times 4} \quad (4.1)$$

The forward kinematics can be obtained creating a closed chain equilibrium. Series transformations multiplied consecutively results the direct transform of last point with respect to first point. Equation 4.2 and 4.3 shows the forward and inverse kinematic formulas for the manipulator system.

$${}^0T_P = {}^0T_{A_1} {}^{A_1}T_{B_1} {}^{B_1}T_{C_1} {}^{C_1}T_P \quad (4.2)$$

$${}^0T_P ({}^{C_1}T_P)^{-1} = {}^0T_{A_1} {}^{A_1}T_{B_1} {}^{B_1}T_{C_1} \quad (4.3)$$

If each matrix form is expanded, each of them can be written as in Equation 4.4, 4.5, 4.6 and 4.7.

$${}^0T_{A_1} = \begin{bmatrix} c\alpha & -s\alpha & 0 & P_x \\ s\alpha & c\alpha & 0 & 0 \\ 0 & 0 & 1 & 0 \\ 0 & 0 & 0 & 1 \end{bmatrix}, \quad \alpha = (i-1)\frac{2\pi}{3} \quad (4.4)$$

$${}^{A_1}T_{B_1} = \begin{bmatrix} 1 & 0 & 0 & 0 \\ 0 & 1 & 0 & 0 \\ 0 & 0 & 1 & d \\ 0 & 0 & 0 & 1 \end{bmatrix} \quad (4.5)$$

$${}^{B_1}T_{C_1} = \begin{bmatrix} c\theta & 0 & s\theta & L_1 \\ 0 & 1 & 0 & 0 \\ -s\theta & 0 & c\theta & 0 \\ 0 & 0 & 0 & 1 \end{bmatrix} \quad (4.6)$$

$${}^P T_{C_1} = \begin{bmatrix} {}^o R_P R_z(\alpha) & L_2 \\ 0 & 0 \\ 0 & 0 \\ 0 & 1 \end{bmatrix} \quad (4.7)$$

Calculations with these matrices takes time and effort. Transforming the points from spatial to Euclidean plane, the projection equation of a point is given in Equation 4.8-4.9 where α is the related plane angle.

$$P_{x,2D} = \sqrt{P_{x,3D}^2 + P_{y,3D}^2} \quad (4.8)$$

$$P_{y,2D} = \sqrt{P_{x,3D}^2 + P_{y,3D}^2 + P_{z,3D}^2} \quad (4.9)$$

The inverse kinematic equations, the position is already known for P_2 since the position and orientation of platform centre of P_3 is known. The rest of the inverse kinematic analysis for a leg mechanism is given in Equation 4.10-4.13. As known, forward kinematic calculation is very difficult and not needed for the thesis.

$$P_x + L_1 \cos \theta = P_{2,x} \quad (4.10)$$

$$d + L_1 \sin \theta = P_{2,y} \quad (4.11)$$

$$\theta = \cos^{-1} \left(\frac{P_{2,x} - P_x}{L_1} \right), \quad 90 < \theta < 270 \quad (4.12)$$

$$d = P_{2,y} - L_1 \sin \theta \quad (4.13)$$

During these motions, it should be considered that when a rotation occurs, on account of the motion constraint of the platform legs, the position of the platform centre slides on xy axis, shown in Figure 4.9. To provide the appropriate analytical solution, the platform centre should be shifted to a position that satisfies the leg positions. This shifting motion can be later compensated with subsidiary manipulator.

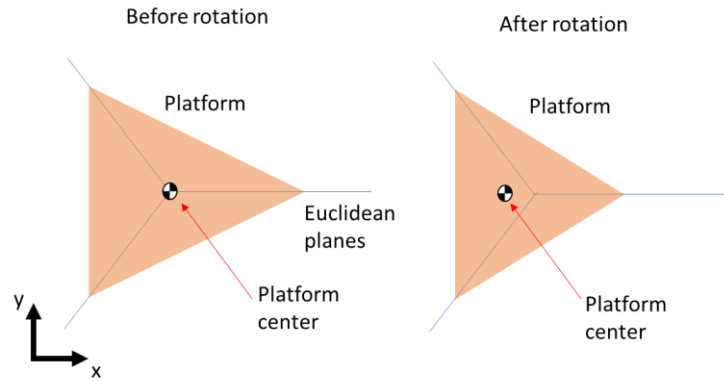


Figure 4.9 Platform rotation and platform centre point relationship

With the DOF analysis, it can be seen that a lot of formulations were studied, some of them can cover most of the basic mechanisms without considering specialized special occasions. Even if this system is a basic system, it was also verified referencing to (Tsai et al., 2003) where the formulation of Freudenstein and Maki (Freudenstein, 1959), given in Equation 4.14.

$$F = \lambda(l - j - 1) + \sum_{i=1}^j f_i \quad (4.14)$$

Here, F stands for degrees of freedom, λ for degrees of freedom that the manipulator operation, l for number of links, j for number of joints, and f_i for number of degrees of freedom that the joint has. So, λ equals to 6 since the manipulator exist in spatial, l to 8 for 2 links for each leg and 2 platforms, j to 9, and f_i to 1 for prismatic and rotary joints and 3 for spherical joints. Then, the equation equals to 3.

The platform design consists of a cage structure made of hexagonal sigma profile for robustness. The linear mechanisms were leaned against three columns out of six between bottom and top frames. The cage structure can be seen in Figure 4.10.

One of the major problems with the design was to provide sufficient angle capability between L_1 and L_2 links given in in Figure 4.8. The issue raised as more capable joints had tremendous dimensions and weights comparing to the rest of the

system. Thus, custom designs and improvised solutions with a few types of spherical joints were tested. In Figure 4.10, the final model of parallel manipulator with spherical joint structure can be observed. Therefore, the manufactured subsidiary manipulator height was referenced with the microrobot position. Predicating on a spherical joint with a 25° angle, a custom designed angled mounting parts provided 0° angle when the platform is at the same level with the microrobot environment. Depending on the analyses, the system can perform up to 21° of rotations using the maximum rotation of spherical joints. It was preferred to use up to 18° of motion with safety limits. This structure can be observed in Figure 4.11.

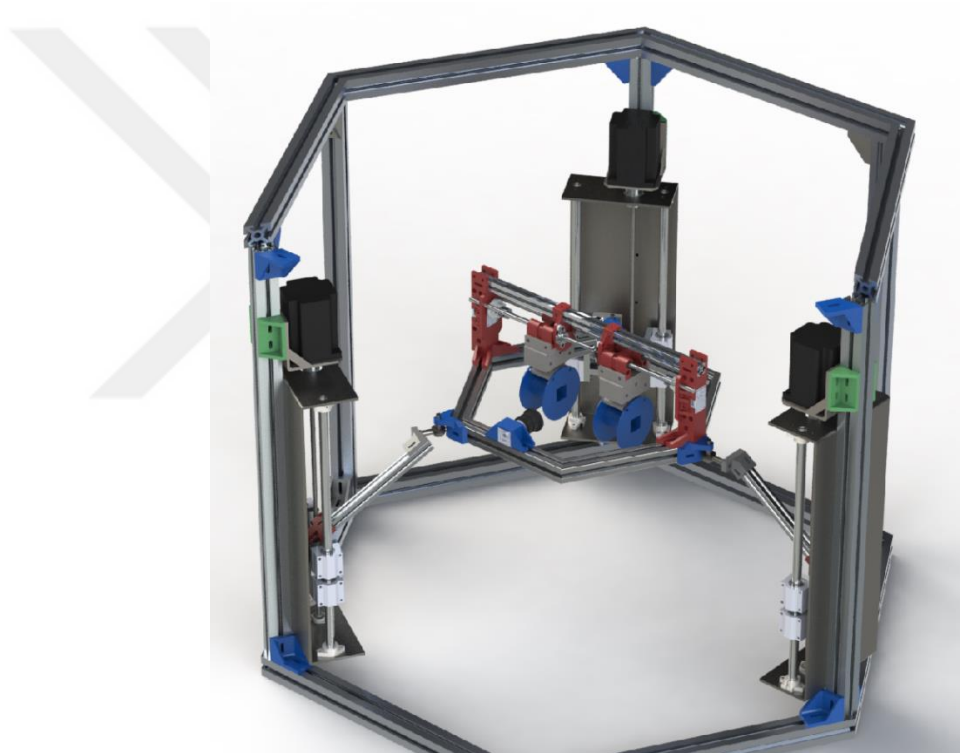


Figure 4.10 The final design of Euclidean platform parallel manipulator with hidden beams

The manufactured leg and guide mechanism are given in Figure 4.11 supporting the structure shown in Figure 4.10. Also noticed, legs with a sigma profile instead of carbon tubes were preferred for better supporting the joint system. Smart servo motors were replaced with stepper motors with more power, and a linear screw shaft and two guiding shafts provide translation motion.



Figure 4.11 Design improvement with major structure reinforcement revisions with leg and spherical joint structure

Depending on the design and manufactured model dimensions, the cage radius is 1200 mm, cage height is 880 mm, 300 mm of L_1 length, 270 mm of L_2 length and 504 mm of P_x distance.

Using these structure parameters, the dynamic calculations can provide the necessary power for motor selection. The model for the calculations is given in Figure 4.12. L_1 and L_2 links were simplified as homogenous rods.

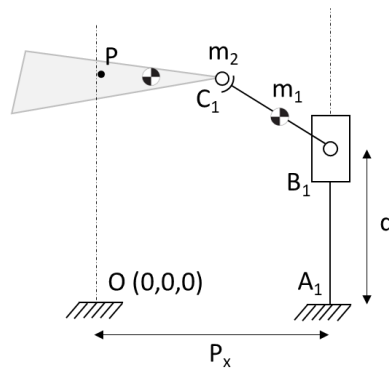


Figure 4.12 Simplified 1/3 model of the parallel manipulator for dynamic calculations

The conventional dynamic calculations consist of kinetic and potential energies. The related formulas are given in Equation 4.15-4.18.

$$U = m_1gh_1 + m_2gh_2 \quad (4.15)$$

$$T = \left(\frac{1}{2}m_1V_1^2 + \frac{1}{2}J_1\omega_1^2\right) + \left(\frac{1}{2}m_2V_2^2 + \frac{1}{2}J_2\omega_2^2\right) \quad (4.16)$$

$$E = U + T \quad (4.17)$$

$$P = \frac{dE}{dt} \quad (4.18)$$

The dynamics were tested using extreme motion conditions. This motion consists of 10 mm of translation and -15° to $+15^\circ$ rotation motion at the same time and in totally 1 second. The calculations were handled numerically, all the position and velocity data were obtained with intervals using inverse kinematic calculations. The result shows 3 W power was needed for the motion. Thus, 13.85 W stepper motor was picked for the system.

4.4.2 Subsidiary Manipulation System

Referencing to the previous design and works section, the subsidiary manipulator underwent a major change. Unlike the previous mechanism that worked on the router principle, the translation mechanism was built in the T-bot style because the considerations were changed. Alternative two-dimensional cartesian mechanisms were investigated during the research phase. H-bots, which are widely used in 3D printers, are one of the most popular structures. Also another structure, called CoreXY, is similar to it. The figures of mentioned structures are given in Figure 4.13. These motion mechanisms have advantages and disadvantages. The biggest disadvantage is that using a timing belt as a driving element makes the system more complex, and the system becomes parallel instead of series, with each cartesian coordinate of the cart bound to both motors in the system. The most significant benefit of these systems is that they allow the cart to carry less weight because all the motors are grounded. The

T-bot structure was chosen for this project because the payload shape desired on the cart was essentially in the shape of a tower and appeared to be more compact than the others.

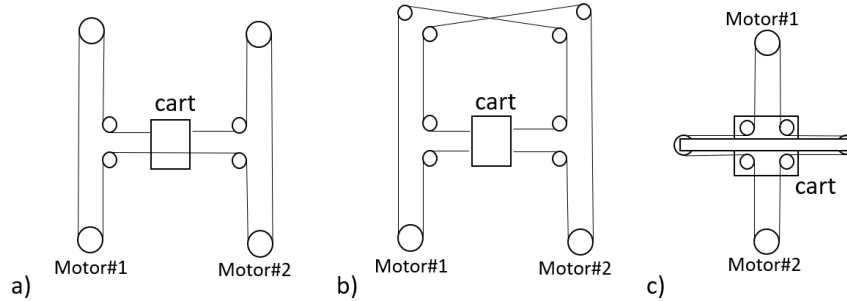


Figure 4.13 xy cartesian structures: a) H-bot b) CoreXY c) T-bot

The mechanism design is given in Figure 4.14. The part consisting of prismatic joints shown with P and the rotary part with R . Using the same DOF formulation (λ equals to 3, l to 4, j to 3, and f_i to 1 for prismatic and rotary joints), it can be calculated as 3. This makes a total of 6 DOF combining parallel platform and subsidiary manipulator.

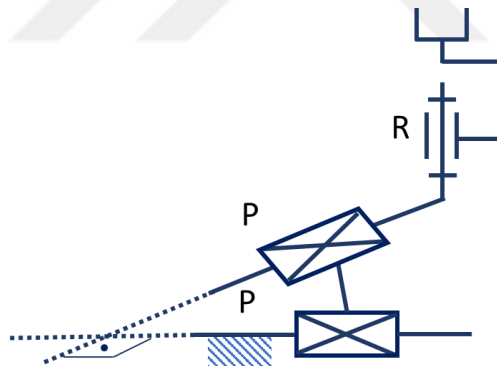


Figure 4.14 Subsidiary manipulator layout

Subsidiary manipulator has a simple structure that both forward and inverse kinematic calculations can be handled. Basically, for T-bot motion, if motors A and B have linear motions, they cause motion in x and y . Inverse calculations can be extracted in the same way. Motor relative motions result in relative changes in both coordinate axes. Equations 4.19 and 4.20 show the basic motion calculations for T-bot.

$$\Delta x = \frac{1}{2}(\Delta A + \Delta B) \quad (4.19)$$

$$\Delta y = \frac{1}{2}(\Delta A - \Delta B) \quad (4.20)$$

A custom design was created to meet the requirements for rotational motion in the z axis. A rotational motion should be achieved in this system, while a camera system should be used to observe the working area from the bottom. The manufactured hybrid system is given in Figure 4.15. The T-bot system can be classified as a parallel robot, and the chain continues with a series joint, making the entire manipulator a hybrid manipulator. The motors for this manipulator are Dynamixel XL-430-W250-T smart servo motors, which are used for both xy plane motions and rotation around the z axis.



Figure 4.15 Manufactured subsidiary manipulator system

The parts' dimensions allow for a maximum of 150 mm of x and y axis translation, and the microrobot is positioned 500 mm above the ground. These dimensions were chosen based on the system's requirements and compactness.

4.4.3 EMA Linear Mechanism

EMA mechanism underwent some changes as well. A sigma profile from one side to the other was preferred to provide better support for EMAs. The first manufactured linear electromagnet mechanism is given in Figure 4.16, and the last form design is given in Figure 4.17. The mechanisms are actuated using Dynamixel XM430-W350-R smart servo motors. Each EMA linear motion is transferred using linear screw. The linear motion distance of each EMA is directly correlated with the screw pitch and number of motor turns.

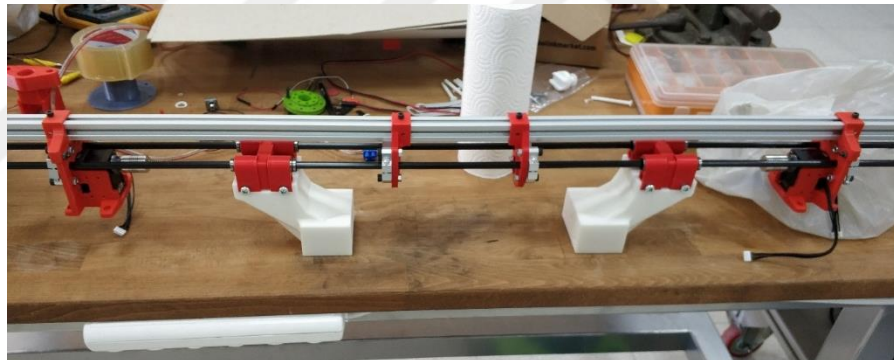


Figure 4.16 Electromagnet linear mechanism

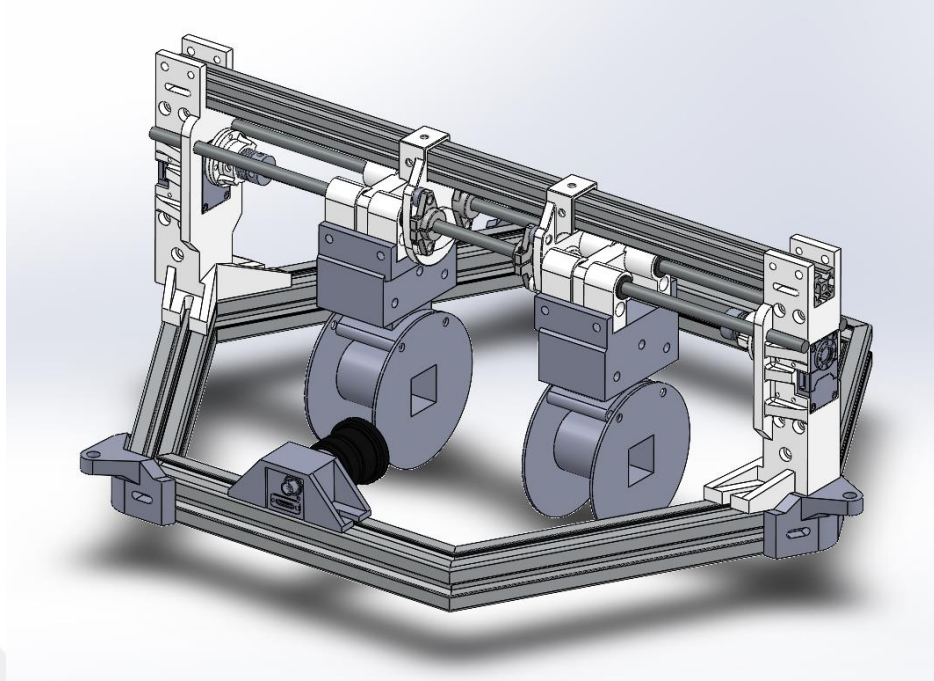


Figure 4.17 The last form of the platform and electromagnet mechanism layout

Depending on the design and manufactured model dimensions, the platform radius is 270 mm and the top side of the supporting beam has a height of 170 mm from the centre point. Moreover, after attaching the EMAs, since core lengths are relatively longer, each EMA has 40 mm of motion capabilities referencing to 100 mm homogenous magnetic field configuration.

4.5 Mechanical System Calibrations

Hybrid mechanical system components and subsystems require scientific-prooved calibration and verification for the process. During some of these processes, Keyence LK-G152 laser distance sensor head was used for linear measurements and Optitrack camera system was used for position and orientation measurement of parallel platform system.

For subsidiary manipulator, the sensor head was assembled to the system as in Figure 4.18. The relative translation motion values that are acquired by the sensor system and motion command log are evaluated to determine the performance of the mechanical system.

Before the whole calibration process, the calibration limits should be revealed. Before, the basics of microrobot manipulation was studied using KUKA KR 6 R900 sixx robot. This series robot manipulator is the comparison reference for this new system. The most convenient comparison parameter that is provided in the catalogue by KUKA robot manufacturer is repeatability, which is 0.03 mm. In terms of involving two manipulators, the repeatability of KUKA robot is compared with the sum of repeatability values of parallel and subsidiary manipulator systems with translational motions.

If the comparison situation is fully analysed, also the opposing states should be revealed. KUKA robot is a more complex manipulator system with high quality elements and more sensors which are positioned at the joints. Moreover, the software support should not be ignored. In the parallel manipulator system, there is no position/angle sensor but microcontroller software counters, and only motor encoders exist with subsidiary manipulator systems. It is not known that how much the mechanical elements like joints, timing belts, and motor backlash causing error. Besides, KUKA catalogue data is not transparent that how much data was used. Further, KUKA robot tests might be accomplished under full load, but it is not possible to provide the same situation with the measurement equipment and manipulator environment.

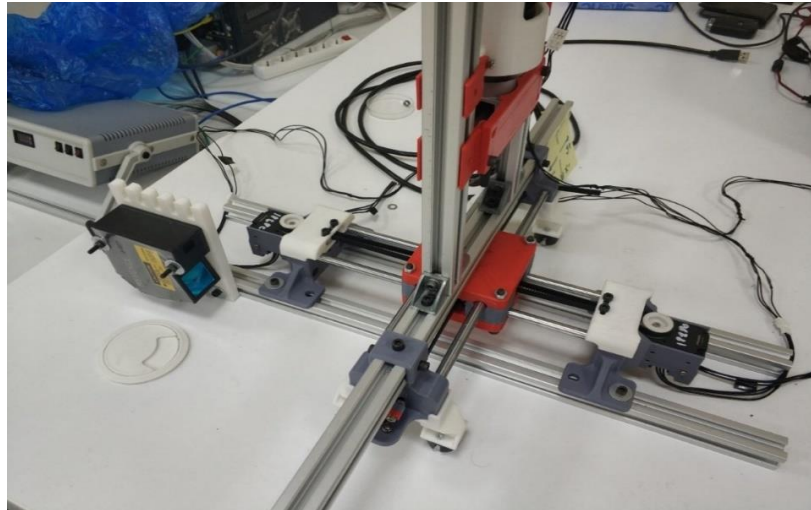


Figure 4.18 Measurement sensor assembly for subsidiary mechanism

Pure motion in the x axis was studied in the first applications. The number of teeth on the timing belt pulley directly aids in defining the translation, while both servo motor encoders provide feedback for precise control. The feedbacked relative distance values had some error with the commanded distance values in early tests. It was also discovered that there was a backlash error with the motion. Additionally, different smart servo motor controller parameters resulted different error values. Using trial-and-error method, the backlash was compensated with software compensation (coding). Table 4.1 shows the compensated motion results, which include two motion scenarios. The first scenario involves motion sequences with commands involving relative distance differences of 10 mm in random directions. The high precision laser distance sensor was used to measure and determine the final positions. The results include the compensated backlash motion.

Table 4.1 Subsidiary manipulator system calibration of 10 mm steps

Command sequence	Relative position change [mm]
0	-
1	10.01
2	10.06
3	10.05
4	9.93
5	10.1

Table 4.1 Continues

6	9.92
7	10.02
8	10.01
RMS error [mm]	0.0988
Standard deviation [mm]	0.0618
Average [mm]	10.013

The electromagnet mechanism calibration system is given in Figure 4.19. Using an augmented plate attached to the electromagnet coil adaptor, the Keyence laser distance measurement system calculates the relative distance. The motion commands and relative error table is given in Table 4.2.

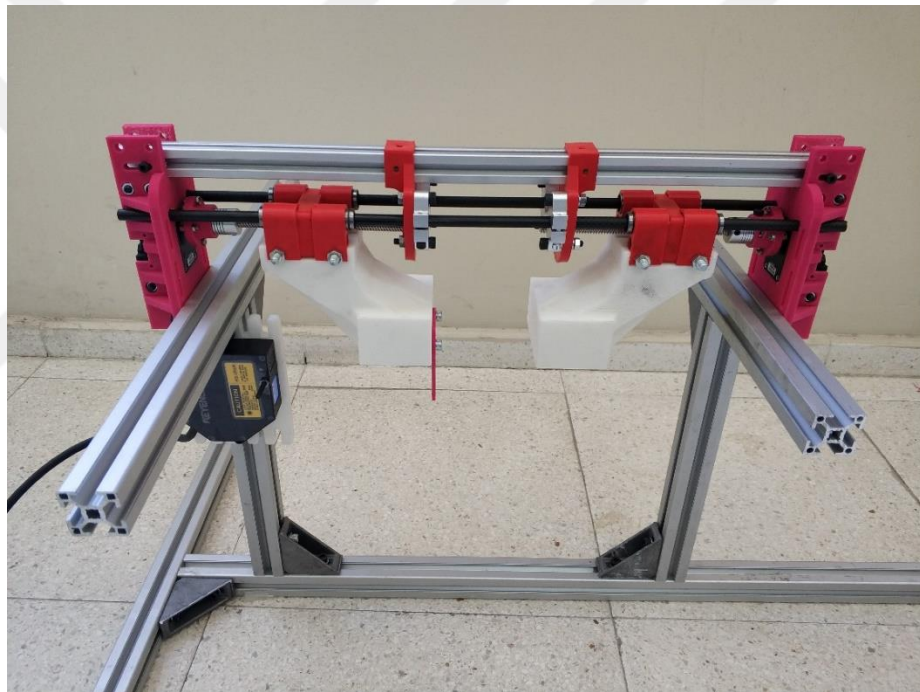


Figure 4.19 Electromagnet mechanism calibration

Table 4.2 Electromagnet linear mechanism calibration results

Left electromagnet		
Relative command [mm]	Relative measurement [mm]	Error [mm]
0	-41.48	-
-2	-39.52	-0.04
0	-41.48	-0.04
-4	-37.53	-0.05

Table 4.2 Continues

-2	-39.49	-0.04
-6	-35.55	-0.06
0	-41.49	-0.06
-6	-35.55	-0.06
-8	-33.57	-0.02
-10	-31.64	-0.07
-12	-29.61	0.03
0	-41.49	-0.12
RMS error [mm]		0.059
Standard deviation [mm]		0.036

To verify the parallel robot system, the camera calibration method was used. This step was completed with the help of a high-precision Optitrack camera system. There must be at least two cameras, each of which must be calibrated before being used. For the measurement, at least three probe balls are required, and in our method, these balls form a rigid body in the platform's centre. Figure 4.20 shows the calibrating system. The measurements were taken from the rigid body centre, which was formed by the marker balls positioned at the centre point of the platform. Also, it should be informed that the figure includes blue coloured masking band to prevent surface that interrupts camera tracking. Moreover, the structure includes some of the hanging leg mechanisms which were left from the previous studies, irrelative with the current project progress but they were unable to get removed for administrative issues. Figure 4.21 shows the user interface of the application that displays the measurand.

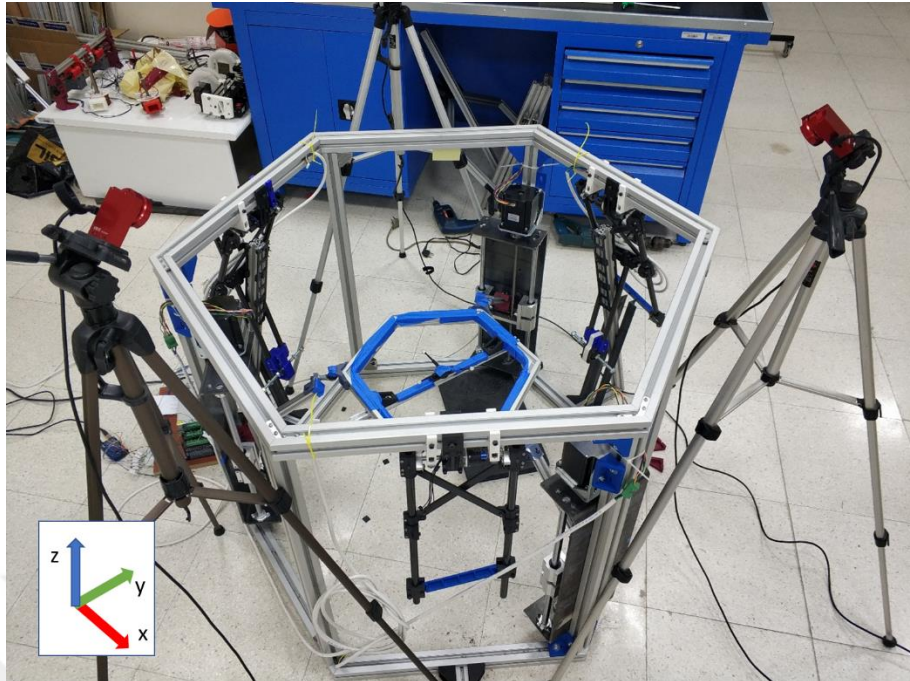


Figure 4.20 Parallel robot calibration system where three cameras observe the measurement probes

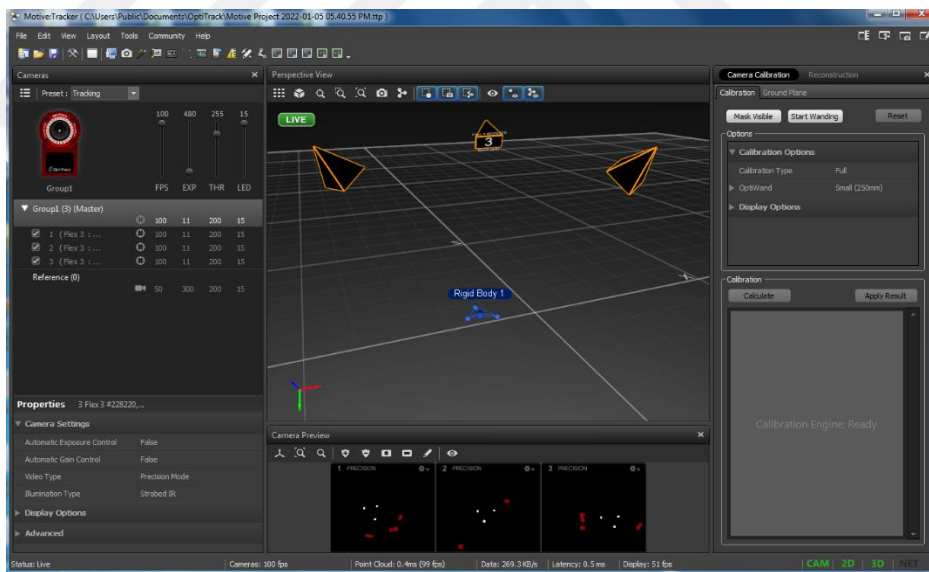


Figure 4.21 Marker and camera configurations shown in the user interface of the program

Translation motion, pitch motion, and roll motion were inspected in the calibration process of the parallel manipulator.

Table 4.3 shows the consequent motion orders as well as the measured data. In z axis, parallel platform relative zero point of the was assumed as 500 mm from ground.

Table 4.3 Translation motion of the platform

Relative command in z axis [mm]	Relative measured position in z axis [mm]	Absolute error [mm]
0	0	0
-5	-4.85	0.15
-9	-8.83	0.17
-15	-14.78	0.22
1	1.09	0.09
5	5.06	0.06
9	9.05	0.05
-1	-0.85	0.15
RMS error [mm]		0.1306
Standard deviation [mm]		0.0623

Parallel manipulator pitch motion serves as the primary motion for the entire system. Table 4.4 lists the motion commands as well as the measured data. Figure 4.18 shows the relevant motion graph. It should be noted that, following the calculations and analyses for spherical joint motion simulations, a limit angular motion of 18° was applied with sufficient safety margins for both pitch and roll motions. For all rotating directions, measurements are provided. It should be noted that the negative side is intended to be used primarily (e.g., if the microrobot is intended to provide motion in the +z direction, the platform executes the rotation in the negative side, and microrobot motion in the -z direction may be provided using gravitational force and thus be used less). Because the leg configuration is asymmetric and most of the weight is applied to only one leg, the measurement findings are asymmetric, resulting in a bit greater error with higher rotational angles.

Table 4.4 Pitch motion of the platform

Relative command in pitch angle [degree]	Measured relative angle [degree]	Error [degree]	Relative command in pitch angle [degree]	Measured relative angle [degree]	Error [degree]
0	0	0	0	0	0
3	2.95	-0.05	-3	-2.95	0.05
6	5.93	-0.07	-6	-5.88	0.12
9	8.97	-0.03	-9	-8.9	0.1
12	12.13	0.13	-12	-11.91	0.09

Table 4.4 Continues

15	15.61	0.61	-15	-14.89	0.11
18	19.29	1.29	-18	-17.85	0.15
0	0.12	0.12	0	-0.01	-0.01
RMS error [deg]		0.509	RMS error [deg]		0.093
Standard deviation [deg]		0.474	Standard deviation [deg]		0.057

Table 4.5 shows the motion commands as well as the measured data. The measurements were taken in only one direction because the movements and leg structures are symmetrical. It should be informed that due to the symmetry of the EMA positionings on the platform, roll motion is not actively used.

Table 4.5 Roll motion of the platform

Relative command in roll angle [degree]	Measured relative angle [degree]	Error [degree]
0	0	0
3	2.91	-0.09
6	5.82	-0.18
9	8.81	-0.19
12	11.8	-0.2
15	14.91	-0.09
18	18.3	0.3
0	0.02	0.02
RMS error [deg]		0.163
Standard deviation [deg]		0.165

4.5.1 Conclusion of Mechanical System Calibrations

The mechanism calibrations using high precision measurement equipment were handled and some critical numerical variables were calculated. KUKA series manipulator, comparison reference manipulator, catalogue values showed that repeatability parameter can be used for comparison of these systems. Considering the worst-case scenario, the comparison value is obtained by summing the repeatability values of parallel and subsidiary manipulator systems. In any condition, the concerns about the comparison were explained.

In the catalogue of KUKA robot, the repeatability value is given as 0.03 mm. Besides repeatability, i.e., the standard deviation, of the parallel manipulator was calculated as 0.0623 and subsidiary manipulator as 0.0618 mm (for two axes it can be square rooted as 0.0873 mm), making total of 0.1072 mm considering vectoral approach in spatial.

As mentioned, the roll rotation is a redundant motion for microrobot manipulation. The results show that due to the asymmetry of the platform leg positions, with the positive angles especially exceeding 12° , the structure cannot provide enough constraint. However, the system can provide flexible control, and majorly the negative sided rotations can be utilized for a functioning system while limiting the positive sided rotations are limited to a lower limit.

CHAPTER 5

SOFTWARE ARCHITECTURE AND IMPLEMENTATION

5.1 Introduction

This chapter includes the software operation principles and structures including the software related components and their interactions. The whole operation is run on a computer with Ubuntu operating system. The main structure is organized around Robot Operating System (ROS). A Guided User Interface (GUI) is used to control and run the main operations, also interacting with the many nodes with different purposes. Hardware related operations include machine vision with two cameras, five Dynamixel smart servo motor control and Arduino supported three stepper motors.

5.2 Choosing the Operating System and Its Distribution

Choosing the operating system and its distribution plays a vital role especially considering the hardware compatibilities. So, here the considerations roughly include the intended software, libraries, and hardware.

ROS is designed to run only on Unix-based operating systems, and it remains so today. Ubuntu is the most widely used operating system for this, but it can also be run on Linux-based distributions such as Fedora, Gentoo, and Arch Linux, to name a few. It can also be found on other Unix-based operating systems, such as FreeBSD, but Ubuntu is the best operating system for running ROS.

The terms "Latest" and "LTS" refer to the most recent ROS distributions (Long Term Support). One can choose their preferred version while keeping in mind the OS version that has been specified as a prerequisite. Additionally, it is recommended to check for package support, as some packages may not have been compiled for the most recent version of the operating system.

It is possible to follow the most up-to-date installation and environment setup steps by following the tutorials provided on the official website of ROS.

According to the project's timeline, the most recent ROS distribution is known as Melodic, and it can be installed on at least the Ubuntu 16.04 operating system distribution. Dynamixel motor packages play an important role in the desired packages, and they also include support for ROS Melodic. Ubuntu 16.04 was chosen as the operating system and ROS Melodic as the ROS distribution as the foundation for the project.

5.3 Robot Operating System

In robotics, ROS is a collection of libraries that can be used to interface with a wide range of robotic platforms and application environments. It is particularly beneficial in applications where hardware implementation is required. Stanford Artificial Intelligence Laboratory developed it in 2007, and the Open-Source Robotics Foundation (OSRF) has been in charge of its administration and development since 2013. It's free and open source.

ROS can be examined from two perspectives: the OS (operating system) and the packages. On the operating system side, ROS provides some common operating system features such as file system and memory management, process management, scheduler, message passing between processes, low-level device control, package management, and so on. Packages provide the most commonly used functionalities, with a particular emphasis on navigation and planning as well as control and visualization. They also provide real-time capabilities as well as data logging and robotic applications.

While the general system is based on a number of ROS philosophies, these provide extensive development areas for applications for both newcomers and experienced veterans. First and foremost, it serves as a communication layer, reducing the amount of effort required to integrate communication between programs. The system is made up of a large number of small programs that are linked together and communicate with one another through messages. These programs are used as tools, which are generic programs that can be used for logging, plotting, and other types of visualization, among

other things. Coding can be done in a variety of languages, including C++, Python, Java, Java Script, MATLAB, and others. These program codes are capable of being executed in parallel. Aside from that, users have the ability to run their desired programs at any desired frequency, which makes controlling many robotics applications much simpler. Communications are administered by a "master" process that allows for the execution of different codes in a distributed fashion. Anyone, however, is free to create their own libraries and incorporate other ROS modules into their system.

5.3.1 Nomenclature

The following are some fundamental ROS concepts to consider:

- **Nodes:** Programs that can be executed and are primarily coded for a single purpose. These nodes can publish services and topics as well as subscribe to them.
- **Messages:** The data structures used in the transmission of information between nodes. Basically, the common structures like integer, float, Boolean, etc. are defined as messages, i.e. .msg files. Also, messages can consist of multiple messages.
- **Topics:** These are the names of stream messages, and they can contain any type of message that is specified. Topics are used by the nodes to transmit messages. When defining topics, also it should be mentioned two terms: publisher and subscriber. Meaning their names, publisher node publishes topic to the environment and subscriber node/nodes subscribe and read the topic data.
- **Services:** They are made up of nodes that serve as both service and client nodes. The client node requests a service from the node that is utilizing the service, and the service node responds with functionality such as computation results, triggers, and other features as needed.
- **ROS Master:** As an administrator, it provides all the information about communication required to conduct a proper peer-to-peer communication between nodes. Every node and services, topics, etc. registers to ROS master manages them.

- The parameter server: It is responsible for providing the variables that can be accessed over a network. It is contained within the ROS Master. This is particularly useful for configuring parameters in software.
- ROS Packages: These structures are file groups that contain nodes, messages, and services that are organized in a logical manner.
- Launch files: A tool for launching multiple nodes simultaneously. The structure is written as XML format.

A brief chart for ROS master, nodes and topic is given in Figure 5.1.

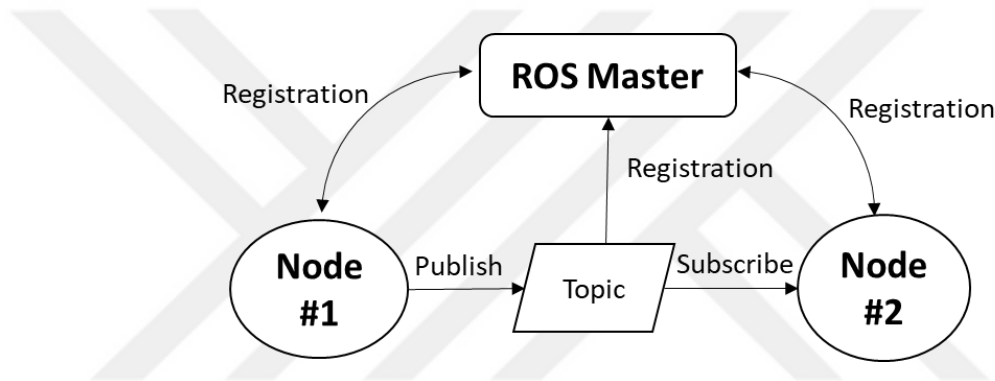


Figure 5.1 A general ROS communication schematic

5.3.2 Library Overview

Most of the packages are installed as add-ons to the base ROS installation, rather than as required. These packages are chosen in accordance with the requirements of the users. Also, it should be noted that the packages listed above are those that have been made available by the ROS community, developers, and related companies. Otherwise, in general, every user can create a package and publish it on the internet for use by other users who have access to the internet.

The following ROS packages were critically used:

- tf2 package: This package includes multiple coordinate system publications, transformation processes, and all the integration related elements (e.g., message, service, etc.) for integration with other packages.
- qt5 package: QT is a popular toolkit used for developing graphical user interfaces (GUIs). These interfaces basically include window and its elements like textboxes, buttons, etc. qt5 package interfaces the QT library to ROS environment. QT installation is required before package.
- dynamixel_workbench package: This package is provided by the producer of Dynamixel smart servo motors. It provides communication to the motors, giving capability of feedback and motion control.
- vision_opencv package: OpenCV is a very popular cross platform machine vision library which can provide real time computer vision capabilities. This package provides the interface to OpenCV libraries. So, an OpenCV library installation is also required before package.
- Rviz package: Basically, this package is used for visualization of 3D robotic environment. Even if it was not used in the latest program interface, in the development phase, it was used as a major support to tf2 package for visualizing the implementation of robot transform accuracies and the results.

5.4 OpenCV

OpenCV is an open-source software library especially used for computer vision. It can be used on any operating system and supports some popular and common languages like C++ and Python. This framework is supported by large companies for a long time and includes thousands of optimized algorithms for many machine vision problems. The applications include derives from reading/writing images and videos to object tracking using camera in real time.

In this project, OpenCV 4.3.0 release was used.

5.5 QT

A powerful generic tool for designing user interfaces, such as form applications, QT is available. The design tool is cross-platform, allowing you to program and integrate with a wide range of programming languages and frameworks. The tool includes all of the features you'll need to create complex, flexible applications, including a quick and accurate GUI layout, easy cut and paste, and mouse following, among other features.

QT is also supported by embedded features in ROS. Additionally, anyone can design their user interfaces (UI) using the QT Designer and then implement them into ROS using the QT binding features that have been implemented into ROS. In addition, their designs can be used as plugins for other websites. This way, anyone can simply drag the plugin form into their UI applications and place it wherever they want within them.

In this thesis, QT5 release was used.

5.6 Hardware

The hardware and their full-scale approach should be provided to facilitate software implementation.

5.6.1 Computer

The software implementation, particularly ROS, which has decentralized working capabilities using a Local Area Network (LAN) and multiple devices, was performed in a centralized manner, with all the nodes running on a single laptop. The computer was equipped with an Intel i7-8750 processor, 16 GB of RAM, and a GeForce 1050 graphics processor. Also, as peripheral PC hardware, two USB3.0 sockets for cameras and three USB2.0 sockets for U2D2 and Arduino hardware were also needed.

5.6.2 *Dynamixel Smart Servo Motors*

Servo motors and gear set components with a wide range of power, price, and size are available under the Dynamixel brand name, which is manufactured by Robotis Co. Ltd. Linux operating system and ROS environment are among the platforms and programming languages supported by the company's Software Development Kit (SDK), which includes source code and libraries that can be programmed using multiple platforms and languages. A variety of control modes are available, primarily including positional, velocity, and voltage controls for the motors. Several feedback variables from the motor (including instant encoder position reading, velocity, current, and so on) can be obtained during operation, and motion commands can be applied to the motor's internal PID control algorithms. The use of common communication protocols allows many motors to be connected to the same network (TTL, RS485, etc.). Industrial communication modules are built into some models on the inside. A converter apparatus can be used to connect a user's computer to the entire communication network.

Two Dynamixel XM430-W350-R motors and three Dynamixel XL430-W250-T motors were used in the finished version of the thesis. As opposed to translation motion in the xy plane and rotation around the z axis, which were provided by the XL430-W250-T motors, translation motion of EMAs were provided by the XM430-W350-R motors, which provide translation motion by changing the distance between. Each motor model number ends with a letter that denotes the communication type (e.g., R denotes RS485, T denotes TTL), which requires two different motor networks in practice. The expansion board OpenCM 485 allows for the creation of separate motor networks as well as shared power grids on a single board. The U2D2, USB to Dynamixel Interface hardware, was used since it is not possible to convert using only one hardware at the same time, but as previously stated, they can be connected to a shared expansion board to share resources. The fundamental structure is depicted in Figure 5.2. The connections between the motors can be established in a series communication manner due to the design of the sockets on the motors, as can be seen in the diagram.

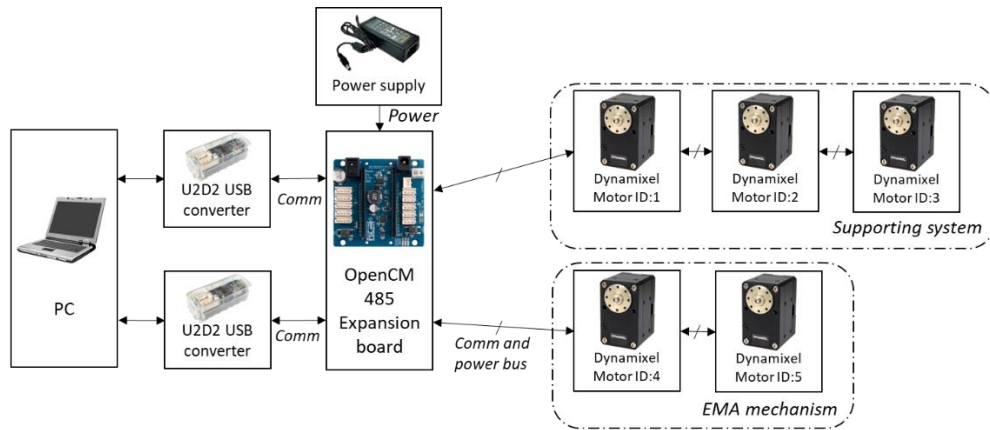


Figure 5.2 Dynamixel network schematic

5.6.3 Stepper Motor, Stepper Motor Drivers, and Arduino Mega board

Stepper motors have long been regarded as simple and inexpensive solutions for problems requiring precise trajectory and positioning. Stepper motors, in contrast to alternating current or direct current motors, require a driver to generate a proper rotation motion by energizing the proper windings in the proper order. Motors can be classified as either unipolar or bipolar depending on how the winding terminals were connected during the manufacturing process. This also has an impact on the cabling variation, with the number of leads varying between 4, 5, and 8.

Wave, full wave, half wave, and microstepping are some of the most commonly used driving methods. The methods essentially alter the energizing orders, durations, and amplitudes; the motor output is directly proportional to the methods' changes in position resolution, velocity, and power output. Even the names are limited in their ability to accommodate variations; the driving method is typically represented as a pulse/revolution parameter, the function of which can be deduced from the name. The motor drivers are also designed in a straightforward manner, depending on whether they are unipolar or bipolar in nature. Because the ready-to-use digital microstep drivers include their controllers and only require stepping (in the form of pulses), enabling, and direction commands, a wide range of variations are available to meet a variety of power demands. 4.5 Nm 4.2 A stepper motor and TB6600 4 A microstep driver were decided.

Arduino is a brand that encompasses the microcontroller hardware, software, and a large online community of users. A diverse range of microcontroller products is available, with capabilities and specifications changing over time. The programming language is straightforward and simple to learn, and the interfacing with motors and sensors is supported by a large number of libraries made available by the company and by members of the community. The programming and communication processes are simple and straightforward, making them user-friendly. They are built on the Atmel AVR architecture, which is part of the RISC family (which means that they have a smaller instruction set), but which also allows for faster and simpler computation operations. The Arduino Mega 2560 board was chosen because it provided a sufficient number of programmable pins, process specifications, and ROS integration.

The basic integration for the stepper motor configuration is given in Figure 5.3.

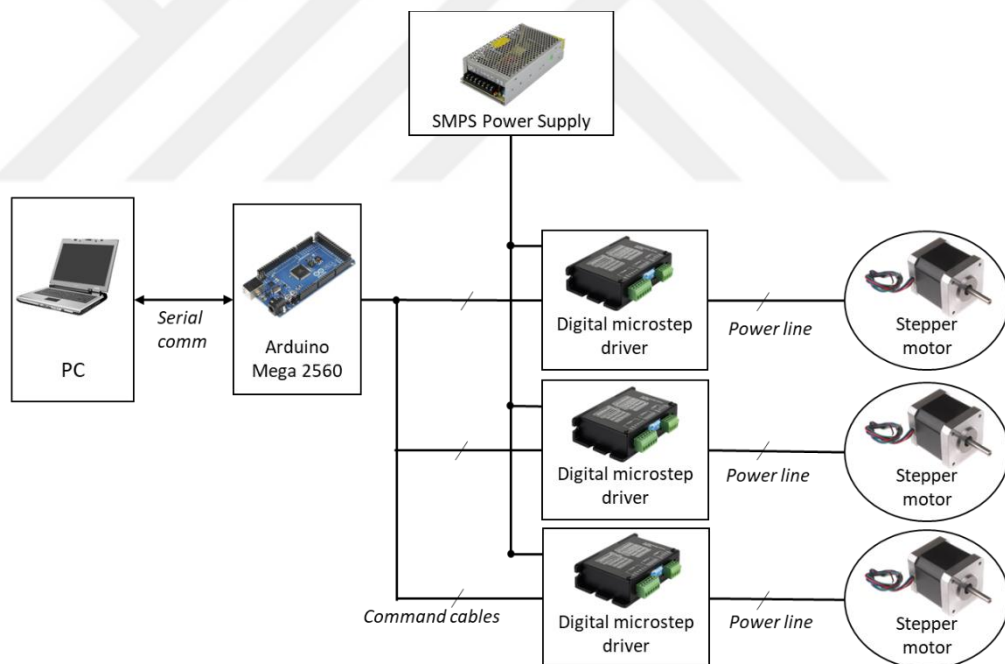


Figure 5.3 Stepper motor connection schematic

5.6.4 Basler Ace Camera

Basler is a company that develops and provides products and services in the field of digital vision. Basler's ace series includes models for low-cost, high-speed, small-diameter cameras with a USB 3.0 interface, among other things. Basler also provides a configuration program known as "pylon" as well as the ROS package, which is one of the primary factors in the decision to use Basler. The Basler ace aca1920-150uc coloured camera model, which has a frame rate of 150 frames per second in full HD resolution, was preferred in this experiment. Each camera has a unique ID number appointed during the production. Before the image sensor, as default, a C-mount lens is required. Even a camera is good in specifications, it also requires proper accessories. For the bottom camera, it was desired to work in lower-scaled area than front camera, the lens was chosen among the ones which may provide a magnified view with 100x zoom capability. For the front camera, a Ricoh Lens (FL-CC0814A-2M) was used.

5.7 ROS Environment Development

This section discusses a few specific configurations that can be applied when setting up the system. This topic might also include some algorithmic components, but those will be discussed in greater depth in succeeding topics. It is important to note that to make the entire work more easily understandable given that it includes both development and test works, as well as some of the complicated coding names were purposefully altered in a way that is more perceptible.

Looking from the start, an Ubuntu 14.04 distribution was downloaded and installed on a personal computer. The distribution preference is directly related to the support availability with the Ubuntu distribution of the used packages. This installation process description was neglected entirely since it can be accessed directly from the official website associated with it. Also, the same situation occurs for the ROS packages. Since the package distributions may be subject to change at the hands of the developers, the further details have been left intentionally vague and only the most crucial points are expressed. As the main node, a graphical user interface (GUI) called 'pema_gui' was developed and included in the 'pema_gui'. This was designed to establish

communication with the other hardware. and interact/coordinate with the other nodes. A basic schematic is provided in Figure 5.4 showing the other nodes summarizing under the types of runfiles and launch files.

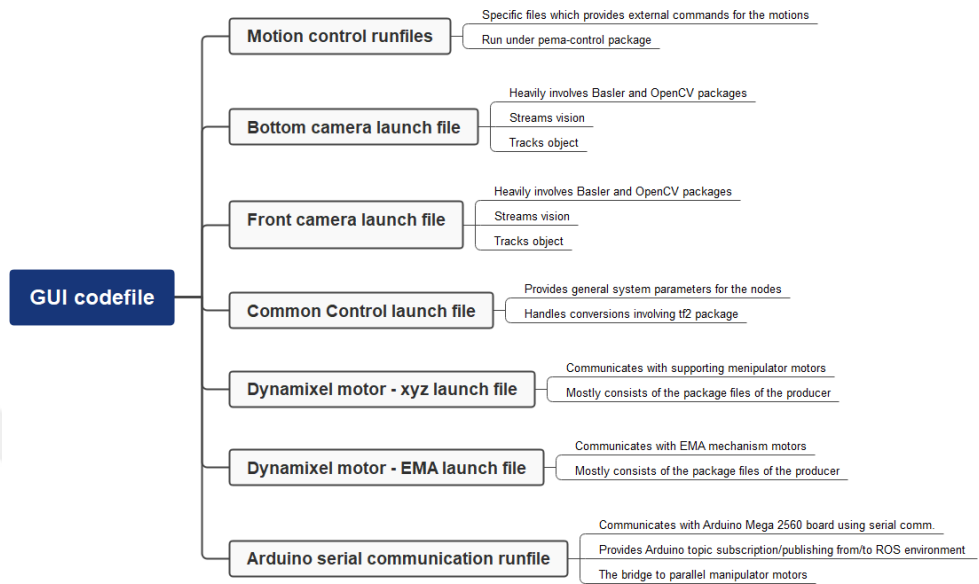


Figure 5.4 A general glance to pema_gui and the other nodes

GUI interface in ROS enables to use multiple programs at the same time called plugins. As some plugins are provided as default, users can also set their GUI interfaces and codes as plugins. Pema_gui was also defined as a plugin, even if this is not a must. A brief schematic of the used plugins is given in Figure 5.5.

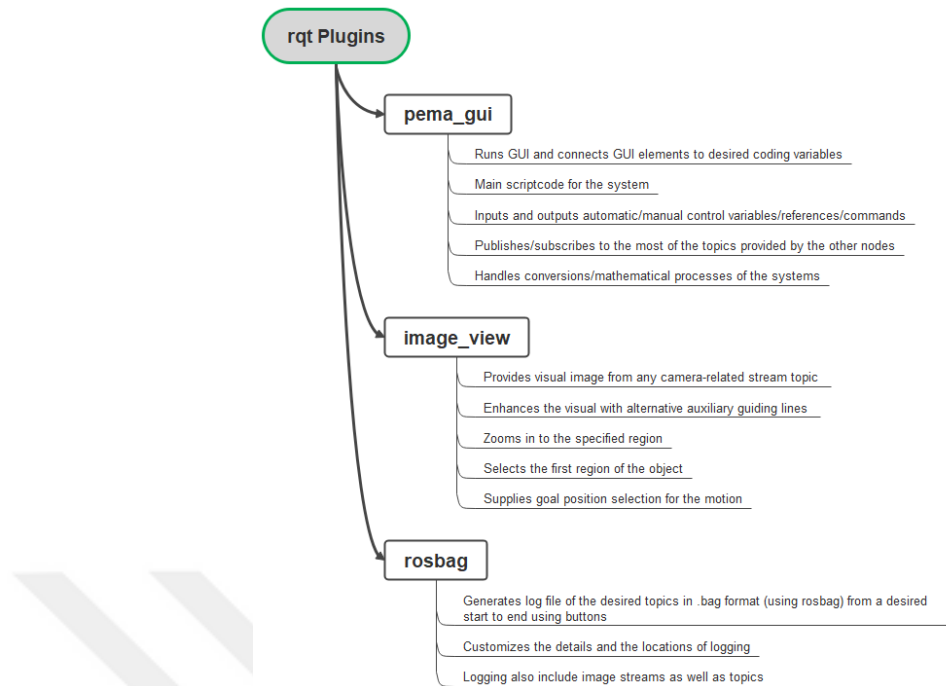


Figure 5.5 GUI plugins

5.8 Calibrations

This topic covers all the calibrations of the system elements as subtopics including mechanical or software. Even the subsidiary and parallel manipulator calibrations could be included here, they were inspected in their related titles.

5.8.1 Camera calibration

The system is equipped with two cameras, which have been given the names bottom cameras and front cameras respectively. Both cameras have different mentalities in different applications.

Bottom camera positions its visual axis along +z direction from the bottom of the microrobot environment observing only xy plane and moves with the subsidiary manipulator system. It has a x100 zoom lens and observes the environment in specific distance ranges away from the lens centre. The calibration aim is to find out the

relationship between pixels and metric distance. The most brute-force method to use a metric ruler at the working area and find out the visual conversion. The general layout of the bottom camera is given in Figure 5.6.

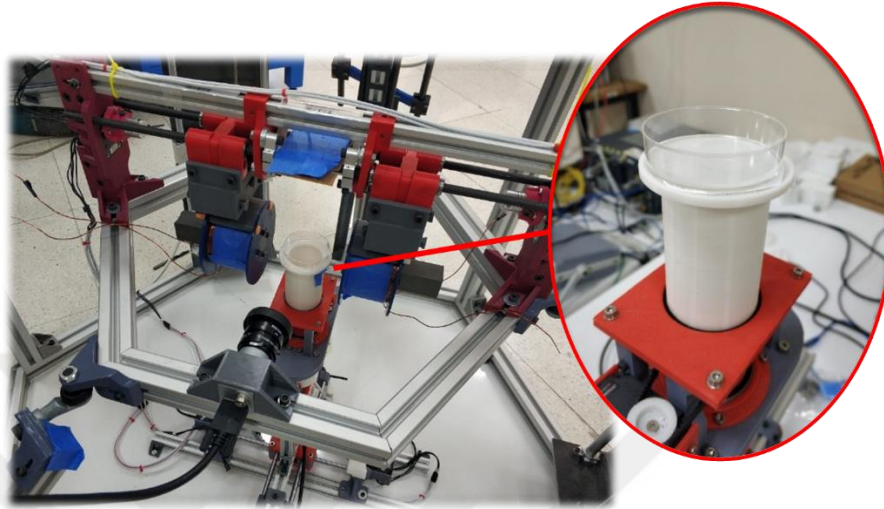


Figure 5.6 Microrobot environment and bottom camera configuration

A graph paper was utilized to determine the relation between the camera image and the microrobot environment. Figure 5.7 shows the image that was captured. The calibration tests were carried out using the PylonViewer program, which is provided by the Basler camera manufacturer. The software outputs the coordinates of the pixels over which the mouse pointer is hovering. A built-in sharpness tool also offers information about the image's quality, which may be enhanced using the lens wheel if bad result is taken. Table 5.1 and Table 5.2 show the obtained results as well as the computed transform. Here, as metric coordinates, the graph paper line intersection at the centre is assumed as (0,0). Also, it should be noted that the image resolution is 1920x1080 pixels where (0,0) pixel coordinates is assumed to be the top-left corner.

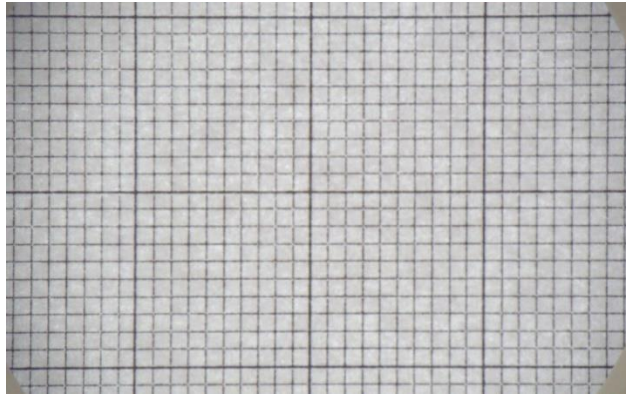


Figure 5.7 Bottom camera calibration using graph paper

Table 5.1 Bottom camera calibration readings

x axis coordinates (x,0) [mm]	Pixel coordinate along x axis	Pixel coordinate along y axis	y axis coordinates (0,y) [mm]	Pixel coordinate along x axis	Pixel coordinate along y axis
10	1462	581	10	935	48
5	1200	583	5	933	313
1	987	585	1	933	527
0	933	583	0	933	583
-1	880	583	-1	933	632
-5	670	583	-5	931	850
-10	397	585	-10	933	1119

Table 5.2 Resolution and conversion of bottom camera image

Reference coordinates in x [mm]	Resolution [mm/pixel]	Reference coordinates in y [mm]	Resolution [mm/pixel]
10 to -10	0.01878	10 to -10	0.01867
5 to -5	0.01887	5 to -5	0.01862
1 to -1	0.01870	1 to -1	0.01905
Average:	0.01878	Average:	0.01878

The results show that as expected the resolution of both axes are the same. Also, a lens warping does not occur when getting farther from the centre point of the camera image. It should be considered that the thickness of the reference lines can also affect the results, especially for the measurement of 2 mm change.

A second application is given in Figure 5.8 where a real motion application is included. This calibration also includes the determining of the reference pivot position of z rotation. The red lines represent the motion trail, and the calibration occurs as positioning the microrobot environment to $+90^\circ$, 0° , and -90° consecutively by rotating. After determining proper value of the reference point, the results showed identically equal absolute values with $+90^\circ$ and -90° positions as well as the opposite axis value of 0° position, exceeding up to 0.5 mm maximum error which may result from image processing, practical application of the fluid and error margin of the reference point selection.

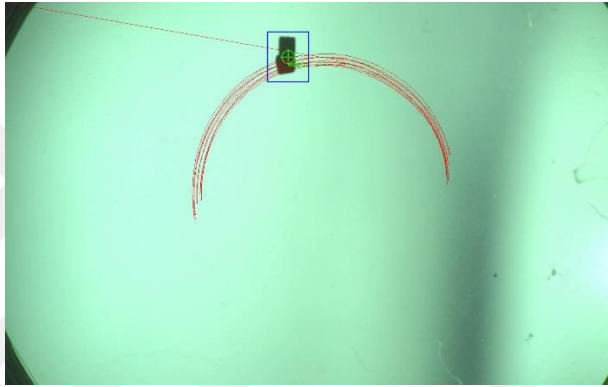


Figure 5.8 Bottom camera calibration with real application

Figure 5.9 shows the calibrating setup as well as the camera image. The application plane was aligned with the graph paper position. This camera calibration is a little bit trickier since the camera axis is not aligned with the ROI centre. For a roughly first part, this calibration phase So, the desired region is not in the centre of the recorded image and an offset occurs in the z direction. The results are presented in Table 5.3 and Table 5.4 likewise. The focused differences include intervals where the warping can be calculated and compared.

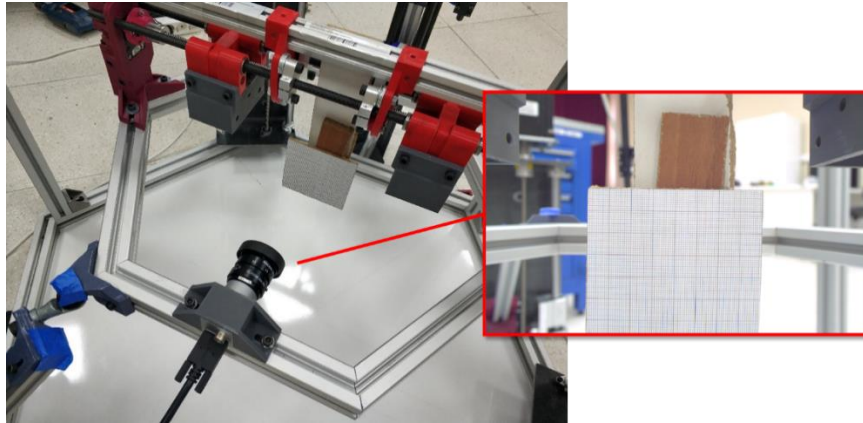


Figure 5.9 Front camera calibration bench

Table 5.3 Front camera calibration readings

x axis coordinates (x,0) [mm]	Pixel coordinate along x axis	Pixel coordinate along y axis	z axis coordinates (0,z) [mm]	Pixel coordinate along x axis	Pixel coordinate along y axis
40	1375	922	40	948	481
30	1268	922	30	947	590
20	1160	922	20	945	700
10	1051	921	10	944	811
0	942	920	0	942	920
-10	832	919	-10	940	1029
-20	723	917	-20	938	1137
-30	615	916			
-40	507	914			

Table 5.4 Resolution and conversion of front camera image

Reference coordinates in x [mm]	Resolution [mm/pixel]	Reference coordinates in z [mm]	Resolution [mm/pixel]
40 to -40	0.09217	40 to -25	0.09155
30 to -30	0.09188	30 to -25	0.09151
20 to -20	0.09153	20 to -20	0.09153
10 to -10	0.09132	10 to -10	0.091743
		0 to -25	0.092251
		-10 to -25	0.092592
		-20 to -25	0.092592
Average:	0.09178	Average:	0.091584

The front camera resolution for both axes showed similar results and insignificant warping difference that can be ignored.

Here, also a second stage of calibration is applied to verify and find out the (0, 0) point reference using a real microrobot and environment. This part is also a little bit tricky since an offset occurs with the rotation of the parallel manipulator and the camera does possess an offset distance with the microrobot. The calibrations were handled using 0, 5, 10 and 15 degrees of motion, expecting 0, 0.51, 2.05 and 4.60 mm of offsets in x global axis. After the trials and proper reference point, the maximum error was found less than 0.3 mm which may also be caused by tracker or mechanism error.

5.9 Object Tracking Algorithm

Object tracker algorithms using computer vision provides the position of an object as an output. Most of the popular and common object tracking methods utilize machine learning techniques for classification and tracking using object patterns as input. The targets may be in multiple numbers; thus, the tracking can be classified into single-object and multi-object tracking. Also, the object pattern can be used for training before or simultaneously with motion capturing, called “offline” and “online” tracker. Practically speaking, the input image may face problems like rotation of the object, object change due to motion (e.g., walking pedestrian), lightning change, interception with the environment/other objects. These algorithms generally include a motion estimation algorithm for more robust results. For the object tracking, OpenCV libraries were used.

OpenCV provides trackers with Boosting, MIL (Multiple Instance Learning), KCF (Kernelized Correlation Filters), TLD (Tracking Learning Detection), MedianFlow, GOTURN (Generic Object Tracking Using Regression Network), MOSSE (Minimum Output Sum of Squared Error) and CSRT (Discriminative Correlation Filter with Channel and Spatial Reliability) algorithms. Each of these algorithms have their pros and cons, providing its best results for specific conditions with consideration of their

algorithm basis. These pros and cons include performance categories like speed, payload, noise, accuracy, stability, and robustness.

Boosting tracking algorithm is an old but still useful algorithm, also using the same principle for a popular classifier called AdaBoost. Briefly, online boosting algorithm uses object pattern assuming as positive and the background as negative image sample. Adapting to the changes with the object, environment, and background, also estimating the next object coordination depending on the velocity, the classifier is always updated with the latest properties.

Some of the tracker algorithms were practically tested and boosting tracker algorithm was chosen in a situation that low microrobot velocity and low mechanical motion velocity were applied. Also, to enhance the tracker, a HSV (hue-saturation-value) filter was used to convert the object background to black.

5.10 Inverse Kinematic Using tf2 Package

The algorithm requires inverse kinematic of the parallel manipulator where the goal position and orientation are given as input and the joint coordinates are received as output. The motion algorithm requires an inverse kinematic functionality that the parallel robot can be controlled. In ROS environments, it is the most common and promoted method to use tf2 package for coordinate transformations. The transform map and the physical presentation is provided in Figure 5.10. First, from `global_base` to `platform_centre`, a translation and rotation variables are relayed. Basically, the platform center and the spherical joint coordinates CG1, CG2 and CG3 points coordinate frames share the same xy plane but different directions and origin points.

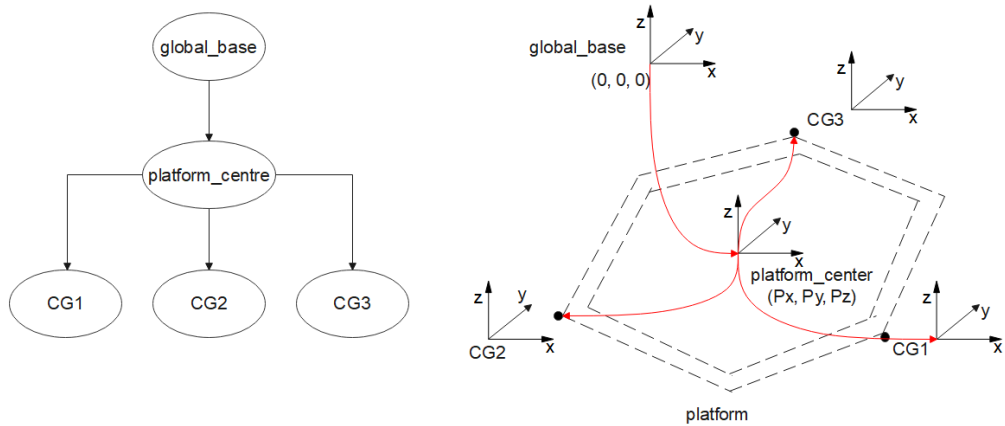


Figure 5.10 tf2 conversion of the inverse kinematic

The next step for calculation is given in Figure 5.11. As the spherical joint coordinates are found, it is possible to reduce the problem from 3D to 2D vectors. The only unknown link variable d can be easily calculated using analytical calculations. These Euclidean planes have 120° of difference between them, so that from `platform_centre` to joints the transformations have a 120° shifting and a translation at the distance of platform radius.

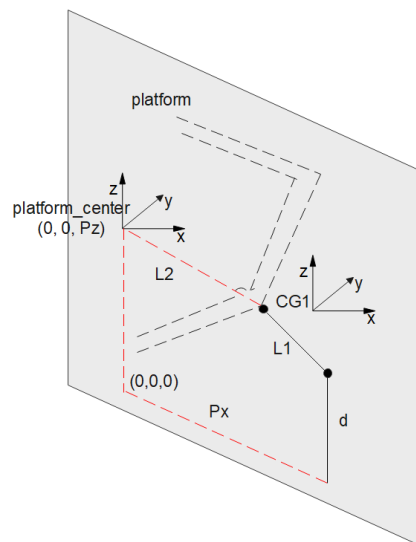


Figure 5.11 Calculating d on Euclidean plane

5.11 Operating Principles of Nodes and Control Algorithms

Summing with the studied applications, it is better to divide those application algorithms into sub algorithms for clarification. First, a general layout for the motion and the required components are given in Figure 5.12. This graph given in a simplified way on purpose for better understanding and not getting lost with the details.

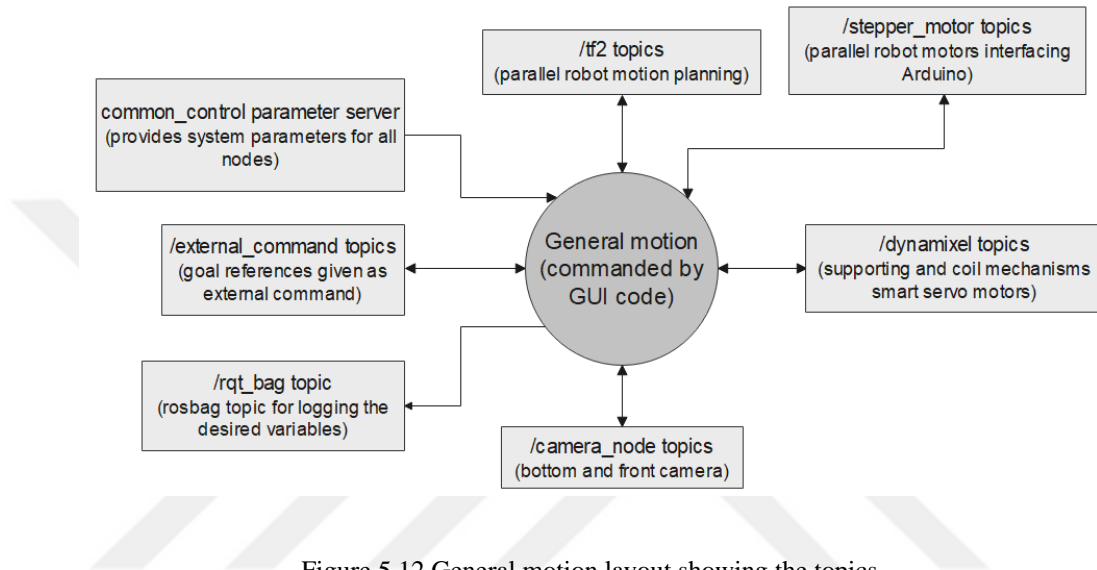


Figure 5.12 General motion layout showing the topics

Closed loop control for each motion configuration requires the present coordinates of the mechanisms and the microrobot. So that it is crucial to analyse and program the transforms between them. The microrobot coordinate transformation with subsidiary actuator mechanism is given in Figure 5.13. While the full chain of the global position of the microrobot is calculated a direct transform from O to P_3 point, the practical calculations are handled using sensor feedbacks of the transforms between $O-P_1$, P_1-P_2 and P_2-P_3 in series chain. In more details, the first chain consists of the translation motion of the manipulator on xy plane, the second chain is defined as the position of microrobot captured using camera, the third chain includes the rotation of the microrobot environment using the rotation motor of the actuator.

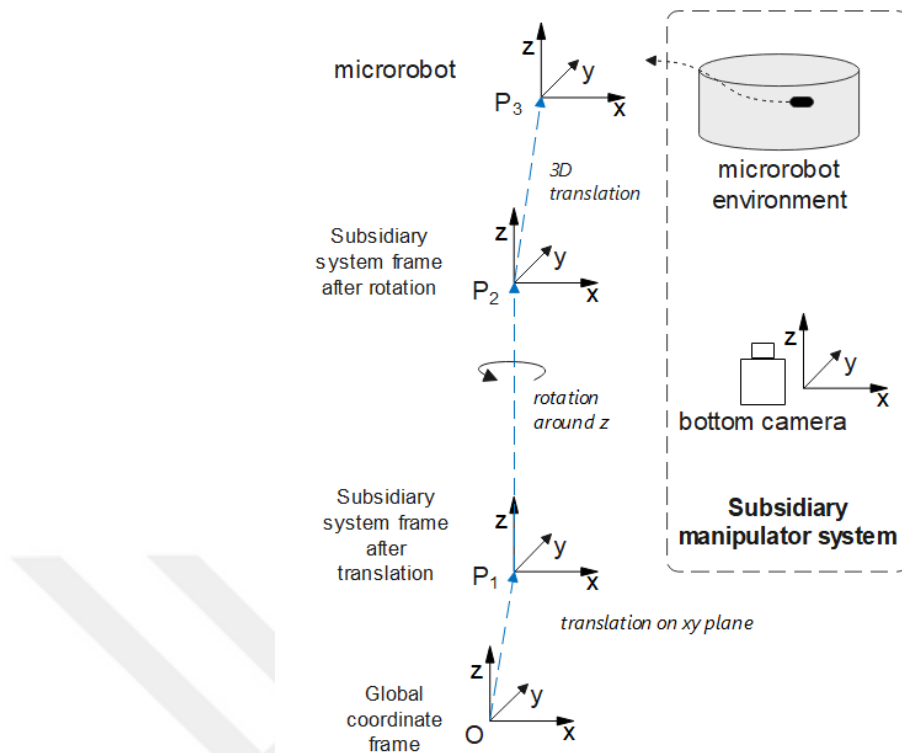


Figure 5.13 Subsidiary manipulator system and coordinate frames

Likewise, the parallel manipulator system coordinate system transformations are given in Figure 5.14. The parallel manipulator system position and orientation data is already known by the user. The front camera is positioned to observe the xz plane where the centre point is calibrated for conversion from camera pixels to cartesian coordinates, stated as O-P₄ transform. It should be reminded that the microrobot environment is in the visual range of front camera. Using this info, the microrobot position on xz plane is determined using front camera, i.e. P₄- P₅ transform.

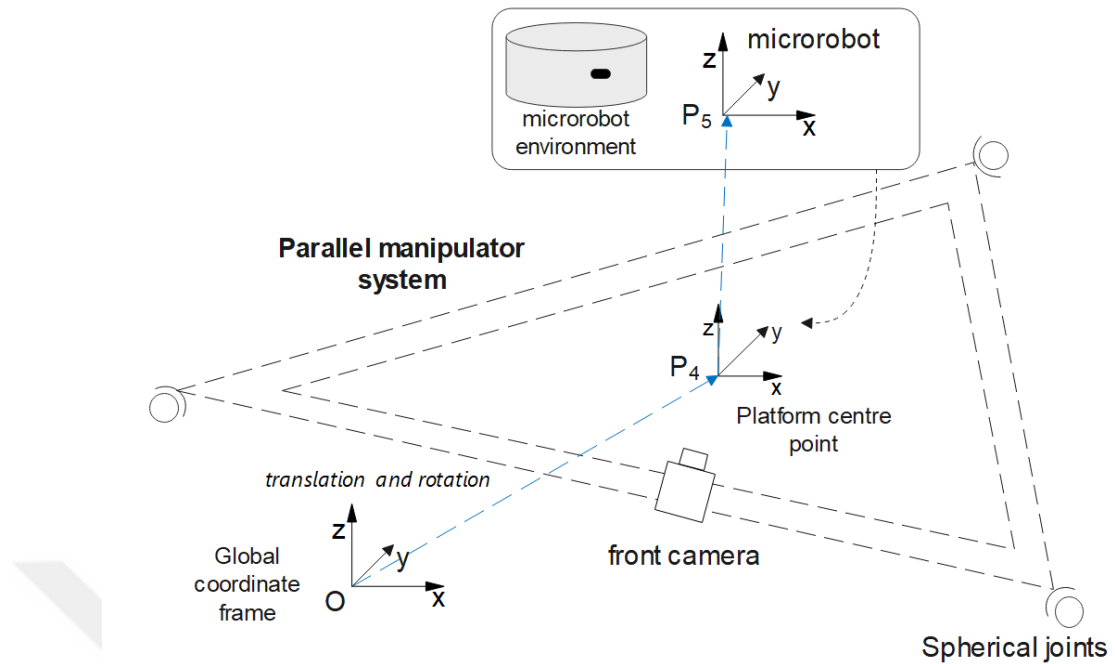


Figure 5.14 Parallel manipulator system and coordinate frames

The motion modes can be briefly summarized as motions on xy and xz planes. These motions require feedbacks from two different sources and these sensors are mounted on different manipulators with distinct functionalities. For a proper start, simply the mechanism calibrations (zero referencing) should be properly accomplished.

During the motions, as known, the manipulators should aim to hold the microrobot at the ROI centre point. To do that, with both motion concepts, a sub-motion is defined as ‘snapping’. When snapping function is on, simply the control algorithm tries to lock the microrobot at the ROI centre by using some snapping reference coordinates. Snapping function is the fundamental base for all the motions.

A brief and general motion algorithm for all motions is given in Figure 5.15. If elaborated, firstly ROS environment launch and runfiles are run, then GUI environment is started. The calibration phase consists of conversion constants, camera-related zero-point coordinates, physical motions for manipulators’ starting points and camera HSV filter setting for camera object tracking phase. The motion modes include xy , xz and xyz motions which refers the spatial medians of microrobot motion. Picking

up the motion mode effects the microrobot position camera feedback source and the algorithms of motion which will be used in motion command calculations during snapping. When snapping function is activated, the algorithm does not only track the microrobot but also applies the commands from GUI or external command nodes for complex or sequential motions, involving manipulators and EMAs. Then, evaluating the position error, the proper commands are generated and sent to the appropriate motion controllers. After that, the loop repeats till the function is turned off.

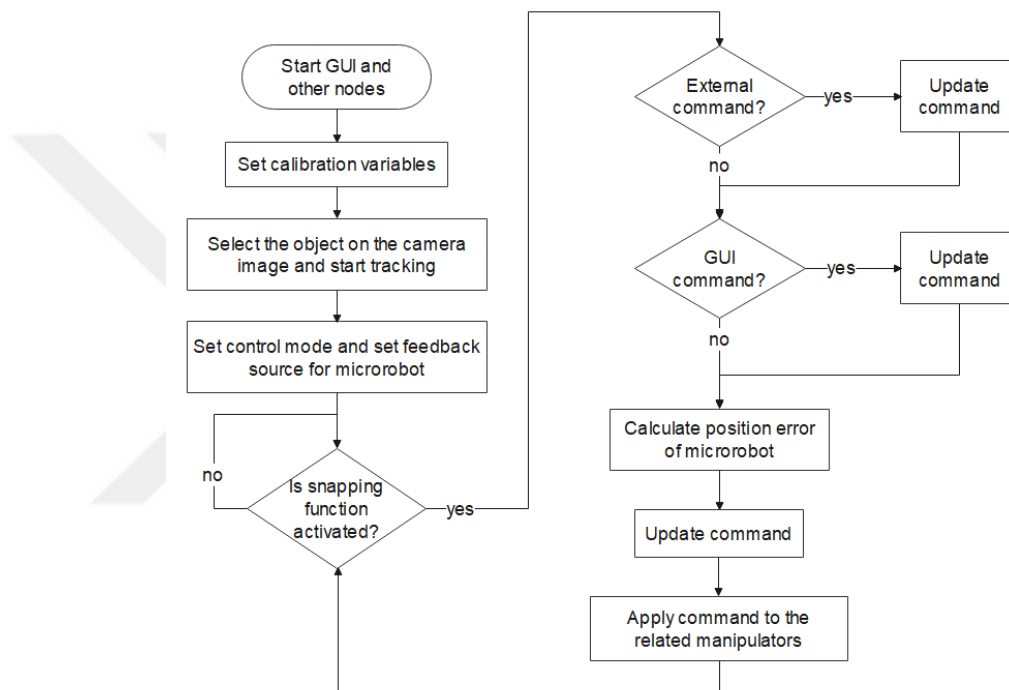


Figure 5.15 A brief and general motion algorithm flowchart for all motions

For pure motion on xy plane (ignoring parallel platform and front camera feedback, assuming that electromagnetic actuator axis height is set properly with respect to the height of the microrobot on global coordinates), alongside the feedback data of subsidiary manipulator motors, only the bottom camera (mounted on the subsidiary manipulator) is used for microrobot position determination. The snapping function concept is given in Figure 5.16. Depending on the concept, the subsidiary actuator starts at the zero-reference configuration that the bottom camera (0, 0) coordinate aligns with the ROI centre. Here, microrobot does not have to be at (0, 0) point. When

the snapping function activates, the subsidiary system centres the microrobot at the ROI centre point. This starting point coordinates of the subsidiary system is registered as ‘snapping reference point’. When EMAs exert force on microrobot and changes global position of microrobot, the global position of the microrobot is determined with respect to the subsidiary manipulator z rotation feedback raw camera feedback which are directly used for coordinate transform.

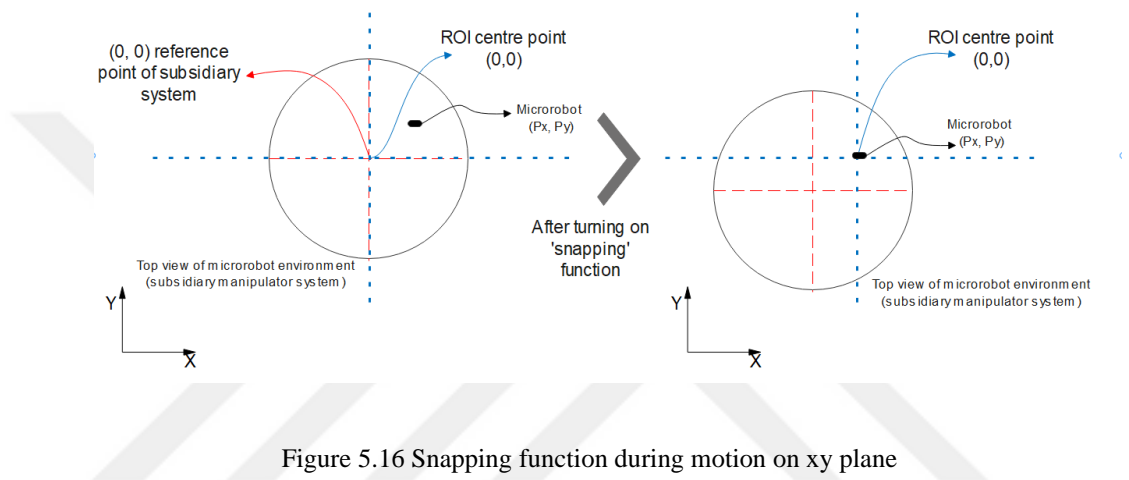


Figure 5.16 Snapping function during motion on xy plane

For pure motion on xz plane, excluding bottom camera feedback, all the camera and manipulators are utilized. The snapping function concept is given in Figure 5.17. It refers that, with a proper camera calibration, any manipulator referencing process is not required. The front camera feedback generates the motion command for snapping function. Different from xy motion, xz motion utilizes a different ROI centre, using x offset compensation distance (due to platform mechanism rotation) on x axis and also z gravity compensation distance on z axis. These motions are supplied by both manipulators.

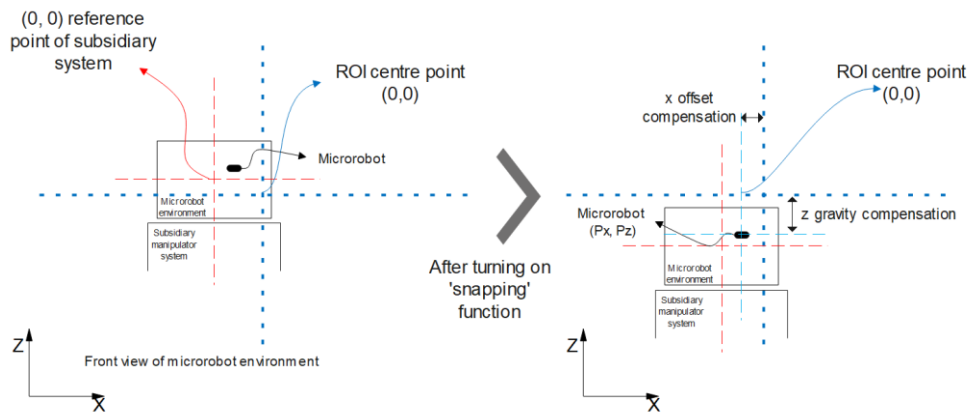


Figure 5.17 Snapping function during motion on xz plane

5.12 User Interface

GUI mainly consists of three types of plugin module. The main plugin consists of the manipulator system exclusively developed interface and codes. The others are custom image and rosbag plugins which were developed by other developers for general purposes. The interfaces are given in from Figure 5.18 to Figure 5.24.

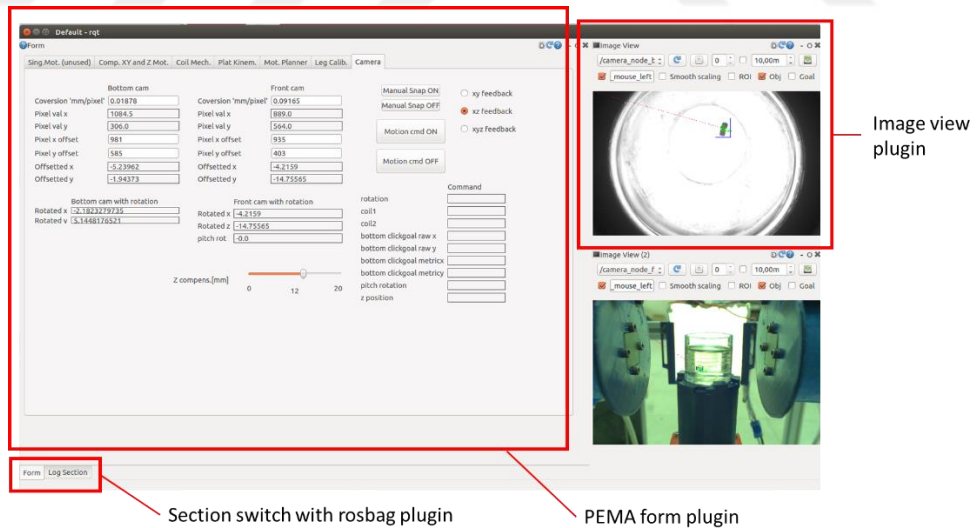


Figure 5.18 General GUI layout with plugins

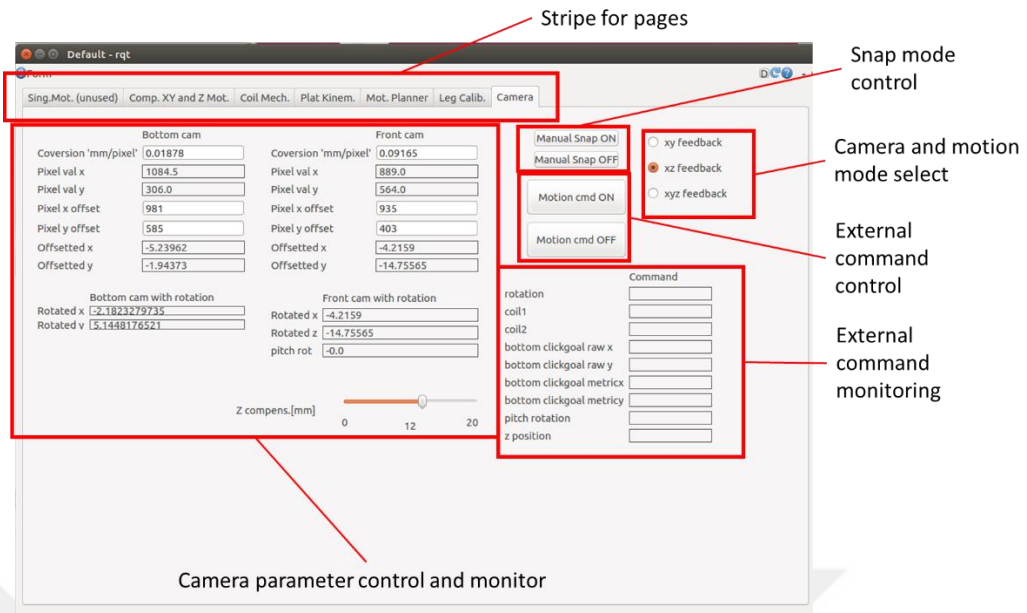


Figure 5.19 GUI camera control page overview

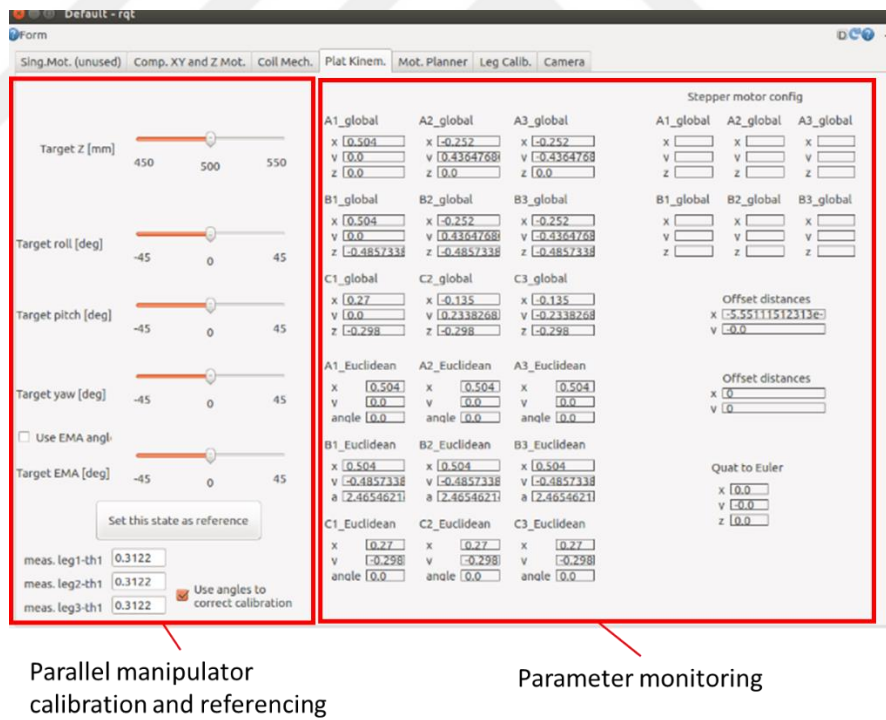


Figure 5.20 Parallel manipulator calibration, referencing and monitoring page overview

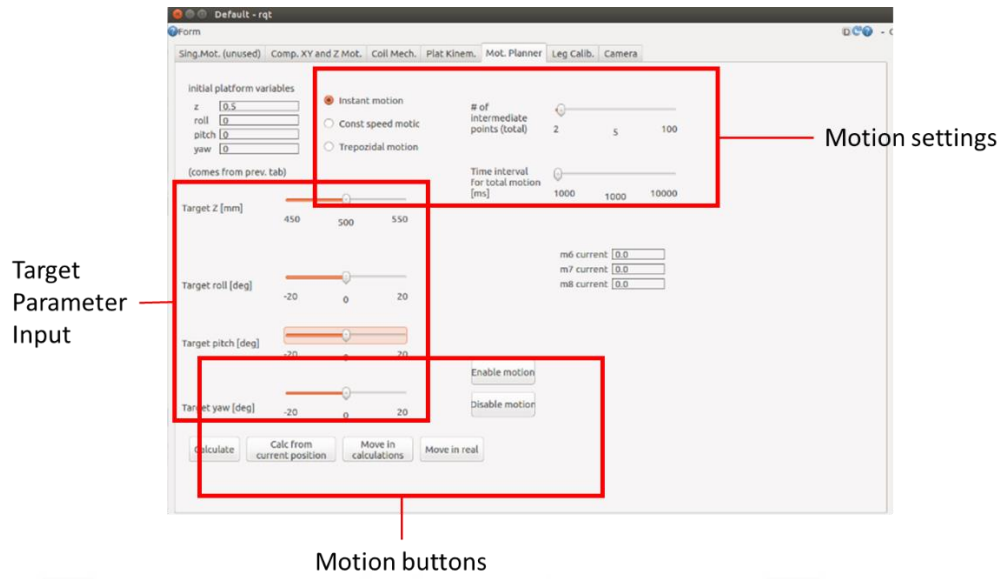


Figure 5.21 Parallel manipulator motion control page overview

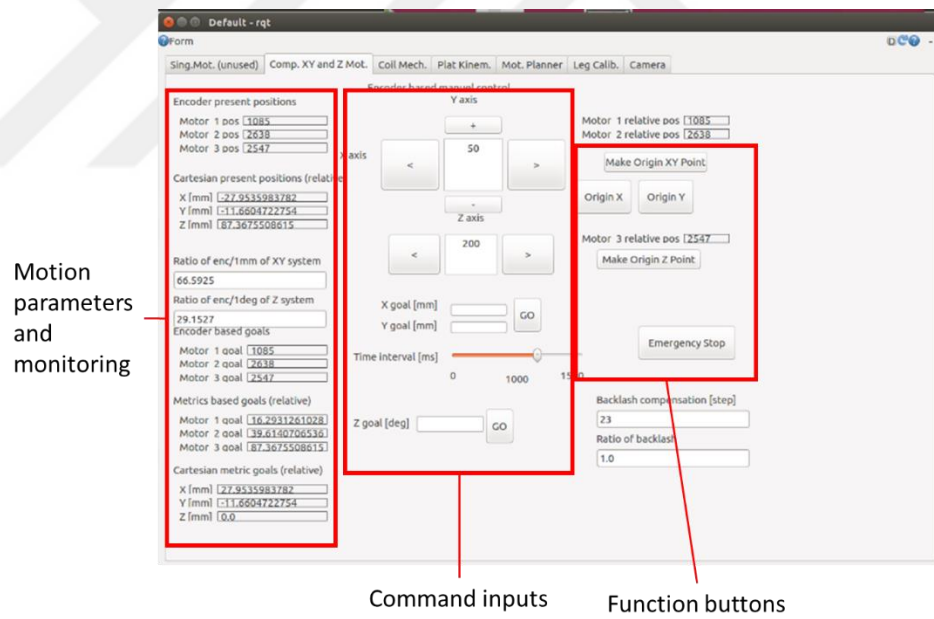


Figure 5.22 Subsidiary manipulator page overview

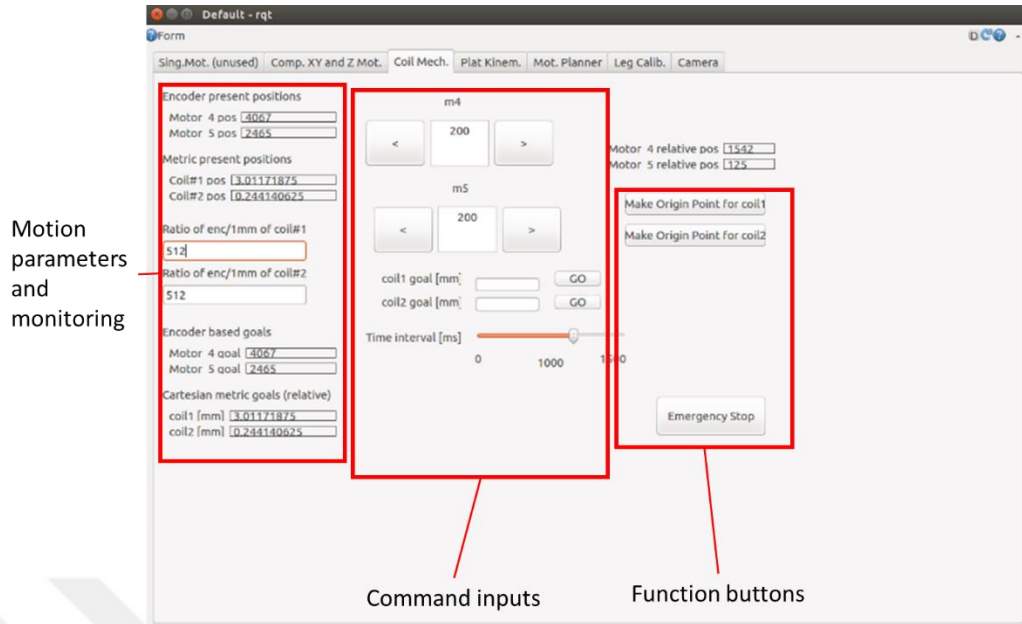


Figure 5.23 EMA mechanism page overview

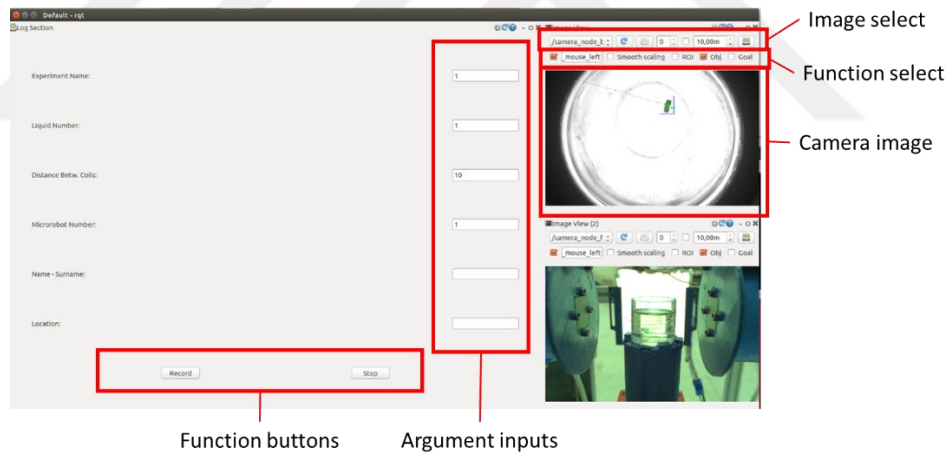


Figure 5.24 Rosbag and camera image plugin page overviews

CHAPTER 6

MOTION APPLICATIONS

6.1 Introduction

In this chapter, the motion applications of the manufactured system were accomplished. Therefore, firstly the required EMA system proof applications were handled. Then, then the aimed motions were presented. These all motions follow a closed-loop feedback control. The aimed motions are based on xy and xz planes. The system motions were tested with biomedical application approach, i.e., balloon shaped cerebral aneurisms models.

6.2 Biomedical Application: Aneurisms

Aneurism is a medical phenomenon occurring in the blood vessels that deforms the weak vein walls in some shapes like bulge, bubble, etc. This deformation may occur in human body parts with high blood pressure, especially arteries and brain, and with a probability of finishing up with rupture or blood leakage. The reason of aneurism may originate from smoking, high blood pressure or family gene history. Some common aneurism types are given in Figure 6.1.

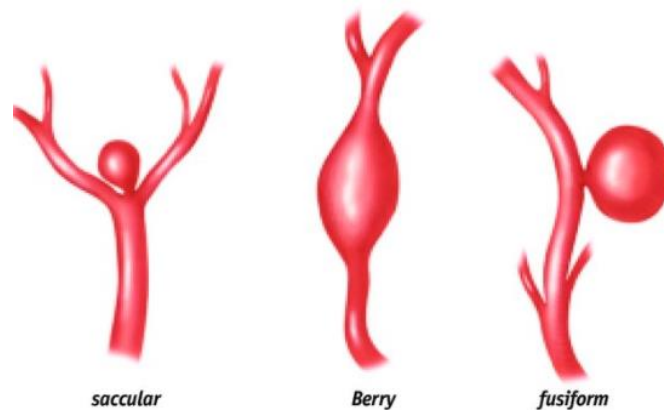


Figure 6.1 Common aneurism types (Wright, 2007)

Depending on the types of the aneurysms, the treatment method also varies. To briefly explain, intracranial aneurysms are the most difficult ones. The aneurysms do not show apparent indications and with a rupture situation it is hard to operate since the brain is vital and the phenomenon difficult places hard to reach and open surgery is dangerous or impossible for deeper cerebral arteries. The cerebral vein system model is given in Figure 6.2 and an aneurism occurrence example is given in Figure 6.3.

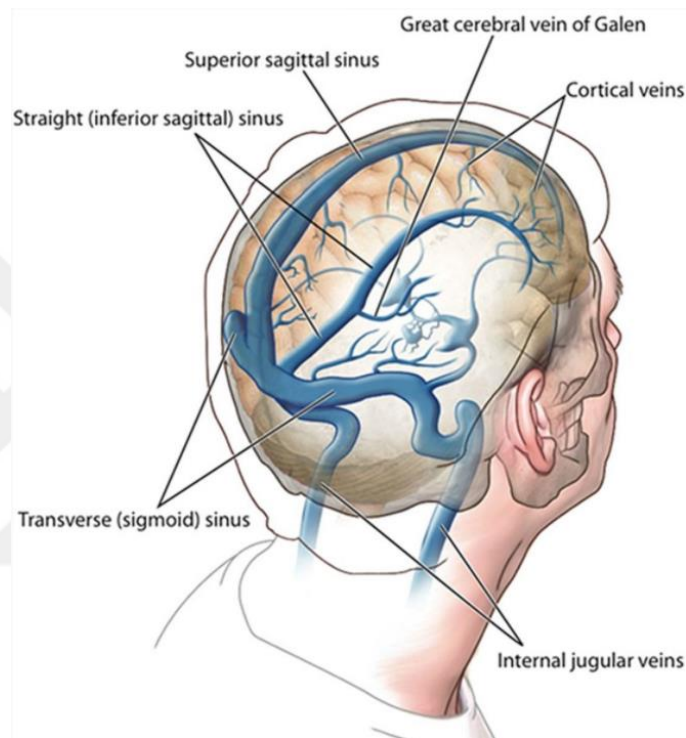


Figure 6.2 Cerebral vein system (Moll & Waldron, 2014)

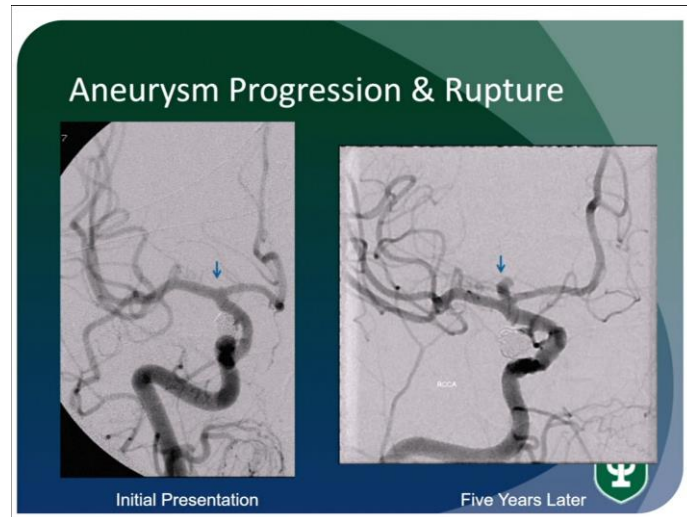


Figure 6.3 An aneurysm occurrence (Moll & Waldron, 2014)

Today, three methods are commonly applied for treatment. First method is clipping, which is an open operation. It allows the surgeon to reach to the deformed wall and the wall is clipped with a latch-like apparatus. The second method is using stent. Applying a stent to the deformed part helps to reduce the pressure to the wall, also regulating the blood circulation. The third method is coil embolization. The bulge or balloon-like deformed part is filled with wire material to support the wall and prevent blood pressure. Last two methods deploy a catheter. In their own scopes they also have their own challenges. Following the medical developments, except the performance with the treatment, increasing the operation comfort and decreasing the recovery time are important.

Researchers emphasize that microrobots can be employed for aneurysm treatments. However, finding a direct study in the literature about microrobot deployment for aneurysms is very rare, even number of studies for microrobot manipulation is this high. In a research, a helical robot was locomoted by tomographic magnetic particle imaging and employed into an aneurysm phantom (Bakenecker et al., 2021). The mentioned phantom is given in Figure 6.4. Other inspected works mostly include the concept that a catheter is deployed.

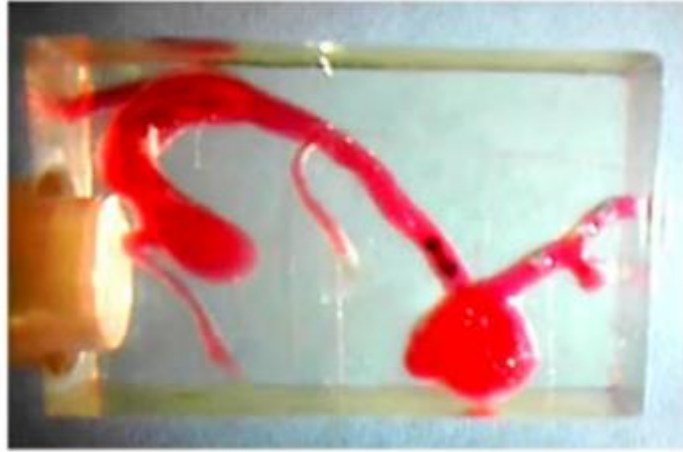


Figure 6.4 A phantom aneurysm model with a microrobot inside (Bakenecker et al., 2021)

6.3 Force Tests

As mentioned before, the force tests give the drag force constant and reveal the drag force mathematical model for calculations. The force tests were applied on xy plane closed loop control. During the force tests, the cylindrical microrobot with 1 mm diameter and 2 mm height was used. The microrobot environment was kept in a petri dish. The current was kept constant as 2 A.

The practical application bred an unexpected result. The drag force which is mostly consist of the adhesion force of the microrobot environment opposes the microrobot to move even if the bottom surface was smooth. The practical experiences showed that the adhesion kept rising when getting closer to the walls.

To prevent this unexpected effect, the gravity should be compensated. The compensation configuration is given in Figure 6.5. Using the practical experiments on xz plane, using the same configuration and the required gravity compensation was found as 12 mm. This situation is presented in the next section.

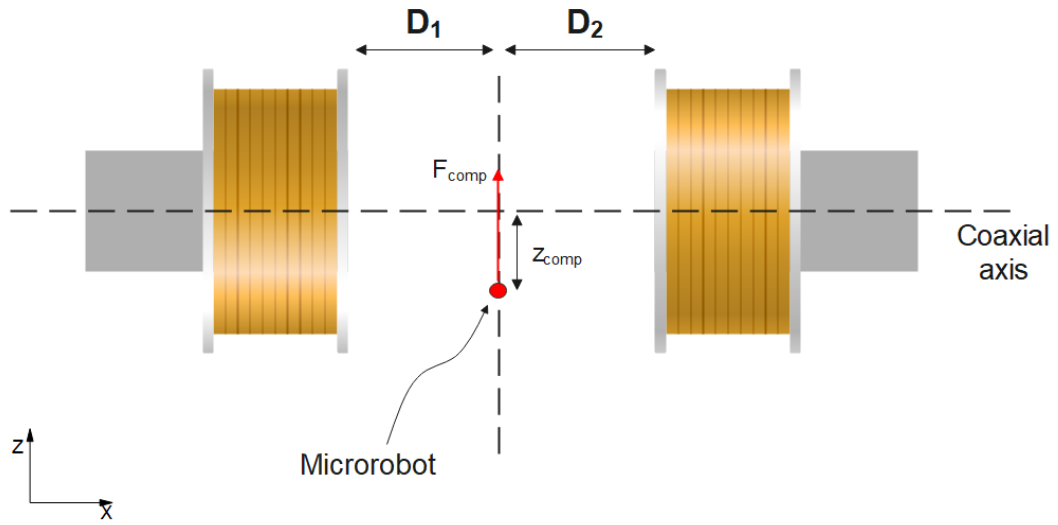


Figure 6.5 Gravity compensation configuration

In simulation, since the changes are too low, it was unable to get clear solutions. So, if this value was calculated, the equation equilibrium is given in Equation 6.1 and 6.2.

$$F_{comp} = F_{grav} - F_{bouy} \quad (6.1)$$

$$F_{comp} = 5,95 \cdot 10^{-5} - 1,48 \cdot 10^{-5} = 4,41 \cdot 10^{-5} N \quad (6.2)$$

Since this compensation is a result of magnetic gradient shown in Equation 6.3 and 6.4.

$$\mathbf{F} = v(\mathbf{M} \cdot \nabla \mathbf{B}) \Rightarrow 4,41 \cdot 10^{-5} N = 1,57 \cdot 10^{-9} \cdot \nabla B \quad (6.3)$$

$$\nabla B = 0.294 T/m \quad (6.4)$$

Using the new information with the gravity compensation, applying 12 mm of z compensation, the force experiments were repeated for 10, 20, and 30 mm asymmetry parameter. An example figure with the motion on xy plane is given in Figure 6.6.

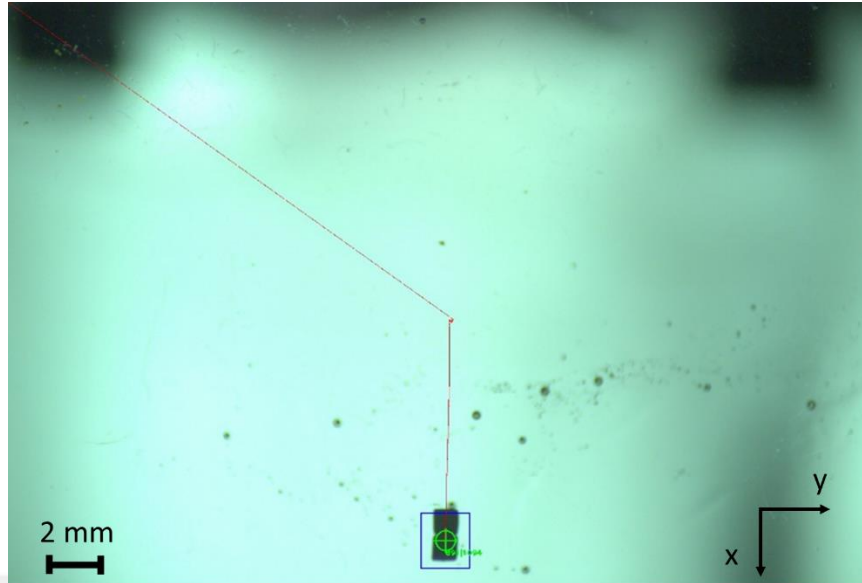


Figure 6.6 An example force test motion from centre towards to an EMA

The acquired results are presented in Table 6.1. Using the relationship between design and the compensated motion experiment, an approximating was obtained as in

Table 6.1 Experimental constant velocity results with different asymmetry parameters

Sample #	Velocity [mm/s]	Velocity [mm/s]	Velocity [mm/s]
	$\epsilon=10$ mm	$\epsilon=20$ mm	$\epsilon=30$ mm
1	0.57	0.8885	0.9
2	0.46	0.8353	1.105
3	0.5	0.804	0.95
4	0.502	0.833	1.133
5	0.476	0.835	1.028
Mean	0.5016	0.83916	1.028

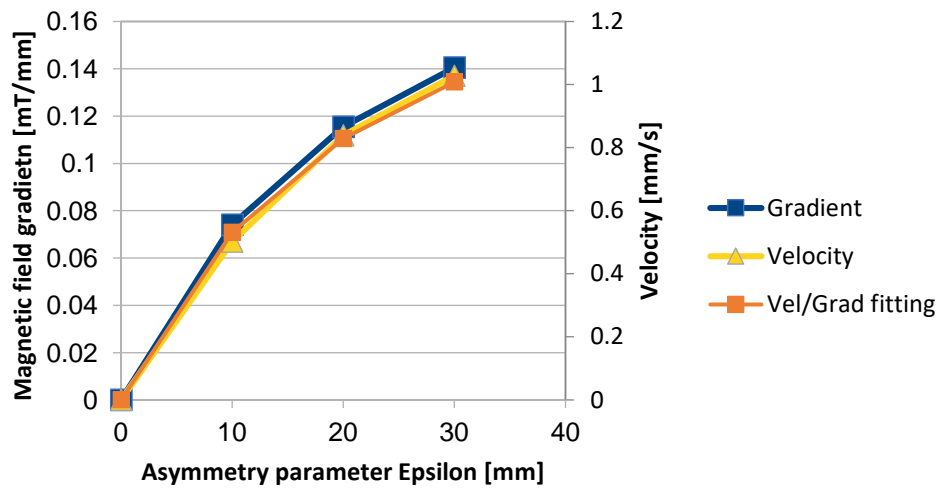


Figure 6.7 When constant ratio 7.176 applied, the gradient velocity relationship

The relationship between gradient and velocity can be given with the conversion constant C_d/C_m as 7.176 constant and causing $9.4e-06$ RMS error after aligning.

6.4 Programmed Control Motions

All the motions consist of closed-loop control with visual feedback, based on two fundamental plane motions, xy and xz . Some of the applications and example results were presented in subsections.

6.4.1 Programmed Motions on xy Plane

The motions on xy plane uses no parallel platform motion. At the start of the motion, the subsidiary manipulator system must be started at the reference point (i.e., zero point). Bottom camera is the only camera that works during this motion mode. Also, to generate force and torque, EMA mechanisms are actively working.

In this motion, to accomplish a point-to-point motion to a desired position, basically the microrobot position should be rearranged depending on the orientation of the desired goal. It can be seen that, on the global the locomotion is only in x direction.

The motions on xy plane consist of two different applications. The first presented motion couple proves pure motions along x and y axes, separately. The second presented motion includes a constrained motion at the shape of an aneurism. The scenario is to manipulate and send the microrobot at inside the balloon shaped aneurism and then take it out again. The assumption is that the microrobot equipped with a treatment method (e.g., medicine, plug, etc.) and activates it inside the aneurism.

The fundamental motions in both x and y axes separately consist of two stages. Those applications reference the position in global coordinate system as the output. It should be reminded that snapping function does keep the microrobot at the centre of the platform all the time. First stage includes torque configuration. During the 90° of rotation, the torque configuration is applied but it does not disturb to the microrobot. After the subsidiary rotation, a pure one-axis 5 mm motion occurs. Technically, if a point-to-point motion is needed, both subsidiary manipulator translation and rotation motions should act at the same time.

The mentioned first motion is given in Figure 6.8. In the first part of the total motion, the robot moves in global frame, and it does not move in the local frame. With the second part, it is opposite of the first situation. The robot moves in the local frame and does not move in the global frame. Also, the plots are given in Figure 6.9 and Figure 6.10.

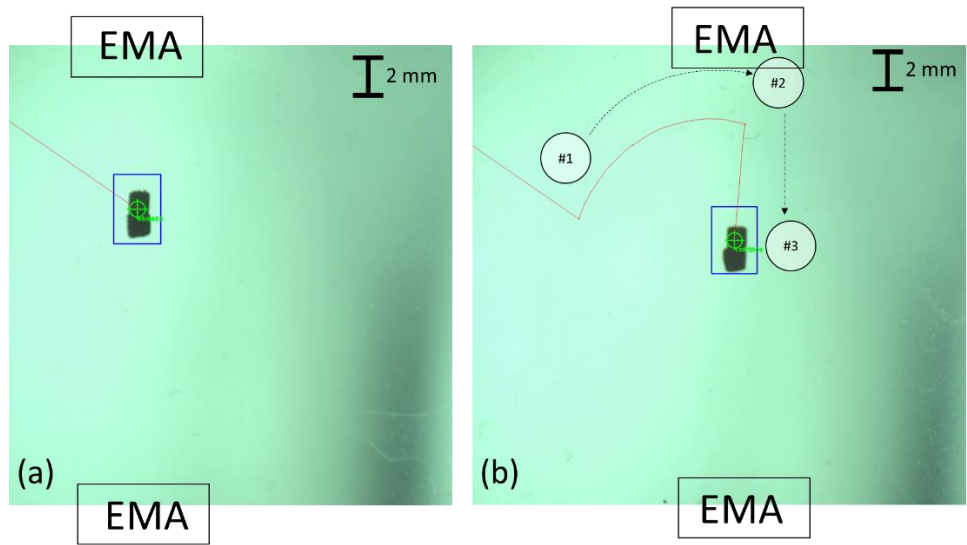


Figure 6.8 x axis pure motion capability test (a) EMAs snap and follow the microrobot (b) between 1-2 there is 90° subsidiary actuator rotation and EMAs only follow in homogenous configuration as between 2-3 EMAs apply gradient configuration and cause local motion

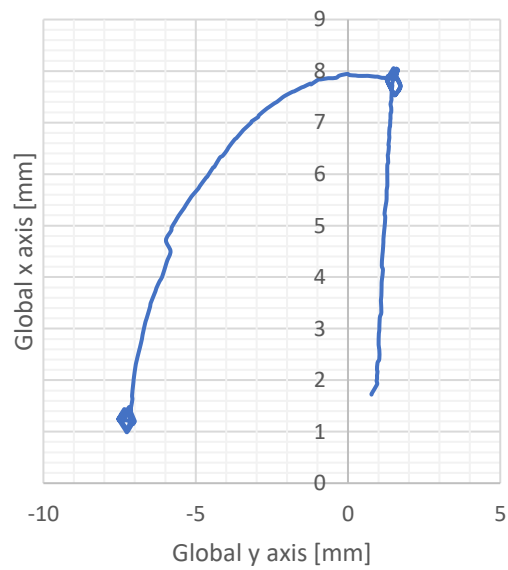


Figure 6.9 x axis motion position plot with global (spatial) positions, first making the circular shape

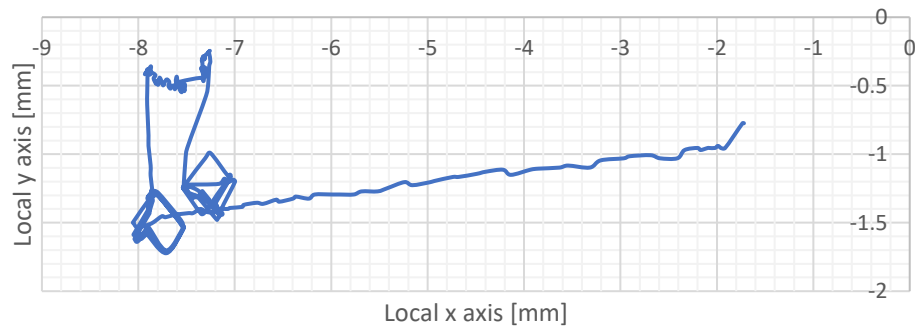


Figure 6.10 x axis motion position plot with local (raw camera reading) positions, last making the straight line

The second motion phase was ended using a closed-loop control algorithm which checks if the targeted position is reached or not. After accomplishing 5 *mm* of straight motion in the end of second phase, the control algorithm transients from gradient configuration to torque configuration. It was observed that the absorption of the existing velocity motion took time and passed the target point.

Like the previous application, nearly the same microrobot motion can be seen in Figure 6.11. Looking to the results, the similar motion was accomplished in the same global direction. However, the local framework registers a motion in the opposite direction.

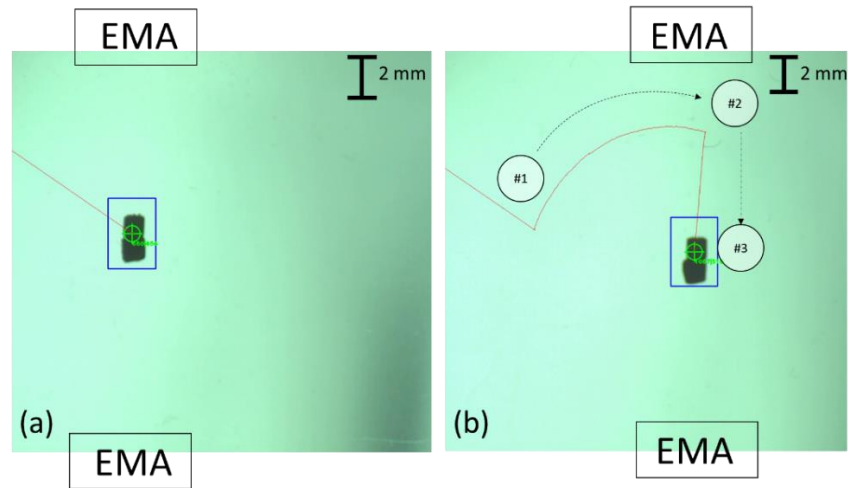


Figure 6.11 y axis pure motion capability test (a) EMAs snap and follow the microrobot (b) between 1-2 there is 90° subsidiary actuator rotation and EMAs only follow in homogenous configuration as between 2-3 EMAs apply gradient configuration and cause local motion

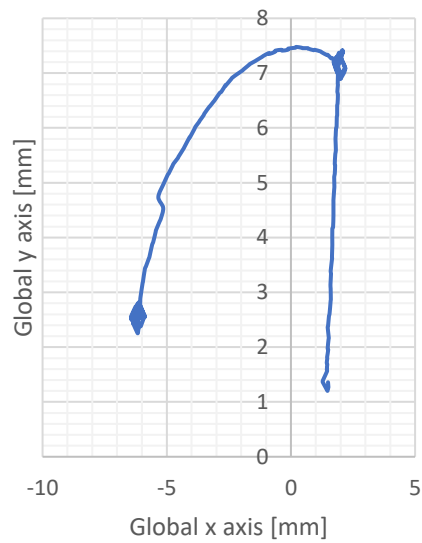


Figure 6.12 y axis motion position plot with global (spatial) positions, first making the circular shape

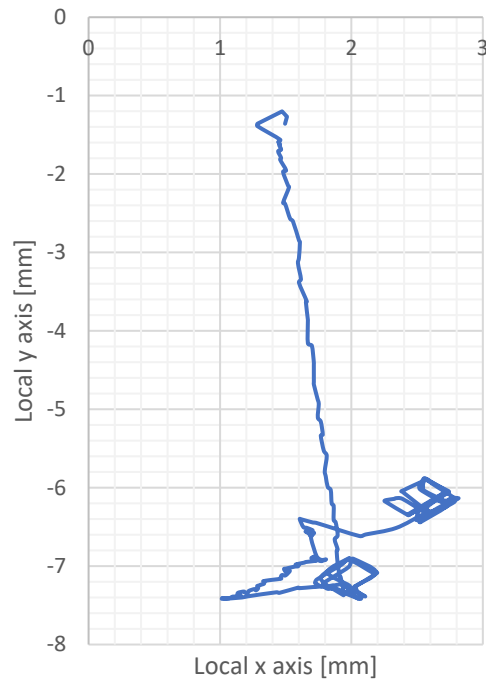


Figure 6.13 y axis motion position plot with local (raw camera reading) positions, last making the straight line

For the second application on xy plane for biomedical applications, a simple aneurysm model was manufactured. The constrained environment application consists of a straight canal (vein) with the width of 5 mm and an aneurysm at the middle with the throat of 3 mm width. This model is shown in Figure 6.14. The structure was constructed from transparent PLA material. The model was then submerged into the petri dish.

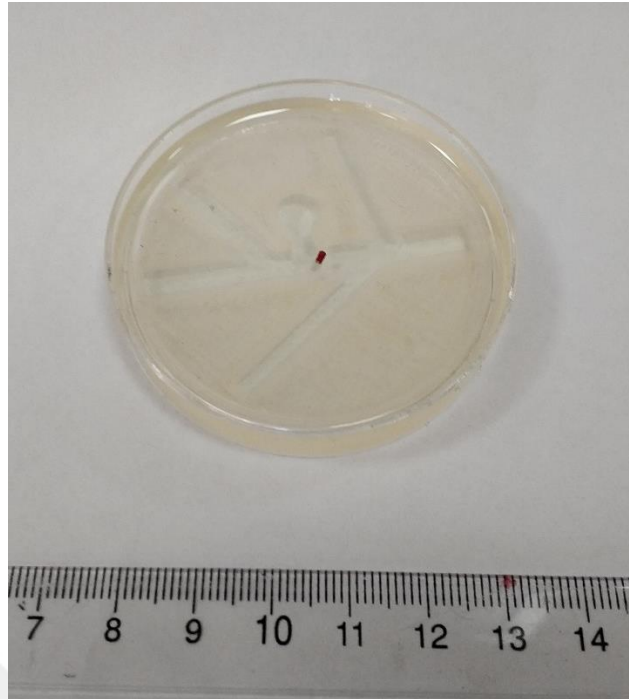


Figure 6.14 The developed constrained xy motion model

Using a click-based goal position closed-loop control, the microbot is manipulated to the registered position. The goal is selected using the camera image plugin. An example of the applied motion is given in Figure 6.15 and Figure 6.16. Total of 5 position targets were applied respectively as the microbot arrives to its next destination.

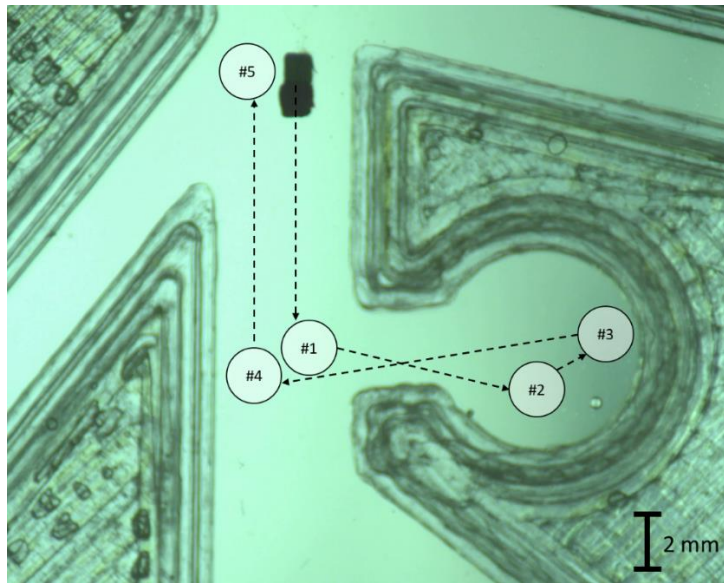


Figure 6.15 Guided motion control that the goal position is given by mouse click, the clicked positions during the motion marked in order

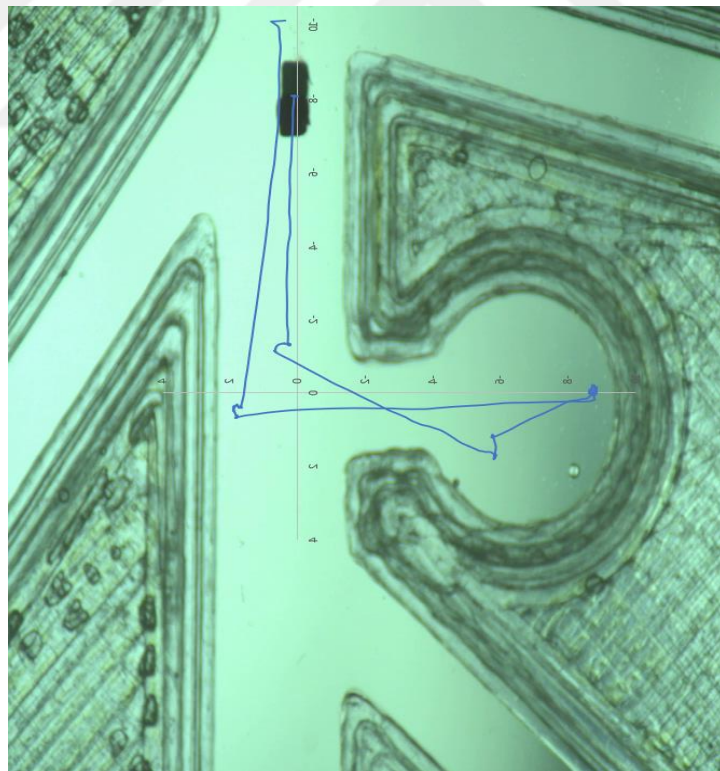


Figure 6.16 The motion result plot (mirrored for better observation)

6.4.2 Programmed Motions on xz Plane

The motions on xz plane uses requires parallel platform motion. Front camera is responsible for the position feedback of the microrobot for this motion mode. The subsidiary system provides the necessary motions for the microrobot environment. Different from other motion mode, subsidiary system is not required to be strictly referenced to absolute zero reference point at the beginning.

This motion requires proper microrobot environments for the motions, especially a phantom for aneurysm applications. Thus, some phantom models were studied using resin and silicon mould. The aim was to create an aneurysm environment inside the thin resin blocks. Some of the examples are given in Figure 6.17. The production method was left for a more convenient one.



Figure 6.17 The resin models and their silicon moulds for xz motion

The transparent plex glass is a proper material for transparent visualization, also having a proper method for sticking them together. Thus, it is much easier to manufacture different models. Some of the plex glass models are shown in Figure 6.18 and Figure 6.19. These models have 30x50 mm dimensions and were filled with the microrobot environment fluid.



Figure 6.18 Most used model for xz motion

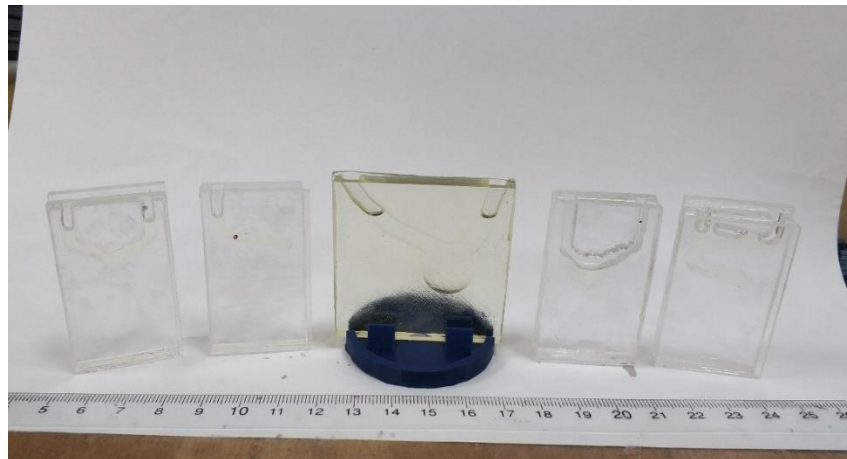


Figure 6.19 Applicable models for xz motion

It should be noted that, these models have very limited contact to outer environment. Also, the models have narrow canals. So that, the fluid characteristic can show some changes. As expected, depending on the phantom model and position, more

resistance by the environment was perceived. It is believed to be originated from increased and approached walls that increases the adhesion force.

Before the applications, the gravity compensation determination should be presented. An example compensation work is given in Figure 6.20. While the gravity compensation is applied (12 mm offset in z direction), the height of the microrobot does not change during the motions along x axis.

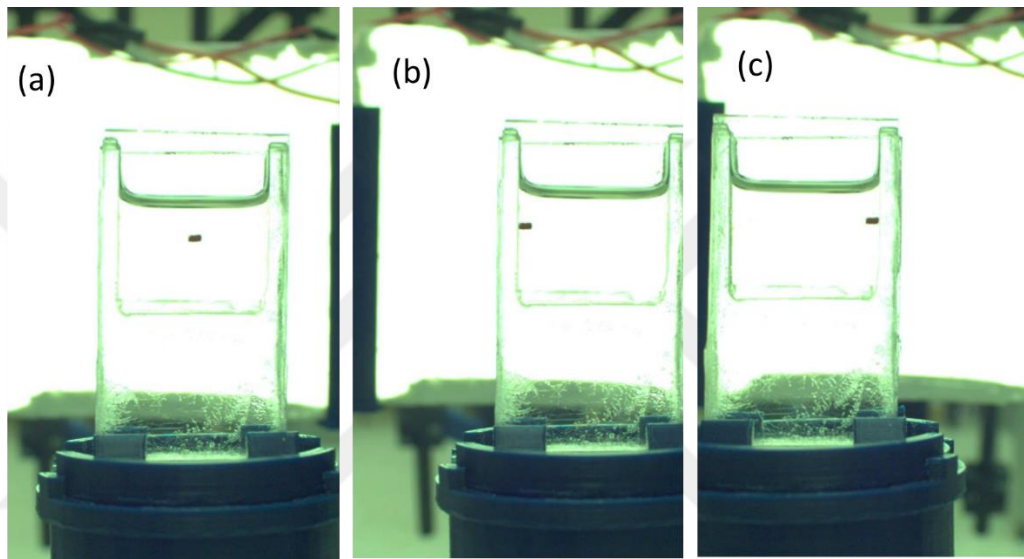


Figure 6.20 The gravity compensation and motion along x axis

With any motions without exclusive conditions, microrobot can be delivered on xz plane. For the motions along x axis EMAs are deployed, and along z axis the gravity compensation is changed. Lowering the gravity compensation (providing less force for floating) causes the microrobot to submerge and vice versa. Also, it is seen that, with the aid of gravity compensation, the microrobots can also climb the inclined surfaces without using a proper angular rotation if any obstacle is not detected. But this motion might not be convenient for the situations.

These motions were tested using model shown in Figure 6.18. Different from xy plane goal-based controller, the exerted forces are controlled by the user/operator using closed-loop controller. The application and its scenario are shown in Figure 6.21.

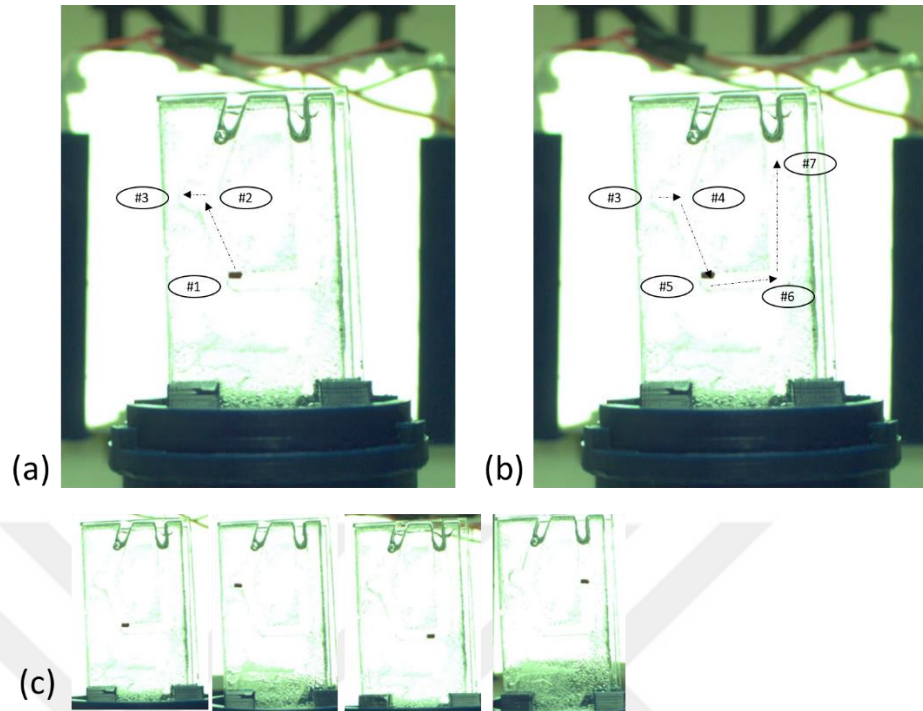


Figure 6.21 Aneurysm application on xz axis (a) between 1-2 floating then between 2-3 gradient motion (b) between 3-4 gradient motion then between 4-5 submerging then between 5-6 gradient motion then between 6-7 floating (c) sequential positions during the motion

The platform rotation provides desired EMA positioning for the motion. The rotation experiments were conducted with 15° platform rotation. During the experiments it was noticed that the gravity compensation value was not enough for the motion. In the rotated situation, the gravity compensation force is not at the same axis but angular with the gravitational force. To provide the former performance, the gravity compensation distance should be increased.

Using trial-and-error method, a proper gravity compensation distance was decided as 16 mm . Depending on the Figure 6.22, 15° angled motion was provided using new compensation distance, having an angled motion of 15.9° average, with 6.3% error.

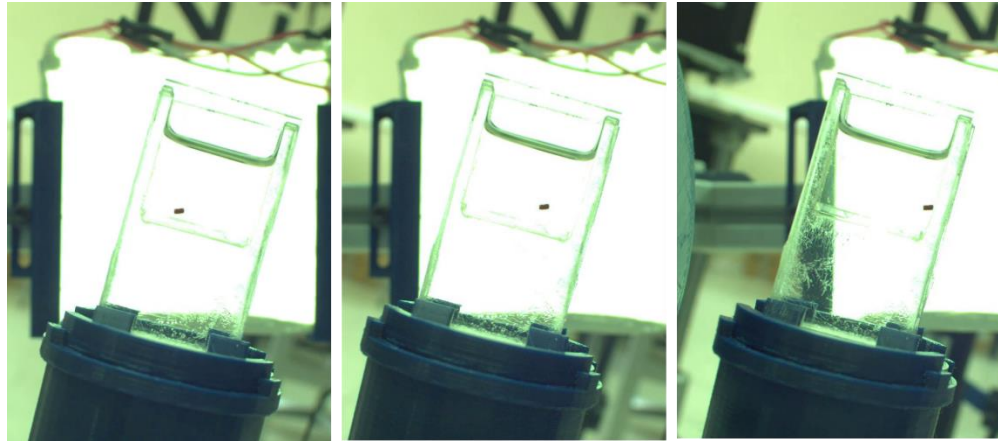


Figure 6.22 15° rotation motion with gravity compensation

6.5 Results and Discussion

In this chapter, the related motion graphics were presented with the related motion part. To sum up, the system can fulfil the needs for microrobot control.

Here, some findings are discussed, and opinions are asserted:

- Firstly, during the usage of the microrobot, it was seen that there is a possibility depending on the motion that the object tracker shifts its tracking position to the head or tail of the microrobot. This tracker shifting causes 0.5 mm of error. To compare the performance, the same motion video was tested, and the same result was obtained. It was concluded that in a proper motion the tracker always have possibility of making that much of error.
- Secondly, cameras were operated with 25 fps since higher fps values caused low gain images and tracking function was not working properly. Even if object tracker nodes run with 60 Hz, when too sudden moves including both microrobot and the manipulators the tracker can lose sight of the object. In general, not the microrobot but manipulator velocities were problem. Bluntly, fast responding motor parameters provide better motion but not for the tracker. It became an obligation to limit the motor parameters.
- The platform motors are controlled using one shared Arduino controller to provide synchronous motion. During these motions, since timer functions and interrupts are

actively used, the communication was temporarily cut off. Thus, to prevent the data loss, the command frequency was also limited. This situation becomes an obstacle for more complex motions since the platform may not be able to act on time.



CHAPTER 7

CONCLUSION AND FUTURE WORKS

7.1 Overview

The microrobot manipulators and locomotion methods were studied in the thesis scope. Ignoring the challenges in many scopes, it was realized that the systems were generally studied were mostly stationary and had a very narrow of workspace. With the systems providing mobility (programmable workspace), the actuator system can be combined, lowering the required number of all kinds of EMAs.

First, the microrobot structures and locomotion methods using external magnetic field were examined and microrobot analyses were handled, resulting with manufacturing of prior microrobot models. The proposed microrobot manipulation system depended on gradient-based motions and the studied applications consisted of navigation in phantom models. Thus, a simple microrobot structure was established.

Second, electromagnetic actuators were investigated, and an electromagnetic actuator model was designed, analysed, manufactured, and tested, considering the total system demands. The studies included unsuccessful works about ferrite core with custom materials and manufacturing, and a general optimization formulation for gradient based EMAs, however none of the stages were included in this thesis. Eventually, considering some performance parameters including weight, a custom EMA design was utilized.

Third, the manipulator systems were analysed, designed, manufactured, and tested. During the development phases, some other manipulators were analysed, studied and manufactured, and mentioned in the related chapter. The calibration results showed a result of repeatability with a total value of 0.1072 mm of standard deviation.

Fourth, a ROS based software was designed, developed, and integrated the hardware.

Then experimental setups were developed, and a few kinds of different experiments were performed. The development setups were depended on biomedical applications of cerebral aneurisms, which was found a lack of microrobot based applications. Also, this application is especially compatible with the proposed concept system. The motion results showed that specified goal-based motions can be established based on the xy and xz motions. However, challenges in vision systems and object tracking, using the manufactured microrobot the positioning error may rise to 0.5 mm, excluding the additional positioning errors caused by the optical refractions of the microrobot environment.

7.2 Future Works

The following expressions can be inspiring for the researchers who may aim to take this work to further steps:

- Considering the concept work is manufactured from this point towards, the mechanical system and the components can be top tier to prevent any mechanical calibration error.
- In the literature it is also seen that helical robots are considered for microrobot applications. To provide helical motion, rotating magnetic field generation is required. In this configuration it does not support rotating magnetic field generation. So, the concept can be improved using 3 EMAs instead of a pair.
- Different phantom types can be utilized, also using different imaging equipment.

REFERENCES

- Aghakhani, A., Pena-Francesch, A., Bozuyuk, U., Cetin, H., Wrede, P., & Sitti, M. (2022). High shear rate propulsion of acoustic microrobots in complex biological fluids. *Science Advances*, 8(10), 1–12. <https://doi.org/10.1126/sciadv.abm5126>
- Akçura, N., Gezgin, E., Çetin, L., & Tamer, Ö. (2019). Mikrorobot hareketinde kullanılacak Öklidyen platform robot manipülatörlü hibrit bir sistem tasarımı. *19. Ulusal Makina Teorisi Sempozyumu*, 371–378.
- Alasli, A., Akçura, N., & Çetin, L. (2018). Effect of the coil shape on magnetic field of an electromagnet for contactless power transmission to microrobots. *Mechanisms and Machine Science*, 52. https://doi.org/10.1007/978-3-319-60702-3_25
- Alasli, A., Çetin, L., Akçura, N., Kahveci, A., Can, F. C., & Tamer, Ö. (2019). Electromagnet design for untethered actuation system mounted on robotic manipulator. *Sensors and Actuators, A: Physical*, 285, 550–565. <https://doi.org/S0924424718312093>
- Alizade, R., & Bayram, Ç. (2004). Structural synthesis of parallel manipulators. *Mechanism and Machine Theory*, 39(8), 857–870. <https://doi.org/10.1016/j.mechmachtheory.2004.02.008>
- Alizade, R., Can, F. C., & Gezgin, E. (2008). Structural synthesis of Euclidean platform robot manipulators with variable general constraints. *Mechanism and Machine Theory*, 43(11), 1431–1449. <https://doi.org/10.1016/j.mechmachtheory.2007.11.006>
- Bakenecker, A. C., von Gladiss, A., Schwenke, H., Behrends, A., Friedrich, T., Lüdtke-Buzug, K., Neumann, A., Barkhausen, J., Wegner, F., & Buzug, T. M. (2021). Navigation of a magnetic micro-robot through a cerebral aneurysm phantom with magnetic particle imaging. *Scientific Reports*, 11(1), 1–12.

<https://doi.org/10.1038/s41598-021-93323-4>

- Bonev, I. A., Yu, A., & Zsombor-Murray, P. (2006). XY-Theta positioning table with parallel kinematics and unlimited theta rotation. *IEEE International Symposium on Industrial Electronics*, 4, 3113–3117. <https://doi.org/10.1109/ISIE.2006.296113>
- Carpi, F. (2010). Magnetic capsule endoscopy: the future is around the corner. *Expert Review of Medical Devices*, 7(2), 161–164. <https://doi.org/10.1586/erd.10.3>
- Çetin, L., Alasli, A., Akçura, N., Kahveci, A., Can, F. C., & Tamer, Ö. (2022). Dynamical electromagnetic actuation system for microscale manipulation. *Robotica*, 1–18. <https://doi.org/10.1017/S0263574722000418>
- Chevalerias, O., O’Mathuna, C., Twomey, K., & Mc Caffrey, C. (2008). Swallowable-capsule technology. *IEEE Pervasive Computing*, 7(1), 23–29.
- Clavel, R. (1988). A fast robot with parallel geometry. *Proc. Int. Symposium on Industrial Robots*, 91–100.
- Diller, E. (2011). Micro-scale mobile robotics. *Foundations and Trends in Robotics*, 2(3), 143–259. <https://doi.org/10.1561/23000000023>
- Dong, Y., Wang, L., Iacovacci, V., Wang, X., Zhang, L., & Nelson, B. J. (2022). Magnetic helical micro-/nanomachines: Recent progress and perspective. *Matter*, 5(1), 77–109. <https://doi.org/10.1016/j.matt.2021.10.010>
- Eliakim, R., Suissa, A., Yassin, K., Katz, D., & Fischer, D. (2004). Wireless capsule video endoscopy compared to barium follow-through and computerised tomography in patients with suspected Crohn’s disease - Final report. *Digestive and Liver Disease*, 36(8), 519–522. <https://doi.org/10.1016/j.dld.2004.03.011>
- Ergeneman, O., Abbott, J. J., Dogangil, G., & Nelson, B. J. (2008). Functionalizing

- intraocular microrobots with surface coatings. *Proceedings of the 2nd Biennial IEEE/RAS-EMBS International Conference on Biomedical Robotics and Biomechatronics, BioRob 2008*, 232–237. <https://doi.org/10.1109/BIOROB.2008.4762857>
- Floyd, S., Pawashe, C., & Sitti, M. (2008). An untethered magnetically actuated micro-robot capable of motion on arbitrary surfaces. *Proceedings - IEEE International Conference on Robotics and Automation*, 419–424. <https://doi.org/10.1109/ROBOT.2008.4543243>
- Freudenstein, F. (1959). Structural error analysis in plane kinematic synthesis. *Journal of Engineering for Industry*, 81(1), 15–21.
- Freudenstein, F., & Alizade, R. (1975). On the degree of freedom of mechanisms with variable general constraint. *Proceedings Fourth World Congress on the Theory of Machines and Mechanisms*, 51–56.
- Fusco, S., Huang, H. W., Peyer, K. E., Peters, C., Häberli, M., Ulbers, A., Spyrogianni, A., Pellicer, E., Sort, J., Pratsinis, S. E., Nelson, B. J., Sakar, M. S., & Pané, S. (2015). Shape-switching microrobots for medical applications: The influence of shape in drug delivery and locomotion. *ACS Applied Materials and Interfaces*, 7(12), 6803–6811. <https://doi.org/10.1021/acsami.5b00181>
- Fusco, S., Sakar, M. S., Kennedy, S., Peters, C., Pane, S., Mooney, D., & Nelson, B. J. (2014). Self-folding mobile microrobots for biomedical applications. *Proceedings - IEEE International Conference on Robotics and Automation*, 3777–3782. <https://doi.org/10.1109/ICRA.2014.6907406>
- Gogu, G. (2008). *Structural synthesis of parallel robots*. Springer.
- Gough, V. E. (1962). Universal tyre test machine. *Proc. 9th Int. Technical Congr. FISITA, London, 1962*.

- Huang, H.-W., Sakar, M. S., Petruska, A. J., Pané, S., & Nelson, B. J. (2016). Soft micromachines with programmable motility and morphology. *Nature Communications*, 7, 12263. <https://doi.org/10.1038/ncomms12263>
- Israelachvili, J. N. (2010). Intermolecular and surface forces. *Interactions*, 3152–3158. <https://doi.org/10.1002/elps.201000212>
- Khalil, I. S. M., Alfar, A., Tabak, A. F., Klingner, A., Stramigioli, S., & Sitti, M. (2017). Positioning of drug carriers using permanent magnet-based robotic system in three-dimensional space. *IEEE/ASME International Conference on Advanced Intelligent Mechatronics, AIM*, 1117–1122. <https://doi.org/10.1109/AIM.2017.8014168>
- Kim, D. H., Kim, B., & Kang, H. (2004). Development of a piezoelectric polymer-based sensorized microgripper for microassembly and micromanipulation. *Microsystem Technologies*, 10(4), 275–280. <https://doi.org/10.1007/s00542-003-0330-y>
- Kim, K., Nilsen, E., Huang, T., Kim, A., Ellis, M., Skidmore, G., & Lee, J. B. (2004). Metallic microgripper with SU-8 adaptor as end-effectors for heterogeneous micro/nano assembly applications. *Microsystem Technologies*, 10(10), 689–693. <https://doi.org/10.1007/s00542-004-0367-6>
- Kratochvil, B. E., Kummer, M. P., Erni, S., Borer, R., Frutiger, D. R., Schürle, S., & Nelson, B. J. (2014). MiniMag: A hemispherical electromagnetic system for 5-DOF wireless micromanipulation. *Springer Tracts in Advanced Robotics*, 79, 317–329. https://doi.org/10.1007/978-3-642-28572-1_22
- Kummer, M. P., Abbott, J. J., Kratochvil, B. E., Borer, R., Sengul, A., & Nelson, B. J. (2010). Octomag: An electromagnetic system for 5-DOF wireless micromanipulation. *IEEE Transactions on Robotics*, 26(6), 1006–1017.

<https://doi.org/10.1109/TRO.2010.2073030>

Mahoney, A. W., & Abbott, J. J. (2014). Generating rotating magnetic fields with a single permanent magnet for propulsion of untethered magnetic devices in a lumen. *IEEE Transactions on Robotics*, 30(2), 411–420. <https://doi.org/10.1109/TRO.2013.2289019>

Merlet, J.-P. (2006). *Parallel robots* (Vol. 128). Springer Science & Business Media.

Mhanna, R., Qiu, F., Zhang, L., Ding, Y., Sugihara, K., Zenobi-Wong, M., & Nelson, B. J. (2014). Artificial bacterial flagella for remote-controlled targeted single-cell drug delivery. *Small*, 10(10), 1953–1957. <https://doi.org/10.1002/sml.201303538>

Moll, S., & Waldron, B. (2014). Cerebral and sinus vein thrombosis. *Circulation*, 130(8), 68–70. <https://doi.org/10.1161/CIRCULATIONAHA.113.008018>

Nelson, B. J., Kaliakatsos, I. K., & Abbott, J. J. (2010). Microrobots for minimally invasive medicine. *Annual Review of Biomedical Engineering*, 12(1), 55–85. <https://doi.org/10.1146/annurev-bioeng-010510-103409>

Nogimori, W., Irida, K., Ando, M., & Naruse, Y. (1997). A laser-powered micro-gripper. *Proceedings IEEE The Tenth Annual International Workshop on Micro Electro Mechanical Systems. An Investigation of Micro Structures, Sensors, Actuators, Machines and Robots*, 267–271. <https://doi.org/10.1109/MEMSYS.1997.581822>

Popek, K. M., Hermans, T., & Abbott, J. J. (2017). First demonstration of simultaneous localization and propulsion of a magnetic capsule in a lumen using a single rotating magnet. *Proceedings - IEEE International Conference on Robotics and Automation*, 1154–1160. <https://doi.org/10.1109/ICRA.2017.7989138>

Ricotti, L., Trimmer, B., Feinberg, A. W., Raman, R., Parker, K. K., Bashir, R., Sitti,

- M., Martel, S., Dario, P., & Menciassi, A. (2017). Biohybrid actuators for robotics: A review of devices actuated by living cells. *Science Robotics*, 2(12), eaaq0495. <https://doi.org/10.1126/scirobotics.aaq0495>
- Schuerle, S., Erni, S., Flink, M., Kratochvil, B. E., & Nelson, B. J. (2013). Three-dimensional magnetic manipulation of micro- and nanostructures for applications in Life Sciences. *IEEE Transactions on Magnetics*, 49(1), 321–330. <https://doi.org/10.1109/TMAG.2012.2224693>
- Stewart, D. (1965). A platform with six degrees of freedom. *Proceedings of the Institution of Mechanical Engineers*, 180(1), 371–386.
- Tasoglu, S., Diller, E., Guven, S., Sitti, M., & Demirci, U. (2014). Untethered micro-robotic coding of three-dimensional material composition. *Nature Communications*, 5, 1–9. <https://doi.org/10.1038/ncomms4124>
- Tsai, M.-S., Shiau, T.-N., Tsai, Y.-J., & Chang, T.-H. (2003). Direct kinematic analysis of a 3-PRS parallel mechanism. *Mechanism and Machine Theory*, 38(1), 71–83.
- Wright, I. (2007). Cerebral aneurysm--treatment and perioperative nursing care. *AORN Journal*, 85(6), 1172–1176. <https://doi.org/10.1016/j.aorn.2007.05.014>
- Yesin, K. B., Vollmers, K., & Nelson, B. J. (2006). Modeling and control of untethered biomicrorobots in a fluidic environment using electromagnetic fields. *The International Journal of Robotics Research*, 25(5–6), 527–536. <https://doi.org/10.1177/0278364906065389>
- Yim, S., & Sitti, M. (2012). Design and rolling locomotion of a magnetically actuated soft capsule endoscope. *IEEE Transactions on Robotics*, 28(1), 183–194. <https://doi.org/10.1109/TRO.2011.2163861>